University of Sussex

School of Engineering and Informatics

Thermo-Fluid Mechanics Research Centre

Design of gas turbine axial compressors for fuel flexibility

Pascal Nucara

Submitted for the degree of Doctor of Philosophy

University of Sussex

November 2013

Declaration

I hereby declare that, to the best of my belief, the work presented in the thesis is original or has been developed in a joint effort and built upon existing knowledge as acknowledged in the text accordingly. The material has not been and will not be submitted in whole or in part to another University for the award of any other degree.

Signature:

Pascal Nucara

Abstract

Current gas turbine technology for power generation is generally optimised for natural gas. On the basis of current instabilities in natural gas price and supply, the use of alternative fuels, such as syngas, has recently gained high interest. Due to the different thermodynamic properties of syngas compared to natural gas the behaviour of existing gas turbine components may significantly change. From practical and economic points of view, it is generally considered that in order to meet the new fuel properties, the main effort should be put on the adaptation of conventional gas turbines in integrated gasification combined cycle (IGCC) plants rather than producing a new generation of gas turbine designs from scratch. In addition to the requirement of new combustion technologies, main critical issues are represented by the reduction of compressor surge margin and turbine blade overheating. Solutions might include thermodynamic cycle as well as turbine geometry modifications. The latter would be preferred in terms of power plant performance. The main aim of this thesis is to explore suitable solutions to be applied to gas turbine compressors in order to accommodate syngas combustion. Among others, the use of variable stator vanes (VSVs) and blade radial stacking line modifications are considered. These are investigated on reference geometries available in the public domain. A baseline compressor geometry representative of a conventional heavy-duty gas turbine fueled with natural gas is generated and modified according to the understating gained during this study. The re-designed machine is a result of the application of stator vanes re-staggering in the front stages and blade sweep in the rear stages in order to cope with compressor air supply control and critical flow separation regions respectively. The obtained results show that efficient and stable operation during power modulation can be achieved, while reducing the need of other modifications to the combined cycle plant. It was therefore concluded that the proposed option can be considered a viable option to satisfy some important technical and economic constraints imposed by the integration of an existing gas turbine within an IGCC plant.

Acknowledgements

Firstly, I am very grateful to my principal supervisor Professor Abdulnaser Sayma for his constant support during my time at University of Sussex. The frequent technical discussions with him significantly improved my understanding of turbomachinery flows and therefore the quality of my work. Naser also helped me to get through the last and tough stages of the project, including the writing of the thesis. I would also like to thank my second supervisor Dr Christopher Long for the very interesting technical and non-technical conversations we often shared over a cup of coffee. I am very grateful to Dr Vasudevan and Dr Xia Hao who, despite being very busy, always made time to answer my questions. I would also like to give thanks to Professor Herwart Honen for providing the IDAC compressor geometry and data and for the related discussions we had during the H2-IGCC meetings. The achievement of my thesis objectives was also possible thanks to the collaboration with Professor Giovanni Cerri and Dr Ambra Giovannelli, who provided the gas turbine mean-flow analysis on which part of my work is based. In particular, I am thankful to Ambra for her advice and suggestions that helped me gain further knowledge on axial compressor design.

Special thanks are due to my colleagues, Yanling, Eleni, Harri and Adrian for their friendship and support throughout my studies.

Last but not least, I would like to express my gratitude to my parents, Tina and Giuseppe, for their fundamental support.

Contents

List of Tables

List of Figures

Nomenclature

Roman Symbols

$\dot{m}$	mass flow rate
A	cross-sectional area
c	absolute flow velocity
c_a	axial flow velocity
C_l	lift coefficient
c_p	specific heat
c_w	whirl flow velocity
e	specific internal energy
f	fuel/air mass flow ratio
F_{out}	outlet flow function
h	static enthalpy
h_0	specific stagnation enthalpy
h_t	heat transfer coefficient
i	incidence angle
l	blade chord
M	molar mass, Mach number
m	NACA 4-digits θ_{max} as percentage of the chord
n	NACA 4-digits distance of θ_{max} from LE in tens of the chord
p	static pressure
p_0	stagnation pressure
q	distance of the point of maximum camber from the leading edge
r	blade radius
r_0	DCA leading and trailing edge radius

R_c	circular camber line radius
R_p	circular suction side radius
R_s	circular pressure side radius
s	blade pitch
t	thickness
T_0	stagnation temperature
u	tangential flow velocity
W	work
x, y, z	Cartesian system coordinates
y^+	non-dimensional wall distance
F_i	inviscid flux vector
G_i	viscous flux vector
S	source terms vector
u_i	velocity vector in the absolute reference frame
V	solution vector of conservative variable
w_i	velocity of the grid in the rotating frame
T	static temperature

Abbreviations

ASU	air supply unit
CCS	carbon capture and storage
CD	control diffusion
CFD	computational fluid dynamic
DCA	double circular arc
DF	diffusion factor
DF_m	modified diffusion factor
DoR	degree of reaction
ECPPS	energy conversion power plant simulator
FV	finite volume
HRSG	heat recovery steam generator
ID	integration degree
IDAC	three stage axial compressor built at RWTH Aachen University

IGCC	integrated gasification combined cycle
IGV	inlet guide vane
LASM	lowest allowable surge margin
LE	leading edge
LHV	low heating value
LP	loss parameter
NGCC	natural gas combined cycle
OGV	outlet guide vane
PR	pressure ratio
PVD	prescribed velocity distribution
RANS	Reynolds-averaged Navier Stokes
SM	surge margin
TE	trailing edge
TET	turbine exhaust temperature
TIT	turbine inlet temperature
VSVs	variable stator vanes

Greek Symbols

α	relative flow angle
$\alpha^{'}$	blade angle
β	absolute flow angle
δ	deviation angle
δ_{ij}	Kronecker delta function
ϵ	cooling effectiveness
η_b	combustion efficiency
η_{is}	isentropic efficiency
η_m	transmission efficiency
Γ	boundary of control volume
γ	specific heat ratio
κ	thermal conductivity
μ	dinamic viscosity
Ω	control volume

ω	blade rotational speed
ϕ	flow coefficient
ψ	stage loading
ρ	density
σ	blade solidity
σ_{ij}	stress tensor
θ	camber angle
ξ	total pressure loss coefficient
ζ	stagger angle

Subscripts

1	inlet to rotor blade-row
2	outlet from rotor blade-row/inlet to stator blade-row
3	outlet from stator blade-row
a	air
aux	auxiliary components
b	blade metal
C	compressor
c	coolant
CC	combined cycle
f	fuel
g	gas
GT	gas turbine
in	inlet to gas turbine component
out	outlet from gas turbine component
sp	stall point
T	turbine
wp	working point

Chapter 1

Introduction

1.1 Background

Fossil fuels have long been the world's major source of electricity production, with coal being the most used raw fuel due to its large reserves. The emission of carbon dioxide from existing coal based power plants is however considered one of the main factors responsible for climate change, commonly referred as "greenhouse effect". This led to a rapid introduction of alternative resources in order to meet the global electric power demand while reducing undesired emissions. Nowadays, a highly developed and commonly used technology for power generation industry is represented by combined cycle power plants fueled by natural gas. Natural gas combined cycle (NGCC) plants became popular mainly because of the substantial lower emissions of carbon dioxide and higher thermal efficiency compared to traditional coal-fired power plants. For instance, for an equivalent amount of energy released, natural gas combustion CO_2 production is estimated to be about 45% less than burning coal (Woods et al.). The simple combined cycle configuration is formed by a gas turbine (topping) plant thermodynamically on top of a steam turbine (bottoming) plant, as shown in Figure 1.1. The gas leaves the gas turbine at about 600°C with a pressure slightly higher than atmospheric. The exhaust enters a heat recovery steam generator (HRSG), which is a set of heat exchangers used to generate high pressure steam from the supplied heat. Steam is expanded through a steam turbine, sent to a condenser and finally returned to the HRSG as boiler feed water. The mechanical power generated by the gas turbine expander drives the compressor and an electric

generator which typically produces about 2/3 of the overall plant electric power.

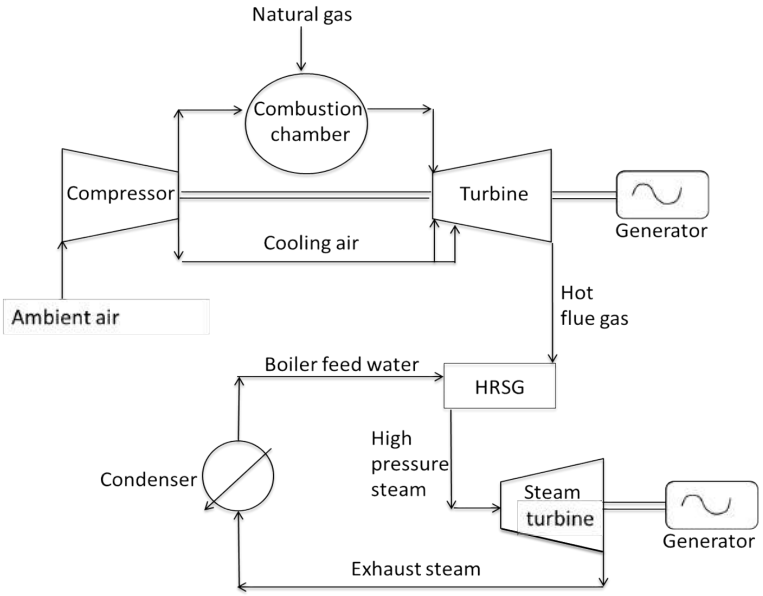

Figure 1.1: NGCC power plant sketch

The increase in emissions restrictions and current instabilities in natural gas price and supply, however, have renewed the interest in the development of advanced coal based power plants that could guarantee viable solutions for large scale carbon capture and storage (CCS), while providing high performance. In this scenario, the integrated gasification combined cycle (IGCC) fired with synthetic gaseous fuels (namely syngas fuels) seems to be one of the most promising long-term technologies [1, 2]. Syngas fuels are most often obtained from coal, biomass or solid waste gasification processes, resulting in a mixture of different gases mainly hydrogen, carbon monoxide, carbon dioxide and steam. A very attractive feature of syngases is the fact that, differently from the original raw fuels, they can be burned in the highly efficient gas turbine systems. The generic approach is to convert most of the coal-derived syngas to H_2 and CO_2 using the water gas shift reaction[1]. The CO_2 can be separated and removed, resulting in a fuel with high content of hydrogen. The hydrogen-rich syngas is finally burned in the gas turbine. The possibility of pre-capturing large amount of carbon dioxide represents another major advantage compared to conventional coal-fired power plants and constitutes the driving force for the expansion of IGCC systems [3]. Nevertheless there are still uncertainties

[1] $CO + H_20 \rightarrow H_2 + CO_2$

about the feasibility of CCS technologies within IGCC plants [4, 5].

Figure 1.2 shows a simplified sketch of an IGCC plant where two main parts can be distinguished: a power block and a gasifier block. Although the power block looks the same as the one illustrated in Figure 1.1, several key differences exist due to its integration with the gasifier. First of all, syngas fuels may have considerably lower low heating value (LHV) and energy density than natural gas. This means that, in order to reach the high power output within an existing gas turbine design, the mass/volumetric fuel flow rate will be much higher than the one with natural gas combustion.

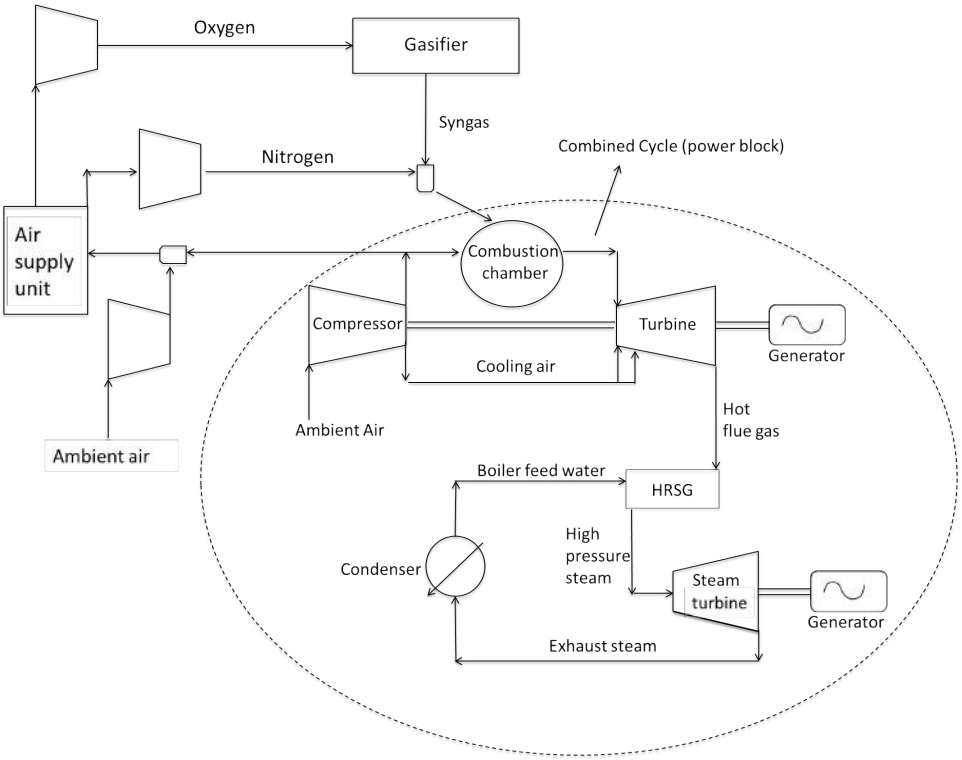

Figure 1.2: IGCC power plant sketch

Additionally, hydrogenated fuels are characterised by higher flame speed, higher adiabatic temperature and lower chemical kinetic times. Among the components of a conventional gas turbine, fuel injectors and combustors are those that need to be modified in order to cope with a larger volumetric fuel flow rate and higher risk of flash back and pre-ignition in the combustion chamber [6]. An important difference also exists in terms of adiabatic flame control and NO_x removal system. It is known that in NGCC plants premixed combustion systems are generally preferred. At

high load operation, fuel is supplied to both primary and secondary zones of the combustion chamber, but combustion only takes place in the second stage after fuel and air are pre-mixed in the first stage. For fuel/air ratios near stoichiometric values and high flame temperatures, steam can be added to the burner box in the dilution zone in order to minimise NO_x emissions. On the other hand, due to the higher flammability limit of hydrogen-rich syngas, at the current state-of-the-art IGCC plants premixed combustion systems are not practicable and the control of flame temperature and NO_x emissions is always achieved through large fuel dilution, mostly by nitrogen or steam [7].

Due to the greater amount of fuel (and fuel diluent) supply, development needs to be done for the turbine as well. The substantial variation of the turbine inlet mass flow rate would significantly affect the original matching with the compressor. Assuming the common turbine choking condition for heavy duty industrial power plants, the larger fuel flow rate would lead to a lower demand of air required from the compressor and, more in general, increase of compressor back-pressure. Thus, if no modification is applied to the existing geometry, this would cause a reduction of compressor stall margin that may not be tolerated because of the engine operation stability requirements [8].

Another important aspect related to the use of LHV fuels is the higher combustion exhaust gas specific heat. Depending on the syngas properties, even assuming a fixed turbine inlet temperature (TIT), this might first lead to turbine blade overheating [9]. A secondary effect is the larger turbine enthalpy drop, which might require a review of the structural integrity of the machine due to net power output increase [7].

From practical and economic points of view, it is generally considered that in order to meet the new fuel thermodynamic properties, the main effort should be put on the integration of conventional gas turbines in IGCC plants rather than producing a new generation of gas turbine designs from scratch. According to the Technology Readiness Level (TRL[2]), from an economical point of view it would be more convenient to introduce development programs departing from existing geometries [10]. In addition to the requirement of new combustion technologies, the

[2]TRL is a widely used index to rank the reliability of new technologies.

main critical issues are represented by the reduction of compressor surge margin and turbine blade overheating. Several options to cope with these restrictions are discussed in the literature. Solutions might include thermodynamic cycle as well as turbine geometry modifications. The former would require minor re-adaptations of the conventional plant components to the new mode of operation. However these would also imply an undesired reduction in performance. Therefore, effort is being made to propose more sophisticated strategies that involve the re-design of the turbomachinery system.

It should be pointed out that IGCC gas turbine operation are strongly dependent on other factors that define a certain integration scheme between the power block and the gasifier block auxiliary elements. A key component is the air supply unit (ASU) where oxygen is generated and provided to the gasifier. Although the gasification process can be oxygen-blown, air-blown or steam-blown type, the former is usually preferred since it allows for higher gasifier efficiency and reduction of gasifier downstream equipment [11]. Furthermore, an oxygen-blown unit would provide fuels with higher LHV values, thus reducing the required gas turbine modifications [12]. The way air is supplied to the ASU establishes a primary design parameter. Air can be delivered either by the gas turbine compressor or by an independent auxiliary compressor. The amount of air supplied to the ASU by the gas turbine determines the so-called integration degree (ID). This is defined as the ratio of the air supplied to the ASU from the gas turbine and total air provided to the ASU [13]. The level of integration can be also referred as air bleed ratio, i.e. the ratio between the amount of air provided to the ASU from the gas turbine and the compressor inlet mass flow. For a given fuel composition and thermodynamic cycle, the value of ID would establish the turbine inlet mass flow rate.

Another integration key factor is represented by the type of fuel diluent used. The choice of nitrogen or steam is quite straightforward. Steam is always available in a combined cycle and can be extracted from the steam turbine at any required rate and pressure. In the case of oxygen-blown gasification, however, a large quantity of nitrogen is generated within the ASU. The selection of the type of diluent supply strongly affects the functioning of the gas turbine components. Because of the different specific heat values of nitrogen and steam (c_{p,N_2} = 1.04 kJ/(kgK) and

c_{p,H_2O} = 1.864 kJ/(kgK)), the mass flow and thermodynamic properties of the gas mixture entering the turbine at a given temperature could have a large effect.

Beyond the influence of the adopted integration method on the gas turbine operation, however, it should be emphasised that optimum IGCC plant designs might not imply optimum combined cycle performance. This is essentially due to the considerable amount of auxiliary power consumption. Overall, the complexity and high costs related to integration systems represent the major drawbacks of IGCC technology. For instance, ASUs are complicated and expensive components that require high power consumption. The large amount of fuel dilution further increases both operational and installation costs. In this context, gas turbine designers are facing the challenge of providing solutions that would involve a minimum number of modifications in order to guarantee an existing plant to operate at high performance when syngas fuels are introduced.

1.2 Objectives

This work is part of the H2-IGCC project, co-funded by the European Union's 7th Framework Programme for Research and Development and coordinated by the European Turbine Network (ETN). The overall objective of the project is to provide and demonstrate technical solutions which will allow the use of state-of-the-art efficient gas turbines in the next generation of IGCC plants, suitable for burning undiluted hydrogen-rich syngas [1]. Furthermore, the power plant is required to allow for a quick switch to natural gas combustion in the event of gasifier failure or breakdown of feedstock supply chain. Twenty-three project partners are working four major research areas: combustion, materials, turbomachinery and system analysis. University of Sussex has been taking part in the turbomachinery sub-project, and the current study focuses on the issues related to the compressor/turbine mismatch and solutions to the potential compressor stability deterioration. The specific objectives of this thesis are:

1. To acquire a fundamental understanding of the impact of burning syngas on conventional industrial gas turbine operation and select appropriate compressor stability improvement techniques for the purposes of the current study.

2. To explore the selected techniques and propose suitable solutions to be applied to heavy-duty gas turbine compressors in order to cope with syngas combustion and fuel flexibility. Advantages and drawbacks of the investigated solutions compared to other possible gas turbine or cycle design modifications will be also discussed.

1.3 Literature review: Influence of syngas combustion and system integration options on combined cycle operation

The re-designed cycle for syngas combustion requires the analysis of the off-design condition that the reference gas turbine would encounter when the new fuel is used. According to the purposes of this study, the literature review is divided into two parts. In the first part, investigations on the effects of burning syngas and system integration methods on compressor surge margin reduction and turbine blade overheating are presented. Proposed solutions to cope with these problems are also discussed, including the consequent effects on system performance. Among the studies dedicated to gas turbine turbine modifications for IGCC power plants, however, few public domain references deal in detail with compressor re-design strategies. Nevertheless, standard techniques usually applied to enhance the stability of a given machine are clearly of interest for the current research. These are discussed in the second part of the literature review.

1.3.1 Compressor/turbine matching

The compressor/turbine design matching of an existing machine is strongly affected by the variation of the mass flow rate at the turbine inlet. Compressor maps are used to model the off-design operating characteristics (see Figure 1.3), while expander off-design operation are represented by the turbine choking condition reported in Equation 1.1, typical for heavy-duty industrial power plant [14]:

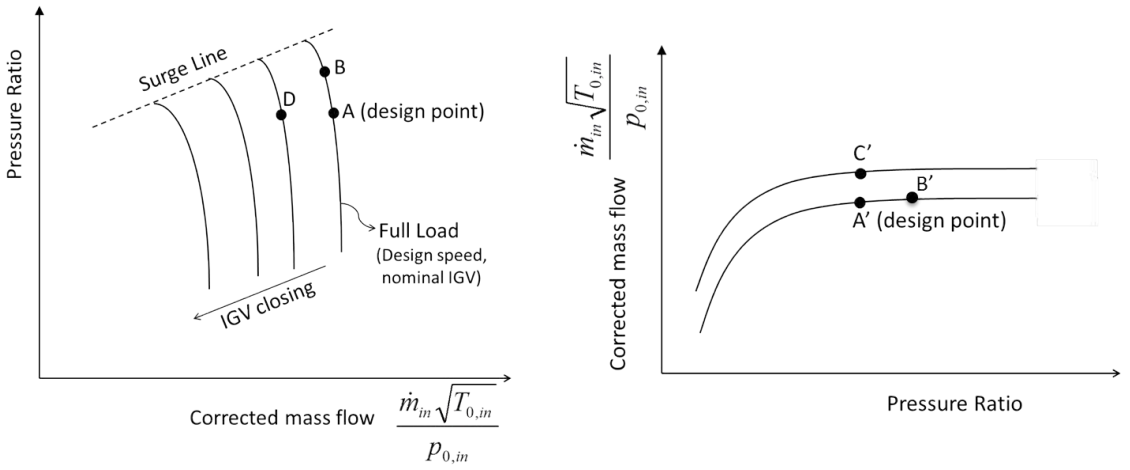

Figure 1.3: Typical compressor (left) and turbine (right) maps. Compressor part-load maps obtained by closing the IGV are also showed

$$\frac{\dot{m}_{in}\sqrt{\frac{TIT}{M}}}{KA_{in}p_{0,in}} = \text{constant} \tag{1.1}$$

where the subscript in refers to the turbine inlet section. M is the molar mass, $K = \sqrt{\frac{\gamma}{R}\frac{2}{\gamma+1}^{\frac{\gamma+1}{\gamma-1}}}$, γ is the specific heat ratio, $\dot{m}$ is the mass flow rate, A is the cross sectional area and p_0 is the stagnation pressure. In a recent analytical study [14], a large number of low LHV syngas fuels was selected in order to investigate a wide variety of gasification processes. The results showed that the different compositions and properties of the fuels led to relatively significant variations of molar mass compared to the case of natural gas. On the other hand, the difference in γ was considered less important so that Equation 1.1 could be reduced in first analysis to:

$$\frac{\dot{m}_{in}\sqrt{\frac{TIT}{M}}}{A_{in}p_{0,in}} = \text{constant} \tag{1.2}$$

From Equation 1.2, assuming the reference TIT and turbine geometry to be fixed, the higher fuel flow rate and dilution entails an increase of turbine inlet pressure. The operating point in Figure 1.3 moves from A and A$'$ to B and B$'$ pushing the compressor to work close to the surge line and, depending on the syngas fuel composition, over the safety margin. The influence of fuel composition on com-

pressor/turbine matching can be found in several public domain studies. However, the additional effects of system integration options are rarely discussed.

For instance, all these factors have been considered using analytical studies by Kim et al. [9]. Taking into consideration a standard raw syngas (LHV=10.5 MJ/kg) and full nitrogen supply, the authors first investigated the effect of the ID variation on a state-of-the-art frame F-class gas turbine[3]. For full integration (ID=100%), the results suggested a relatively small decrease of the reference surge margin due to the lower LHV of the syngas. An almost linear reduction of surge margin with lowering the ID was observed, resulting in a significant and critical compressor stability deterioration. The authors estimated that for high ID the problem could be alleviated by reducing the amount of nitrogen supplied to the combustor. At low integration (ID=25%), however, the original pressure ratio and surge margin could be only restored by venting all the available nitrogen outside the system. In a following work the authors added the effect of burning different types of syngas [13]. In particular, CO_2 capture process was applied to the raw syngas and both diluted and undiluted cases were considered, resulting in LHV values of 37 MJ/kg and 119.95 MJ/kg (pure hydrogen) respectively. For a fixed integration degree (ID=50%), as the syngas is cleaned before entering the combustor (increase of hydrogen content) the reduction in compressor stability is enhanced. However, even in case of pure hydrogen combustion the compressor stall margin resulted slightly lower than the original value. According to Equation 1.2, although the fuel mass flow rate reduces compared to natural gas combustion (LHV_{NG}=45 MJ/kg), the much lower molecular mass of hydrogen might lead to higher turbine inlet pressure.

The effect on compressor stability due to a large fuel diluition was highlighted by He et al. [15]. A CO-rich and H_2-rich undiluted syngas ($LHV_{CO-rich}$=12.4 MJ/kg and LHV_{H_2-rich}=42.2 MJ/kg) combustion was first considered using a E-class gas turbine as reference. Nitrogen dilution was then taken into account in order to reduce both fuel LHVs down to 7 MJ/kg. For each case, finally, the conditions of 0% and 5% air bleed ratio were assumed[4]. Both undiluted combustions resulted in a surge margin reduction, with the one relative to the CO-rich syngas being

[3]A brief discussion on the classification of gas turbines is provided in Appendix A

[4]Typically the air needed at the ASU is about 20-25% of the gas turbine inlet mass flow, thus an air bleed ratio of 5% corresponds to an integration degree of 25%.

more significant as expected. The surge margin would be enhanced by raising the air bleed ratio from 0% to 5% and for the H2-rich syngas case the original design pressure ratio could be almost restored. When considering fuel dilution, however, H2-rich syngas combustion led to a much larger departure from the reference design point compared to the case of burning CO-rich syngas. The impact of type of fuel dilution was investigated by Chiesa et al. [7] using a conventional F-class gas turbine as baseline geometry. First of all, in agreement with the mentioned studies, the authors estimated that burning undiluted hydrogen would result in a pressure ratio similar to the reference value, due to a balancing effect between fuel flow rate and molecular mass variations. In order to reduce the flame temperature to the reference design value, both steam and nitrogen dilution was applied. Because of the different specific heats, the required amount of nitrogen supply and thus the increase in pressure ratio resulted about double that in the case of steam dilution.

1.3.2 Turbine metal temperature

It is known that the combined cycle maximum temperature represents a key design parameter. Theoretically, for a simple gas turbine cycle, the higher the value the higher the engine performance. The maximum temperature is however constrained by metallurgical considerations related to turbine blade mechanical and thermal stresses as well as oxidation problems due to high gas temperatures. In any modern engine a large amount of cooling flow is therefore required. This is provided by the compressor and the overall bleed may reach 20-25% of the compressor inlet mass flow. Detailed cooling analysis can be very complex and it goes beyond the scope of this study. Nevertheless, for preliminary calculations, relatively simple thermodynamic models can be considered. In these models, the efficiency of the cooling system is described through the introduction of the cooling effectiveness (ϵ) [9, 15]:

$$\epsilon = \frac{T_g - T_b}{T_g - T_c} = f\left(\frac{\dot{m}_c\, c_{p,c}}{\dot{m}_g\, c_{p,g}}\right) \tag{1.3}$$

where the subscripts g, b and c refer to gas, blade metal and coolant respectively. The temperature difference ratio is regarded as the actual reduction in blade metal

temperature divided by the maximum possible reduction. Assuming perfect cooling the metal temperature is decreased to the cooling temperature, while in absence of cooling this is equal to the gas temperature, i.e. $0 \leq \epsilon \leq 1$. The term in brackets in Equation 1.3 defines the thermal capacity ratio between the coolant and hot gas and it is considered the main parameter that determines changes in cooling effectiveness at off-design condition. Another important parameter is represented by the average heat transfer coefficient on the outer side of the blade. Several correlations can be found in the literature and, as an example, Equation 1.4 reports the expression proposed by Louis [16]:

$$h_t = 0.285 \frac{(\rho c_s)^{0.63} c_p^{1/3} k^{2/3}}{l^{0.37} \mu^{0.3}} \tag{1.4}$$

where ρ and μ are the gas density and dynamic viscosity, c_s is the main stream velocity, k is the thermal conductivity and l is the blade chord length. Different aspects should be considered when discussing the effects of syngas combustion on an existing cooling system for a fixed TIT. First of all, both expressions 1.3 and 1.4 highlight the negative impact of an increase in combustion exhaust heat transfer properties on turbine blade metal temperature. Equation 1.3 also emphasises the decrease in cooling effectiveness due to the expected larger turbine inlet mass flow rate. Accordingly, as for the compressor surge margin issue, the problem deteriorates when the ID is reduced [15, 17]. The efficiency of a given cooling scheme may be also strongly affected by the cycle pressure ratio variations discussed in the previous section. Higher compressor pressure discharge means higher temperature of the extracted coolant. Furthermore, the higher pressure ratio increases both hot gas and coolant heat transfer coefficients, due to the higher fluid densities, and thus the heat flux across the blade walls. The net result is a substantial turbine blade overheating as the pressure ratio rises [7, 18]. A secondary effect is related to the greater turbine enthalpy drop due to the higher values of $c_{p,g}$ and pressure ratio, which leads to an increase of the turbine stream flow velocity c_s and therefore higher h_t.

Finally, fuel dilution plays an important role. Using nitrogen, for example, implies a lower $c_{p,g}$ compared to steam dilution possibly leading to considerable advant-

ages in terms of turbine blade overheating [7]. On the other hand, for a fixed TIT the use of nitrogen requires a larger amount of dilution that means higher turbine inlet mass flow and pressure ratio. The choice between steam and nitrogen would also depend on other factors such as syngas properties and ID, as well as system integration complexity and economical aspects. In any case, however, the reference TIT can not be maintained unless cycle or gas turbine geometry modifications are applied.

1.3.3 Possible gas turbine and cycle modifications

From the results of the studies mentioned in the previous section the following could be summarised:

- A high value of ID would reduce both surge margin reduction and turbine blade overheating problems.
- The possibility of burning undiluted hydrogen rich-syngas would imply minor surge margin variations even at relatively low ID.
- The use of nitrogen as fuel dilution might require minor cooling system modifications than in the case of steam supply. On the other hand it would lead to higher compressor surge margin deterioration.

Major problems related to high ID include high complexity and cost of the technology due to the strong integration between the gas turbine and gasifier block components [19]. In addition, in terms of design and integration of ASUs several studies agree that an optimum ID might be achieved when all the nitrogen available from the ASU is provided to the gas turbine and air that cannot be sent through the combustor, due to mass/volumetric flow restrictions, is sent to the ASU [11, 20]. For a typical raw syngas, this level of air extraction from the compressor would generally correspond to an ID=25-50%. Furthermore, although great effort is being devoted towards undiluted hydrogen-rich syngas combustion, current system cooling technologies still require significant fuel dilution. For such type of integration scheme, key boundary conditions in terms of compressor surge margin and turbine

metal temperature would not be satisfied. Modifications of the baseline cycle and/or gas turbine geometry are therefore required in order to guarantee a stable and safe operation. The different solutions proposed in the literature could be summarised as follows:

- Reduction of the TIT through a decrease of firing temperature, possibly sustained by an increase of the coolant mass flow rate.
- Blow-off the excess air from the compressor.
- Maintain the original compressor/turbine operating point by raising the swallow capacity of the expander.
- Allow for an increase in pressure ratio by adding one or more compressor stages.
- Maintain the original pressure ratio by reducing the compressor air supply.
- Combine some (or all) of previous solutions.

With the exception of the combustion chamber, which has to be anyway redesigned, some solutions would not require major modifications to the compressor, expander and cooling flow system. For instance, reducing the flame temperature would allow to satisfy both compressor surge margin and turbine blade overheating restrictions [7, 15]. The possibility of restoring the reference blade metal temperature is self-explanatory. Recalling Equation 1.2, an appropriate reduction of the TIT would also accommodate higher turbine inlet mass flow rate at the reference turbine inlet pressure. Nevertheless, such possibility is not attractive due to the substantial decrease of the combined cycle specific power output and efficiency. Better performance could be achieved via an extensive improvement of the cooling technology so that lower flame temperature decreases can be considered. For relatively low ID, however, the required coolant mass flow might be much larger than the reference one, suggesting the need of a complete re-design of the cooling system [17]. Another straightforward solution to cope with compressor surge margin reduction is represented by blowing-off the amount of air that cannot be sent through the gas turbine.

This clearly involves a waste of energy although part of the compressed air might be used within the IGCC plant. Consequently, more interesting strategies have been proposed in terms of expander and compressor reference geometry re-designs. For instance, the turbine flow capacity could be improved by increasing the nozzle inlet guide vane area, which would allow to keep the original pressure ratio and TIT at full fuel dilution without affecting the stability of the machine [8]. With reference to Figure 1.3, the compressor would still operate at the design point A, while the expander working point would move to point C$'$. The larger turbine mass flow rate together with the higher specific heat of hot gas (thus enthalpy drop) would result in much higher net power output[5] with respect to the reference engine, as indicated by Equations (1.5) and (1.6):

$$W_{GT} = (W_T \eta_m - W_C) \tag{1.5}$$

$$W_T = \dot{m}_g c_{p,g}(T_{T,out} - T_{T,in}) \ , \ W_C = \dot{m}_a c_{p,a}(T_{C,out} - T_{C,in}) \tag{1.6}$$

where η_m is the transmission efficiency that accounts for the (very small) losses due to bearing friction and windage, W_T and W_C are the expander and compressor powers, the subscripts g and a refer to gas and air respectively and the subscripts *in* and *out* refer to the inlet and outlet sections of the gas turbine element.

In addition to a larger turbine inlet area, further modifications are required in order to guarantee the machine structural integrity [7]. For instance an increase of number of turbine blades per blade-row might be necessary in order to cope with the higher torque acting at the root-sections. Changes (scale-up) to the steam turbine in order to accommodate the higher expander outlet mass flow should also be applied. The heat recovery steam generator and condenser need as well to be re-adapted to the new gas turbine exhaust condition and a generator with higher capacity is required [7, 8]. Finally, recalling Equation 1.3, it should be pointed out that, for a

[5]Compressor operating condition and work input can be considered unchanged

fixed TIT and combustion exhaust properties, the much larger amount of hot gas would have further negative influence on the existing cooling effectiveness.

The possibility of adding extra compressor rear stages would instead allow to avoid stability deterioration by increasing the maximum pressure ratio of the revised map. With reference to Figure 1.3, this would allow the compressor and turbine to operate at point B and B$'$ without affecting the original stall margin by shifting upward the surge line [18, 21]. Usually, the addition of one or two stages is required. In addition to the relatively high cost, this option might also involve a re-adjustment of stage matching at the new operating pressure ratio in order to maintain high compressor efficiency [18]. Similarly to the expander modification, a much higher net power output is achievable, since the higher pressure ratio (and thus turbine inlet pressure) allows for higher mass flow through the baseline expander nozzle area. It is known that changes in pressure ratio would affect the specific net power. It has been acknowledged that in conventional industrial gas turbines pressure ratios are close to the maximum specific power condition, mainly because this would permit maximum combined cycle efficiency [22]. As indicated in Figure 1.4, at high cycle temperatures and pressure ratios, the specific power curve is nearly flat so that the effect of changes in pressure rise would depend on the original design. Nevertheless, assuming an equivalent increase in inlet turbine mass flow rate, the net power output rise is expected to be lower compared to the one obtained by means of an enlargement of the first turbine inlet guide vane area. For a fixed TIT, this is due to the higher pressure ratio that implies a higher work input required by the compressor and lower turbine outlet temperature. Overall, however, the discussed structural modifications and re-adaptations of the bottoming cycle to cope with higher shaft power and turbine outlet mass flow rate should be taken into account. It is important here to recall the negative effect of an increase in pressure ratio on the cooling scheme effectiveness. In particular, assuming other design parameters to be fixed (TIT, turbine inlet mass flow rate, syngas properties) the addition of compressor rear stages would lead to a more serious turbine blade overheating with respect to the expander scale-up option. In case a relatively high pressure ratio increase is required, it might not be possible to operate at the reference TIT which has to be decreased [7].

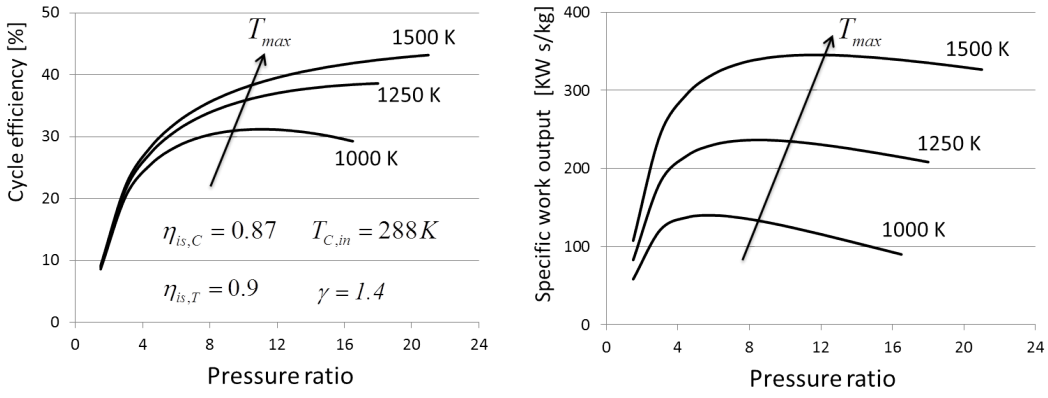

Figure 1.4: Efficiency and specific power output of a simple cycle gas turbine.

The other compressor modification solution would be to reduce the air supply by closing the inlet guide vane (IGV) in order to cope with higher fuel and fuel diluent flow rates while keeping the reference turbine inlet volumetric flow rate and TIT unaltered. With reference to Figure 1.3, it can be assumed that the compressor working point moves to position D while the nominal expander operation is maintained (point A$'$). In addition to changes in turbine enthalpy drop, related to the enhanced hot gas specific heat, compared to the baseline machine the net power output is further increased due to a reduction in compressor work input. Nevertheless, with respect to the two gas turbine geometry modifications previously mentioned, a lower net power output would be achieved since the inlet turbine mass flow rate may not significantly change. A major advantage of such option resides in the fact that, keeping the baseline cycle TIT, turbine inlet mass flow rate and pressure ratio, requires minor cooling technology adjustments. However, as indicated in Figure 1.3, although the stall margin is improved compared to the operation at point B, the original compressor stability would slightly reduce and further modifications to the compressor might be needed [7].

Taking into account Equation 1.7, the effect of integration factors on system performance should be briefly discussed[6]. Assuming full nitrogen dilution supply and fixed TIT and type of fuel, lowering the ID would tend to further increase the mass flow rate through the turbine. This means that grater cycle/geometry modifications are needed. Despite higher gas turbine power is theoretically achievable, this also re-

[6]Other minor power consumptions exist due to the presence of several pump powers and the syngas expander.

quires a higher auxiliary air compressor consumption. Furthermore, considering the large power required from the nitrogen compressor, which has to bring the nitrogen from atmospheric pressure to higher values than combustion air, the system power output might not vary significantly [13]. The overall auxiliary power consumption could be decreased taking into account steam dilution. However, this would clearly involve a reduction in combined cycle power.

$$W_{IGCC} = W_{CC} - W_{aux} = W_{CC} - [W_{air\ comp} + W_{0_2\ comp} + W_{N_2\ comp}] \tag{1.7}$$

Despite very different strategies can be followed during a design process, it should be recalled the common task of minimising the number of gas turbine modifications and cost, which represents a major disadvantage of IGCC power plant technology. A main incentive for the current research is therefore found in the option of compressor air supply reduction. In particular, the possibility of reducing the need of major cooling system and bottoming cycle modifications would represent an important advantage. The main drawback is the reduction in surge margin, as observed in Figure 1.3, considering that the reference pressure ratio has to be guaranteed. However, similarly to standard combined cycle part-load operation, another way of extending the surge boundary could be possible through the application of variable stator vanes (VSVs) rather than closing only the IGV or adding compressor rear-stages. Clearly VSVs schedules as well as other techniques generally used to enhance axial compressor surge margin and range of operation are of interest for the purposes of this work. Some of the studies related to these compressor stability improvement methods are reported in the next section.

1.4 Literature review: axial compressor stability enhancement

It is well known that a main technique to improve compressor performance and stability at off-design condition is the use of VSVs. The basic purpose is to redirect

the air towards the respective downstream rotors in oder to keep the incidence angle within an acceptable range away from the stalling incidence. While at design condition optimum stator vane schedules are determined following standard rules and analytical tools, at off-design operation new guide vane settings are usually obtained through rig tests or numerical optimisation procedures. In both cases the general procedure is to allow each guide variable vane to move independently in order to find the required schedule for the specific geometry under analysis. It would be expected that for a given off-design condition, the optimum VSVs stagger ratio configuration (the stagger angle variation ratios between the IGV and other variable stators) would be generally different from those relative to other load operation. However, mechanical simplicity prevails over the aerodynamic requirements and compressors are generally fitted with a single mechanical actuator [23]. Optimum VSVs settings should be therefore regarded as trade-off between different off-design condition at which the machine is required to operate.

In combined cycles, VSVs are widely used to control the air mass flow rate at part-load operation. Analysis and prediction of combined cycle off-design performance is of high relevance considering that power plants operate at part-load condition for a considerable part of their lifetime. The two main power control strategies adopted by manufacturers are known as *fuel only control* and *air flow modulation* using the VSVs. The former method is the simplest and does not require compressor air flow rate modulation. However, the latter is generally preferred, which is explained as follows. For a given combined cycle specific power, the fraction relative to the gas turbine decreases if air flow modulation is applied since the fuel is not effectively used and a relatively large amount of provided energy flows out from the expander. This also results in lower gas turbine efficiency. On the other hand, the consequent higher turbine exhaust temperature (TET) leads to higher steam turbine efficiency. According to available public studies on combined cycle, when air flow modulation is used the net effect is an increase in the power plant efficiency [24, 25]. Generally, the main purpose is to maintain the design TET constant for a wide load range, which can be extended by increasing the number of VSVs in order to guarantee safe operation in terms of compressor stability [26]. Some manufactures adopt a slight variation, where the principle is to keep the design TIT constant. This leads to a

TET higher than the design value due to the lower pressure ratio and thus further improvement in terms of combined cycle efficiency. However, constant TIT control solution is strongly constrained by the maximum allowable TIT (and TET) considering hot section life cycle. As a consequence, for a given machine, the part-load range (typically obtained with IGV only control) is narrower with respect to the one achievable using constant TET control strategy. The choice between the two methods clearly depends on the load characteristics at which the power plant would mainly operate although, in any case, further load reductions can be obtained by only varying the fuel flow rate [22].

Based on the concept of VSVs application, in this work the possibility of re-staggering the front guide vanes of a heavy-duty gas turbine compressor to meet syngas combustion operation will be taken into account. In addition, other major strategies to achieve further compressor stability enhancement should be considered. These can be regrouped in three main classes:

- Casing treatment
- Air injection or end-wall recirculation
- Blade radial stacking line modifications

The first two methods are typically applied wherever rotor tip regions are critical. It is known that at blade tip the pressure difference between the pressure and suction sides generates a tip-leakage flow that moves into the main flow. The interaction between the two flows gives rise to a vortex which originates in the proximity of the leading edge and propagates into the blade passage, along the pressure surface and towards the leading edge of the adjacent blade, which is a low relative Mach number zone. Consequently the blade passage might be partially or fully blocked. Moreover, the interaction of such vortex with the casing boundary layer and (in case of transonic blade profiles) passage shocks has detrimental effects on the overall performance. As the compressor back pressure is increased from nominal condition, this flow structure becomes stronger and more unsteady eventually leading to flow instabilities and compressor stall. Thus, the general objective is to reduce such tip clearance vortex effects without affecting the performance. This presents a high

challenge, considering the complexity of the phenomena related to tip clearance vortex generation and propagation. A useful information is however provided in the work performed by Lakshminarayana et al. [27] who highlighted that tip leakage flow is produced near the quarter of tip chord and reaches its maximum intensity around the mid-chord.

In casing treatments, surge margin improvement is obtained using casing cavities along the blade tip axial chord. The two major techniques are know as groove-type and slot-type treatments and some examples are illustrated in Figure 1.5. The basic concept of groove-type methods is to reduce the pressure gradient over the blade tip and thus tip-leakage velocity and strength. This additionally leads to a change of tip leakage vortex trajectory which is driven by the main flow, resulting in lower blade passage flow blockage [28, 29]. A main goal is however to optimise the volume of the device while maintaining the positive effect on flow stability in order to reduce the cost. For instance, a numerical and experimental investigations showed that the application of two grooves near the leading edge of the first rotor of a two stage axial compressor had similar effect on stability margin than applying five groove evenly spaced along the blade tip chord [30]. The mechanism of slot-type treatment is characterised by flow recirculation through the slots, where flow is "bled" from the rear part of the passage and re-injected further upstream of the leading edge. Such mass injection may have a strong impact on the tip clearance vortex, which is reduced in strenght and shifted towards the trailing edge so that further reduction of mass flow rate and higher maximum pressure ratio are achievable [31, 32].

Despite the considerable stability improvement, however, efficiency penalties were generally observed. In particular, the bleeding mechanism of slot-type methods as well as the flow circulating in the groove cavities are responsible of stronger shear layers that might induce substantial additional viscous losses. Furthermore, losses arise from the mixing between the re-injected flow and main flow. Nevertheless, reducing the tip-leakage vortex effects would also allow for a decrease of the related entropy generation. Although there isn't still a deep understating of the mechanism, this might explain why in few studies slight efficiency enhancements have been predicted [33].

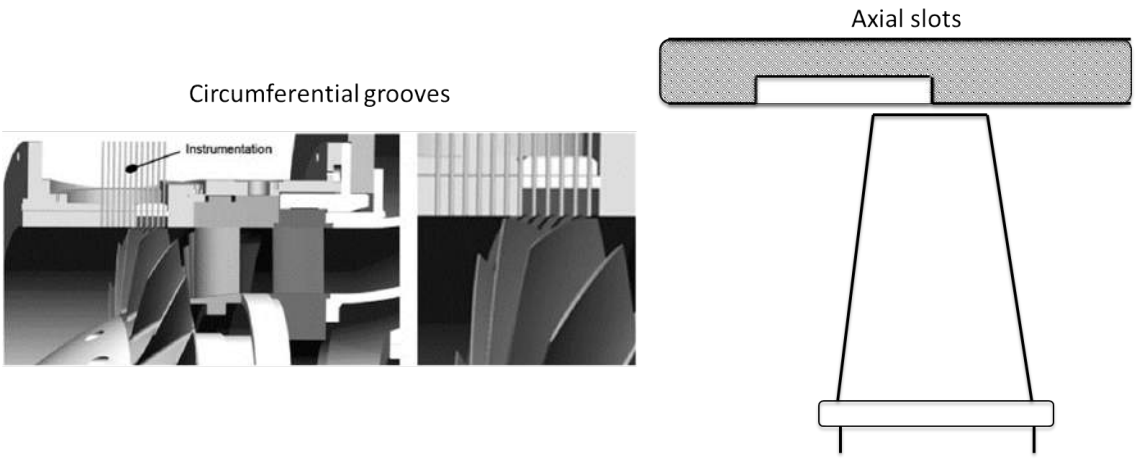

Figure 1.5: Circumferential grooves and axial slots casing treatments

Similarly to slot-type casing treatments, the generic concept of air injection is to increase the circumferential mass averaged axial velocity at rotor tip. The purpose is to reduce the very high local incidence angle (unloading of the rotor tip), typical of near-stall flow condition, allowing for a further compressor mass flow rate reduction. Air injection can be provided either by an external source or by bleeding some flow from downstream stages (end-wall recirculation). The latter method is preferred due its higher practicability since high pressure fluid is directly provided by the machine. In their analysis on a single axial compressor stage, Suder et al. [34] found that increasing the speed of the injected air has higher positive impact than increasing the injected mass flow. Thus, better surge margin enhancement could be achieved by maintaining choked condition in the injector flow path rather than increasing the number of injectors. These results have been confirmed in subsequent studies [35]. An important aspect of this technique is that it causes radial and hence axial flow re-matching, possibly leading to a variation of stage pressure ratios, compressor inlet mass flow and thus reference working point. In particular, Hiller et al. [35] pointed out a reduction of the total temperature at blade tip due to flow incidence reduction, while the opposite was found in the core region. On the other hand an increase of the radial total pressure ratio profile was observed. However, as argued by the authors, the relevance of such effects on working point condition would strongly depend on the reference design. Strazisar et al. [36] added that a multi-stage compressor surge margin improvement might result from an enhancement of the stage matching at near-stall condition rather than a decrease in stalling

mass flow of an individual blade-row. Since compressor re-matching depends on the original design, a specific recirculation technique (locations of bleed and re-injection) should be carefully designed considering the baseline throttling characteristic of each stage. A main disadvantage of such technique is that the supplied flow is compressed but does not contribute to turbine power. In addition, the design of high velocity jet injectors represents a significant challenge in terms of pressure losses. It is worth noting that while casing treatments are permanent geometric modifications, resulting in a continuous interaction with the flow, air injection systems can be disabled when not needed.

The two mentioned techniques are being largely investigated in aircraft engine compressors where rotor tip regions becomes usually critical, especially at part-speed operation. In industrial power plant, however, compressors might be trigged to stall by large flow separations along rotor and stator suction side at both hub and tip regions. Therefore, blade radial stacking line modifications, such as sweep and lean, probably present a more attractive solution for the current study. In this work the effects of sweep and lean on performance are investigated on a transonic rotor blade (Chapter 3) and subsonic stage (Chapter 4) where further literature reviews are accordingly provided.

1.5 Contributions

A common theme of the public studies on IGCC power plants is the need of turbomachinery re-design if high gas turbine performance is required. Other solutions may involve a significant derating of the engine. The most discussed combined cycle update is the re-size of the turbine inlet section, while compressor geometry variations mainly regard the possibility of adding additional stages. Typically these solutions require several adaptations to the bottoming cycle and changes to the cooling system. Furthermore, investigations are usually conducted via analytical methods since the overall power plant system is considered.

Based on the combined cycle system analysis provided by other H2-IGCC project partners, the study presented in this thesis aims to propose the air compressor delivery reduction as an efficient and cost competitive solution for heavy-duty gas

turbines. The viability of such solution is further assessed by the application of computational fluid dynamic (CFD), which reduces the limits of mean line analyses due to three-dimensional effects. Furthermore the study includes part-load operation, rarely discussed in the literature within the IGCC context. The obtained results suggest that stable and safe power control can be achieved keeping the original expander unchanged, gas turbine and combined cycle performance similar to the baseline design and allowing for minor modifications to other important plant components.

1.6 Thesis outline

This thesis is divided into 7 chapters, including the introduction. A description of the in-house numerical model used is provided in Chapter 2, where a validation case study is also presented. General advantages and limitations of using CFD modelling as a design tool are also discussed.

Chapter 3 focuses on transonic rotor blade modifications, such as stagger, sweep and lean, which might be useful for the re-design of a compressor geometry required when syngas fuels are used. In particular the discussion focuses on the possibility of maintaining the stability range and performance of an existing transonic stage unchanged when operating at lower mass flow range.

In Chapter 4 the analysis is extended to a multi-stage axial compressor. The purpose is to investigate the possibility of re-staggering a 3.5 stages machine to provide an efficient air supply reduction. Only guide vanes stagger variations are considered in order to emphasise that the installation of VSVs might allow for a relatively simple and efficient adaptation of the compressor to different combustion processes. The use of sweep is also explored as further tool in order to reach the specific target. In particular the modification is applied in a highly loaded subsonic stage and the improvements obtained in terms of performance and fuel-flexibility are discussed.

Chapter 5 is dedicated to the generation of the H2-IGCC gas turbine compressor baseline geometry for natural gas combustion. A standard procedure is used, which starts with the determination of the basic machine configuration by means of a

through-flow model in order to provide the specified cycle parameters and mean line turbomachinery design. Three-dimensional compressor blade design is performed, which is assisted by CFD analysis in order to asses the suitability of the machine for the specified duty.

Chapter 6 deals with the re-design of the H2-IGCC compressor reference geometry in order to cope with a specific H2-rich syngas combustion. The new configuration is a result of the understating gained during this study. In particular, the proposed "new" machine is obtained through the application of stator vanes re-staggering in the front stages and blade sweep in the rear stages in order to cope with air supply control and critical flow separation regions respectively. The results show an efficient and stable configuration at nominal and part-load operation, thus representing an interesting solution for the purpose of the H2-IGCC project.

Conclusions from the current study and suggestions based on the acquired knowledge are finally presented in Chapter 7.

The basic features of gas turbines units and their classification in different level classes are described in Appendix A.

1.7 Publications

Selected parts of this research have been published in the following papers:

- P. Nucara and A.I. Sayma *"Effects of using hydrogen-rich syngas in industrial gas turbines while maintaining fuel flexibility on compressor design"* ASME paper GT2011-45589

- P. Nucara and A.I. Sayma *"Effects of using hydrogen-rich syngas in industrial gas turbines while maintaining fuel flexibility on a multistage axial compressor design"* ASME paper GT2012-69780

The following paper has been submitted to the ASME Journal of Engineering for Gas Turbine and Power in October 2013:

- P. Nucara, A.I. Sayma and A. Giovannelli *"Re-design of a Heavy-Duty Gas Turbine Axial Compressor for H2-rich Syngas Operation"*

Chapter 2

In-house CFD model Validation

2.1 Introduction

In this chapter the in-house numerical model used in the current work to perform CFD simulations and a particular validation study are presented. The computational approach is first introduced. Test case (NASA Rotor 37) design features and parameters are reported. This test case has been widely used by several authors because of the availability of experimental data in the public domain, so that the results obtained in this work could be also compared with previous numerical studies. The validation is preceded by a grid-independence study with the intent of acquiring an insight on the effect of varying the mesh resolution on solution accuracy. In addition, advantages and limitations of using CFD methods as turbomachinery design and analysis tool are discussed.

2.2 In-house computational model

2.2.1 Flow model

The in-house CFD code (SURF) used in the present work is based on the methodology developed by Sayma et al. [37, 38, 39]. The code is a finite volume solver for simulation of steady and unsteady viscous compressible flows for turbomachinery applications. Reynolds-averaged Navier Stokes (RANS) equations are computed in their conservation form in a Cartesian coordinate system that rotates with the blade. For a given control volume Ω and its control surface Γ the governing equations can

be written as:

$$\frac{d}{dt}\int_{\Omega} V\,d\Omega + \oint_{\Gamma} (F_i - G_i)\cdot n\,d\Gamma = \int_{\Omega} S\,d\Omega \tag{2.1}$$

where V is the vector of the conservative variables, F and G are the inviscid and viscous flux vectors respectively and S contains the source terms of Equation (2.1) due to the rotation of the reference system. The explicit form of these terms is:

$$V = \begin{pmatrix} \rho \\ \rho u_i \\ \rho e \end{pmatrix} \tag{2.2}$$

$$F = \begin{pmatrix} \rho(u_j - w_j) \\ \rho u_i(u_j - w_j) + p\delta_{ij} \\ \rho e(u_j - w_j) + p u_j \end{pmatrix} \tag{2.3}$$

$$G = \begin{pmatrix} 0 \\ \sigma_{ij} \\ u_k\sigma_{ik} + \kappa\frac{\partial T}{\partial x_i} \end{pmatrix} \tag{2.4}$$

where ρ is the density, p is the static pressure, T is the temperature, e is the specific internal energy, u_i is the absolute flow velocity vector, w_j is the grid velocity in the reference frame and κ is the thermal conductivity. The stress tensor σ_{ij} expression is:

$$\sigma_{ij} = \mu\left(\frac{\partial u_i}{\partial x_j} + \frac{\partial u_j}{\partial x_i}\right) - \frac{2}{3}\delta_{ij}\mu\frac{\partial u_k}{\partial x_k} \tag{2.5}$$

where μ is the sum of the molecular and turbulent viscosity. The term S of Equation (2.1) is given by:

$$S = \begin{pmatrix} 0 \\ 0 \\ \rho\omega u_2 \\ \rho\omega u_3 \\ 0 \end{pmatrix} \tag{2.6}$$

where ω is the rotational speed of the coordinate system around the x_1 coordinate. The equation set is complemented with the perfect gas relation:

$$p = (\gamma - 1)\rho\left(e - \frac{c^2}{2}\right) \tag{2.7}$$

where γ is the the fluid specify heat ratio.

Finally, the Spalart-Allmaras model is used to close the RANS set of equations, in which a differential transport equation for the eddy viscosity is solved [40].

2.2.2 Numerical methodology

An edge based data structure is used to represent the computational unstructured grid which, in principle, can contain cells with any number of boundary faces. A given internal node I is connected to the cell vertices $J_1 \ldots J_{n_s}$, where the solution vector is stored, so that Equation (2.1) can be discretised as:

$$\frac{d}{dt}(\Omega_I V_I) + \sum_{s=1}^{n_s} \frac{1}{2}|\eta_{IJ_s}|(F_{IJ_s} - G_{IJ_s}) + B_i = \Omega_I S_I \tag{2.8}$$

where Ω_I is the control volume associated with to node I, V_I the solution vector at node I, F_{IJ_s} and G_{IJ_s} the inviscid and viscous fluxes along IJ_s sides, B_i the boundary integral and η_{IJ_s} the side weight obtained as the sum of the each control volume area adjacent to the IJ_s side. The numerical discretisation is shown in

Figure 2.1. For clarity this is illustrated on a two-dimensional mesh, although the formulation is applicable to three-dimensional cells. For example, in this case the side weight η_{IJ_1} is obtained by the summation of the two dual median lengths around the side times their normals: $\eta_{IJ_1} = -\eta_{IJ_1} = \overrightarrow{AB} + \overrightarrow{BC}$. The inviscid fluxes F_{IJ_s} are expressed using a central difference formulation with artificial dissipation based on an upwind scheme. Such scheme allow for a numerical dumping of oscillations in proximity of discontinuities where the scheme reverse to first order using a pressure-based sensor. The viscous fluxes are expressed using the edge weights η_{IJ_s} and evaluating the required gradients of the primitive variables at the mesh nodes.

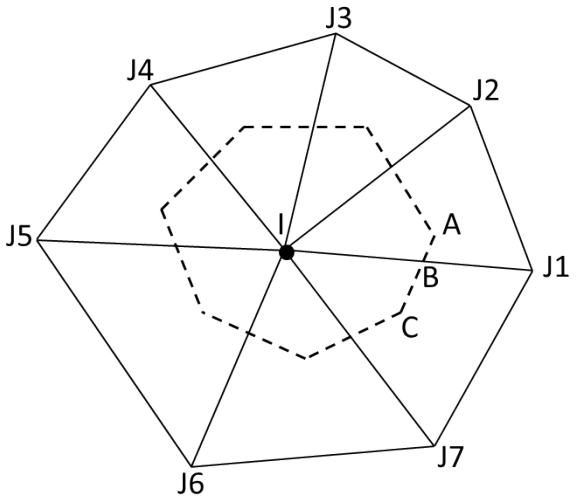

Figure 2.1: Typical two-dimensional mixed-cell mesh

Typical boundary conditions for turbomachinery are applied. In particular, total pressure and total temperature profiles and two flow angles are used at the inflow boundary, whereas static pressure is used at the outflow. Standard steady-state simulations for a single passage are performed by applying periodic conditions in blade-to-blade direction and mixing planes at blade-row interfaces in the case of multi-blade-row axial compressor simulations. Finally, near solid walls the viscous computations are performed in conjunction with the wall function, with a slip velocity boundary condition and the velocity normal to the wall set to zero in a weak sense.

2.3 Test case

NASA Rotor 37 is a low aspect ratio transonic rotor designed at the National Aeronautics and Space Administration Lewis Research Center (now NASA Glenn Research Center) in the late 1970's [41, 42]. The design of Rotor 37 was part of a research program on axial-flow compressor for aircraft engines. In particular, Rotor 37 was designed to be representative of the rotor of an inlet stage for an eight stage high-pressure core compressor. The rotor blade-row was originally built and studied experimentally by Reid and Moore and was retested in the 1990's by Suder et al. [43]. The design parameters are listed in Table 2.1. During the measurements the rotor was isolated with a circumferentially uniform inlet flow so that the flow through it could be considered steady. Despite that, due to a strong shock-boundary layer interaction which extends along most of the blade span, the rotor presents a challenge for 3D viscous flow solvers. Figure 2.2 shows Rotor 37 meridional view and two typical measurement locations, where comparisons between numerical results and experimental data are carried out. Due to the large amount of available data, the flow field at design speed is examined in details at two different operating condition, corresponding to 98% (near-peak efficiency) and 93% (near-stall) of the choking mass flow rate.

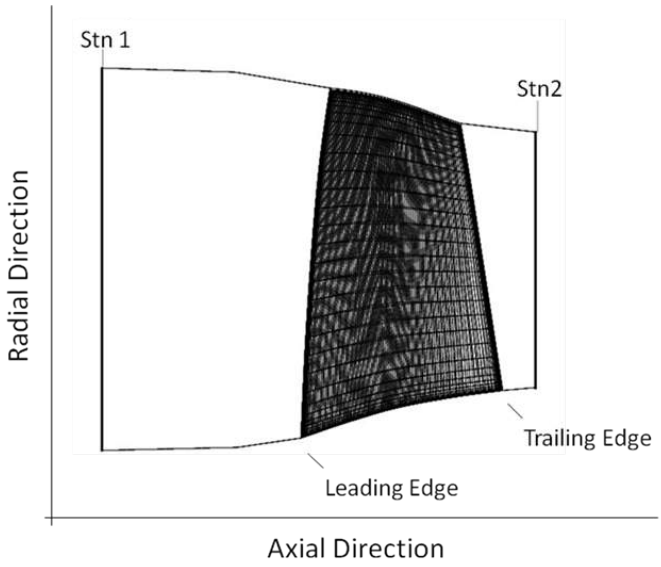

Figure 2.2: Rotor 37 cross section and measurement stations

Table 2.1: NASA Rotor 37 design parameters

Number of rotor blades	36
Tip solidity	1.288
Inlet hub-to-tip diameter ratio	0.7
Blade aspect ratio	1.19
Tip relative inlet Mach number	1.48
Hub relative inlet Mach number	1.13
Tip clearance (mm)	0.356
Mass flow rate (kg/s)	20.19
Choking mass flow rate (kg/s)	20.93
Blade speed (rad/s)	1800
Tip speed (m/s)	454.136
Total pressure ratio	2.106
Polytropic efficiency (%)	0.889

2.4 Grid independence study

The in-house grid tool (SURFM) allows for the generation of semi-structured meshes using a combination of structured and unstructured meshes, the former in the radial direction and the latter in the axial and tangential directions. A structured O-grid is used to resolve the boundary layer around the blade. Tip gap grids are generated using an unstructured mesh in the region within the blade tip and projecting a number of mesh layers in the tip gap (see Figure 2.3).

In order to investigate the grid influence on the numerical solution, four different meshes have been generated. Starting from a relatively coarse grid the number of control volumes has been gradually increased for each type of grid. Due to the type of turbulence closure applied and use of the wall function, however, the mesh should not be arbitrarily refined close to solid boundaries. In particular, the radial distribution at the end walls is set in order to obtain a desirable value of the

non-dimensional wall distance ($y^+ \approx 30$) and excessive stretching in the direction normal to the wall should be avoided [44]. Table 2.2 shows the number of points per blade passage and distribution used for each grid. For each case, the mapping of characteristic curves starts from the choking condition. Once the steady-state simulation has converged the back pressure is increased in order to march towards the stall point. The variation of the back pressure has been obtained by adding an outlet guide vane (OGV) and variable area nozzle downstream the rotor. Since only the rotor geometry is available in the public domain, the stator design used in this work for CFD calculations is a matching aerodynamic blade design produced by University of Sussex. The objective of using such an OGV is to remove the swirl from the flow as it enters the nozzle.

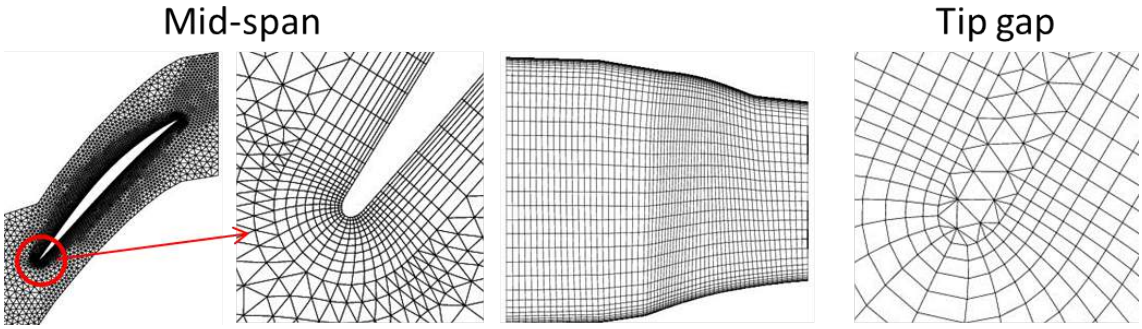

Figure 2.3: Computational grid. Mid-span, radial and tip gap meshes

Table 2.2: Grid refinement variation

Case	No. of Points	Radial Levels	Tip Gap Levels
mesh 1	165,000	35	5
mesh 2	270,000	48	6
mesh 3	480,000	61	8
mesh 4	600,000	75	11

The mapping of a whole characteristic curve is performed by changing the nozzle throat size. This allows to draw the compressor maps without having to change the boundary conditions. It is believed that, compared to the standard back pressure boundary conditions, this method allows for the simulations to approach the stall

boundary closer [38]. The three elements are joined together in a single mesh with mixing planes at the interface boundaries (see Figure 2.4). In terms of mesh size, the four cases differ only in the number of points used to resolve the rotor. Starting from the choked condition the nozzle throat area is decreased. Calculations at lower flows were restarted from converged solutions at higher flow rates, with the convergence criterion based on the residuals from the flow equations and mass flow rate. As the stall boundary is approached the back pressure is slightly increased (small reductions in nozzle throat area). This is done by means small increases of the angle γ highlighted in Figure 2.4 with a minimum variation set to 0.1°. The number of iterations for a fully converged solution increases near-stall and cases are considered to be stalled if the residuals criterion is not satisfied after a pre-specified number of iterations (typically a maximum of 10000). For a given case study, the formula used in this thesis to predict the compressor stall margin is introduced in the next chapter in Section 3.2.

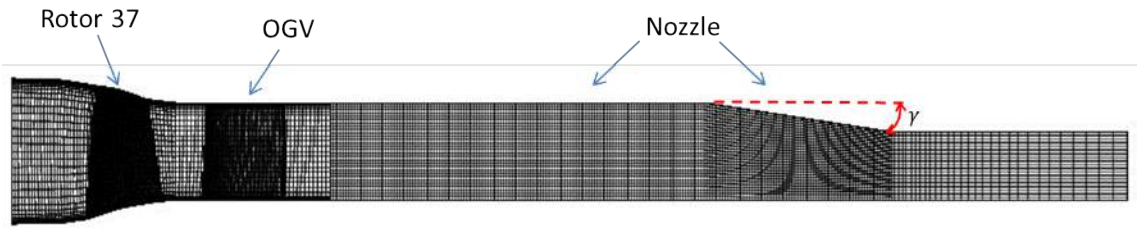

Figure 2.4: Solution domain for NASA Rotor 37

Before discussing the results, it should be clarified that the expressions *pressure ratio* and *temperature ratio* refer to ratios of total quantities. Such a terminology is used in the whole thesis. Figure 2.5 shows the rotor characteristic maps obtained with the different mesh resolutions. For each grid, the predicted choking mass flow rate resulted to be around 20.80 kg/s. In order to provide a better comparison from high to low flow range, however, the mass flow range of each characteristic curve has been normilised using the corresponding choking value. A small difference can be found in the pressure ratio map, with the finest grids (mesh 3 and mesh 4) predicting a slightly lower rotor performance. Figures 2.6 and 2.7 present a comparison of the total pressure and total temperature ratio spanwise distributions downstream of the rotor respectively at high flow (near-peak-efficiency) and low flow (near-stall)

conditions.

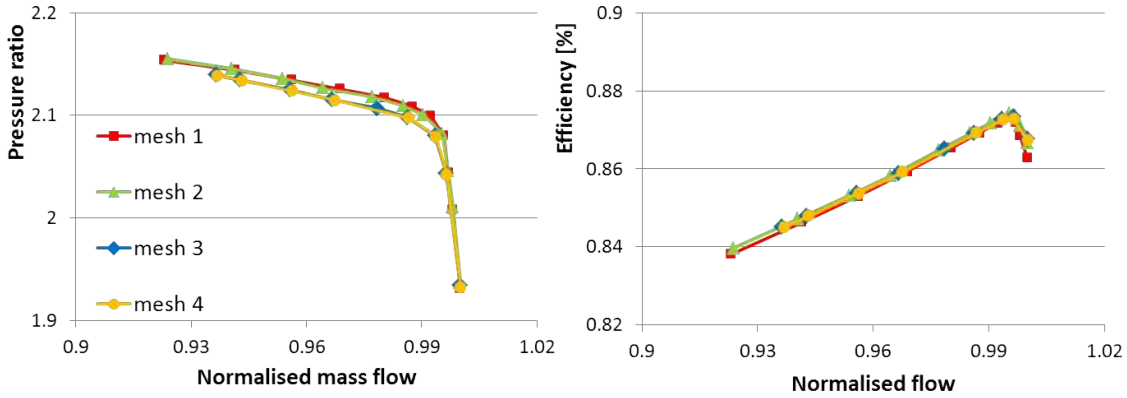

Figure 2.5: Grid independence study. Rotor maps

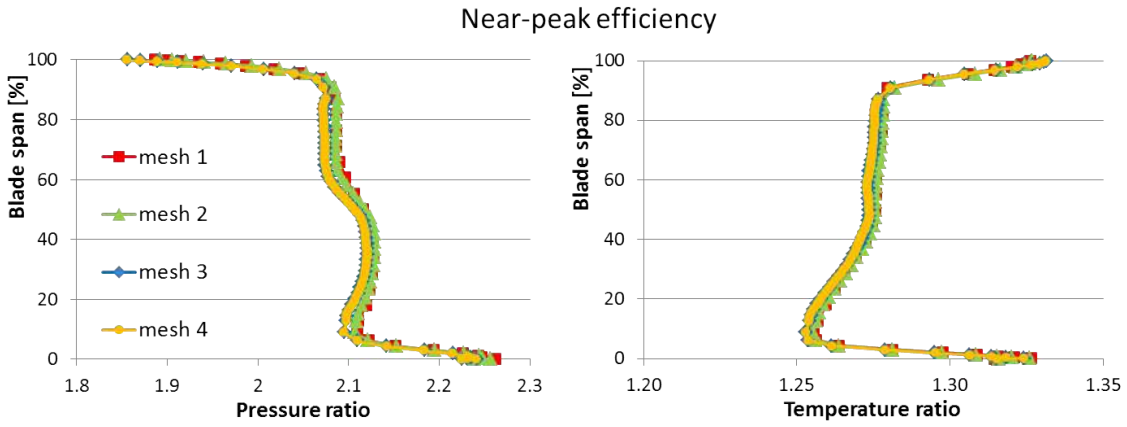

Figure 2.6: Grid independence study. Pressure and temperature ratio radial profiles at near-peak efficiency operation

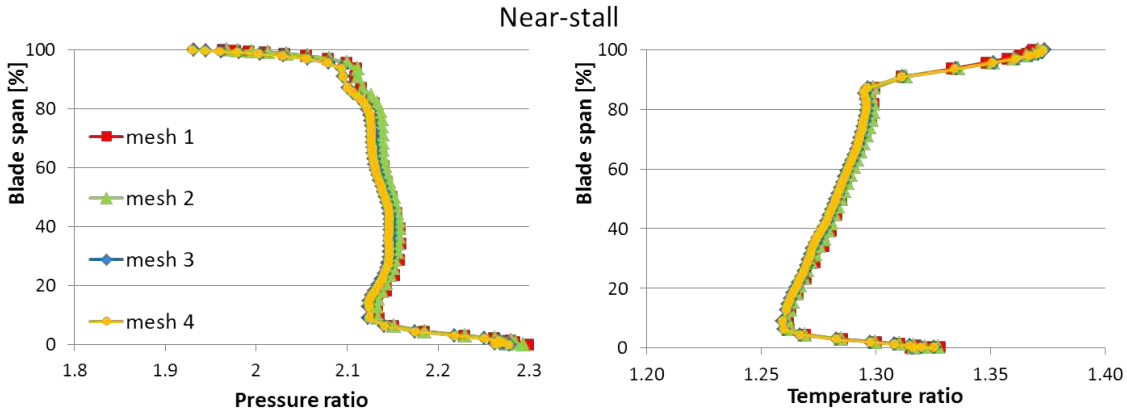

Figure 2.7: Grid independence study. Pressure and temperature ratio radial profiles at near-stall operation

No significant differences are observed among the results produced by CFD simulations, particularly in terms of profile shapes. According to the overall performance map, however, the profiles obtained with meshes 3 and 4 are slightly shifted towards lower pressure ratio values. Temperature ratios are affected in a similar way, which would explain why the calculated efficiency maps overlap. Figure 2.8 shows the blade pressure profiles extracted at 95% and 70% of span for high flow condition. Once more, no considerable variations are observed; in particular the strength and position of the shock obtained using the four different grid resolutions are very similar. Blade-to-blade flow field solutions have been extracted at the same radial levels, as shown in Figures 2.9 and 2.10. At 70% of blade span, the grid refinement does not affect the numerical solution significantly. At 95% blade span, on the other hand, the results obtained with the coarsest mesh show a slightly lower flow blockage downstream the shock in the region between the mid-pitch and pressure side. Nevertheless, as it will be also discussed in the following section, it has been observed that when comparing the presented CFD results with available experimental data the discrepancies are not improved significantly by means of further grid refinement.

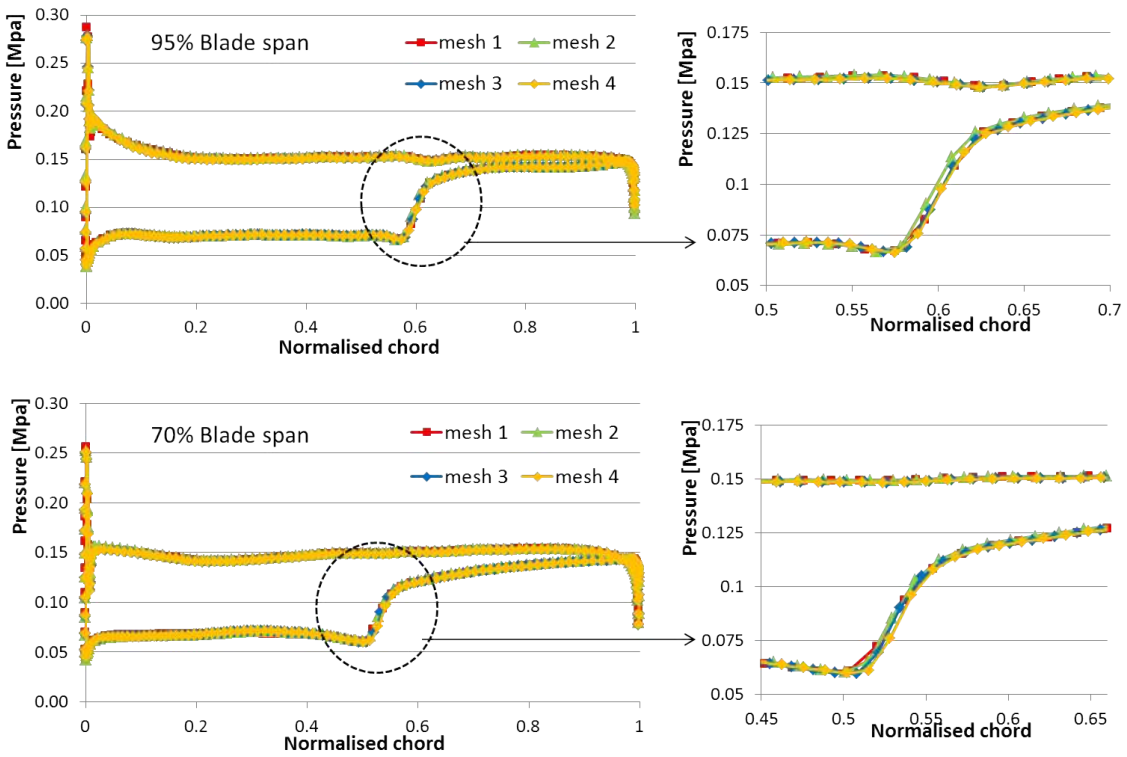

Figure 2.8: Grid independence study. Blade pressure profiles at near-peak efficiency operation (95% and 70% blade span)

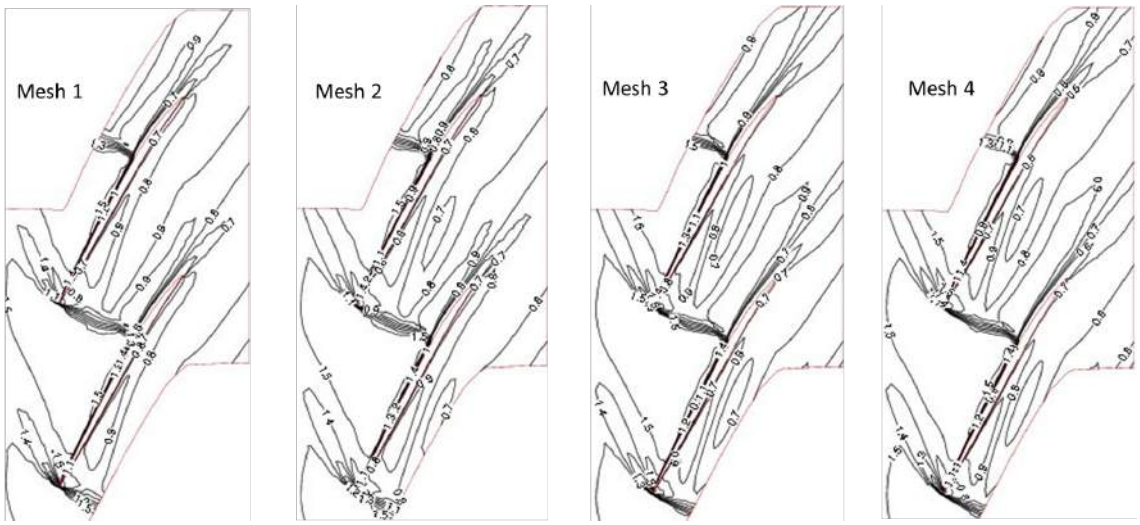

Figure 2.9: Grid independence study. Blade-to-blade Mach number contours at near-peak efficiency operation (95% blade span)

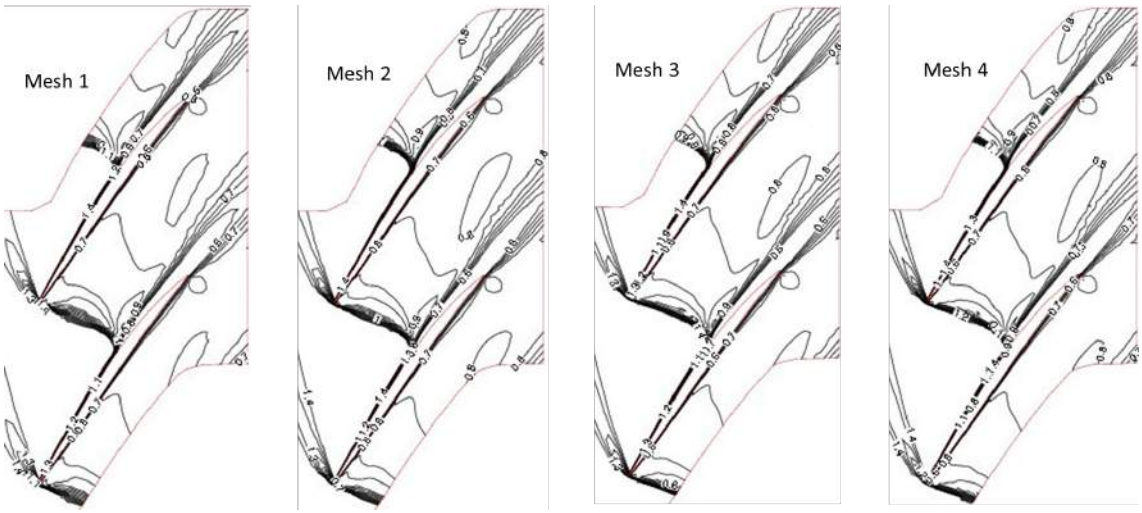

Figure 2.10: Grid independence study. Blade-to-blade Mach number contours at near-peak efficiency operation (70% blade span)

It may be therefore concluded that the numerical solution is essentially independent of the applied grid resolution. To some extent this was expected since mesh refinement typically aims to improve the prediction of the flow over the near-wall (boundary-layer) regions. By adopting a wall function, however, the viscous sublayer is avoided since the solution is "bridged" at the first control cell (assumed to be fully turbulent) with the wall properties. Wall functions are a set of semi-empirical functions, which connect the fluid velocity and temperature at a certain distance

from the wall (in the turbulent region) with the wall shear stress and heat flux respectively. It may be therefore interesting to repeat the grid independence study by removing the application of the wall function. However, this is beyond the scope of this study. Considering the relatively large difference in computational cost, the coarsest mesh will be used for the rotor re-design investigations performed in the next chapter.

2.5 Model validation

Over the past decades a large number of CFD codes have been validated using NASA Rotor 37. However, all the important aspects of the flow field have not been fully explained with numerical studies based on RANS. In particular, three specific details of measurements proved to be especially difficult to predict at design speed [45, 46, 47]:

- Most of codes under-predict the overall efficiency and slightly over-predict the pressure ratio over the high flow range operating condition.
- Most of codes fail to predict accurately the total pressure distribution downstream of the rotor.
- Most of codes calculated a higher total temperature ratio in the outer part of the blade.

The results obtained with SURF and presented in this section are those for the coarsest grid previously described. The comparison with the experimental data are performed at design speed.

As mentioned in the previous section, the numerical simulations calculated a choking mass flow rate of about 20.80 kg/s, which results 0.6% lower than measurements (20.93 kg/s). This is in agreement with most of model validation studies on Rotor 37 available in literature [45, 47]. Figure 2.11 shows rotor maps in terms of normalised flow. The results show an under-prediction of the overall efficiency and an over-prediction of the pressure ratio at high flow operating range.

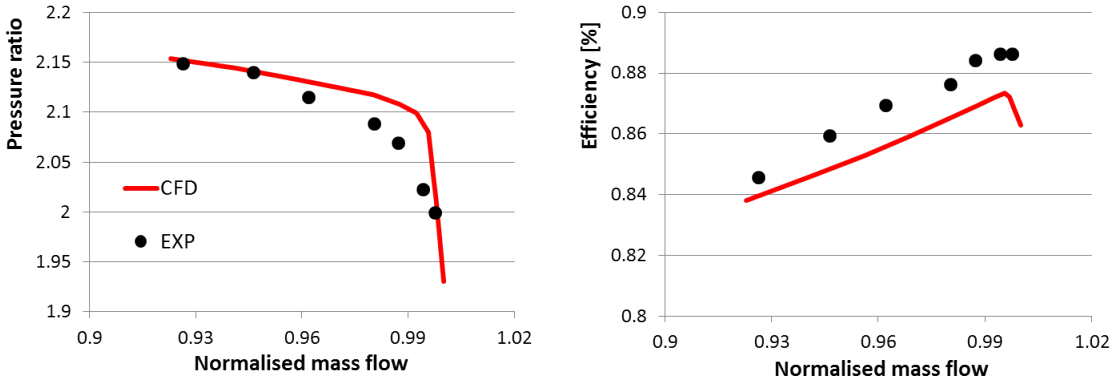

Figure 2.11: Numerical model validation. Rotor maps

The validation in terms of efficiency maps, however, should be discussed considering that CFD results are circumferentially averaged using data at all mesh points. On the other hand, as also suggested by Figure 2.12, experimental measurements may not fully include loss regions in the end wall boundary layers potentially over-predicting the efficiency. Thus, it could be argued that in terms of global rotor performance a fairly good prediction was obtained. It is however interesting to recall the argument provided by Denton et al. about the relatively good prediction in terms of overall efficiency obtained with several numerical RANS approaches, even with the use of coarse grids [45]. First of all, it is known that the two main contributions to total rotor pressure loss are shock loss and boundary layer (profile and end-wall) loss. According to the authors, while shock loss can be predicted fairly well by any solver irrespective of grid density, the viscous loss estimation should strongly depend on the applied turbulence closure and mesh fineness. One could assume, for instance, that a given computational model would under-predict the boundary layer thickening after the interaction with the shock. As a consequence, the subsonic flow downstream the shock would experience a lower acceleration so that the local mid-pitch Mach number is decreased and the shock strength is raised. Therefore, in terms of overall efficiency, the under-prediction of profile/wake losses could be somehow balanced by the over-prediction of shock losses. Such argument will be further discussed in this section using the current case study as an example.

Figure 2.12 presents comparisons of stagnation pressure and temperature ratios spanwise distributions at near-peak efficiency condition. The corresponding efficiency radial profiles are also shown.

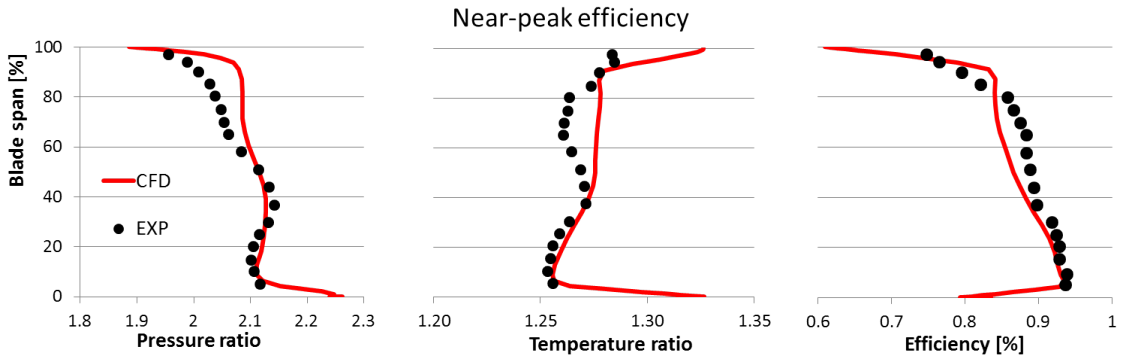

Figure 2.12: Numerical model validation. Pressure ratio, temperature ratio and efficiency radial profiles at near-peak efficiency operation

Near the hub, the measurements show a region of low total pressure that has not been generally well reproduced by numerical codes. The low-pressure region prompted much discussion in the literature and the related phenomenon is not fully understood. Hah et al. predictions [48], for instance, suggested that due to the very high aerodynamic loading of the rotor, the passage shock extends all the way down to the hub. Here, the interaction with the boundary layer causes a three-dimensional corner separation, producing the local pressure deficit. In a following work [49] the author confirmed his results by means a Large Eddy Simulation (LES) study. Shabbir et al. [50] instead related the pressure deficit to the presence of an axial gap between the upstream hub and the rotor blade in the experimental setup. The authors performed experiments and CFD studies that demonstrated an important effect of the hub leakage flow on the pressure ratio radial profile. Nevertheless, even reducing the amount of flow through the axial gap to zero did not completely eliminate the pressure deficit. On the one hand, the hypothesis that the hub pressure drop is mainly caused by the leakage flow does not explain why the pressure deficit disappears at part rotational speed [49]. On the other hand, the axial gap argument would be more consistent with the fact that most of CFD investigations neglected it and didn't detect a large corner separation, thus over-predicting the local pressure ratio [45, 50]. Unfortunately experimental measurements do not resolve the question if a significant hub corner flow separation occurs. The experimental data in Figure 2.12 shows a gradual drop of pressure rise from mid-span towards the casing. An explanation of this trend may be found in the large flow blockage detected in the core flow region by the measurements [51] and strong radial migration of the

low momentum flow region downstream of the passage shock observed in most of numerical computations. Such spanwise movement of the fluid has the effect of transporting pressure losses from the mean region of the blade towards the tip. A strong radial flow has been also predicted in this study, as shown in Figure 2.13. The figure also shows the blade-to-blade Mach contour at mid-span. The results suggest that in the mean region the flow slightly separates after the shock-boundary layer interaction and rapidly reattaches downstream. In agreement with most of CFD codes, the discussed large hub corner flow separation is not predicted by SURF. In terms of code validation, fairly good agreement is found from hub to 60% blade span, with the code predicting a low pressure region at hub although neglecting the discussed upstream axial gap. With respect to the experimental data, however, it can be noticed that the numerical simulation predicted a smaller pressure deficit.

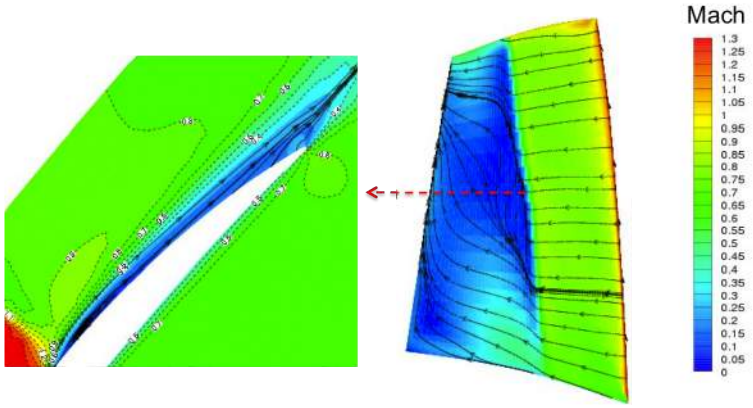

Figure 2.13: Near-wall Mach number contour with streamlines (suction side). A slight separation with reattachment after the shock is predicted at mid-span

From 60% span to the casing, instead, the numerical results show a steeper behavior than the experimental one, resulting in an over-prediction of the local pressure ratio, which justify the higher overall performance obtained at high flow condition. Similar trend can be observed in the total temperature distribution: good matching is found from hub to mid-span while CFD calculations show higher values towards the tip. Consequently, efficiency discrepancies are also observed in the outer part of the blade. It is however interesting to notice that better agreement is found in terms of efficiency, as a results of self cancellation of small discrepancies in pressure ratio and temperature ratio profiles since these are both over-predicted.

As for the high flow operation, analogous observations can be made for the pressure ratio profile calculated at near-stall (see Figure 2.14).

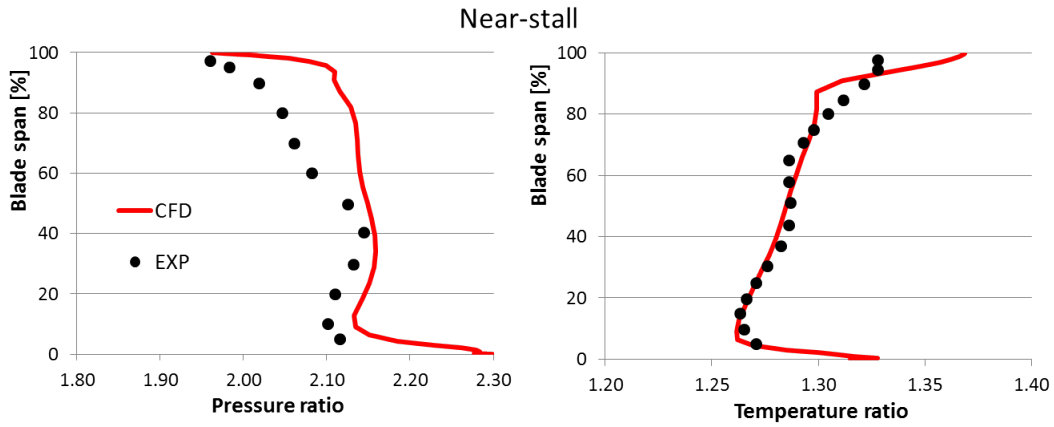

Figure 2.14: Numerical model validation. Pressure and temperature ratio radial profiles at near-stall operation

Good matching is found over the inner part of the blade while from mid-span towards the casing the pressure ratio is clearly over-predicted. Better agreement is however found in terms of stagnation temperature with the numerical results differing from measurements only over the tip region. Some of the discussed discrepancies have been obtained by several authors [45, 47, 49, 52].

Experimental data in terms of blade-to-blade relative Mach number at both high and low flow conditions at different blade span can be found in the literature [51, 53]. Figure 2.15 reports the measurements acquired by Suder. At the tip region the results show that a nearly normal passage shock exists, as indicated by an upstream and downstream Mach number of about 1.5 and 0.75 respectively. The bow shock at the leading edge is slightly detached so that the downstream flow is subsonic and rapidly accelerates around the leading edge and along the suction side until it encounters the passage shock. The vortex passing through the shock generates high flow diffusion (flow blockage), which is noticeable from the low relative Mach number region downstream the shock. As the back pressure is increased, the shock/vortex interaction (and thus the blockage) becomes stronger and moves upstream. Downstream of the shock the flow distortion increases and the low Mach number region migrates towards the pressure surface and merges with the rotor wake. At near-peak efficiency condition and 70% blade span, measurements indicate a clear

thickening of the boundary layer after its interaction with the passage shock. Despite the slight reduction of the upstream Mach number, the steep pressure gradient across the shock is still very high and cannot be sustained by the boundary layer [51]. Figure 2.16 shows the computed blade-to-blade Mach number flow fields. The results show reasonable agreement in comparison with Figure 2.15, however the comparison is difficult in these terms. A better qualitative validation is reported in Figure 2.17 using the available experimental data provided in [45]. The first plot refers to the blade-to-blade pitch profile extracted at 20% of the local chord and 50% blade span. First of all, it should be observed that the code is able to predict accurately the shock position although the shock strength seems slightly over-predicted. Agreement is also found upstream the discontinuity. Mach number calculations downstream the shock are instead lower than experimental data, indicating an under-prediction of the boundary layer thickening on pressure side after its interaction with the shock. The second plot shows the comparison of Mach number along the mid-pitch line at 50% blade span. Good agreement is found, with the model being able to predict the position of both bow and passage shocks.

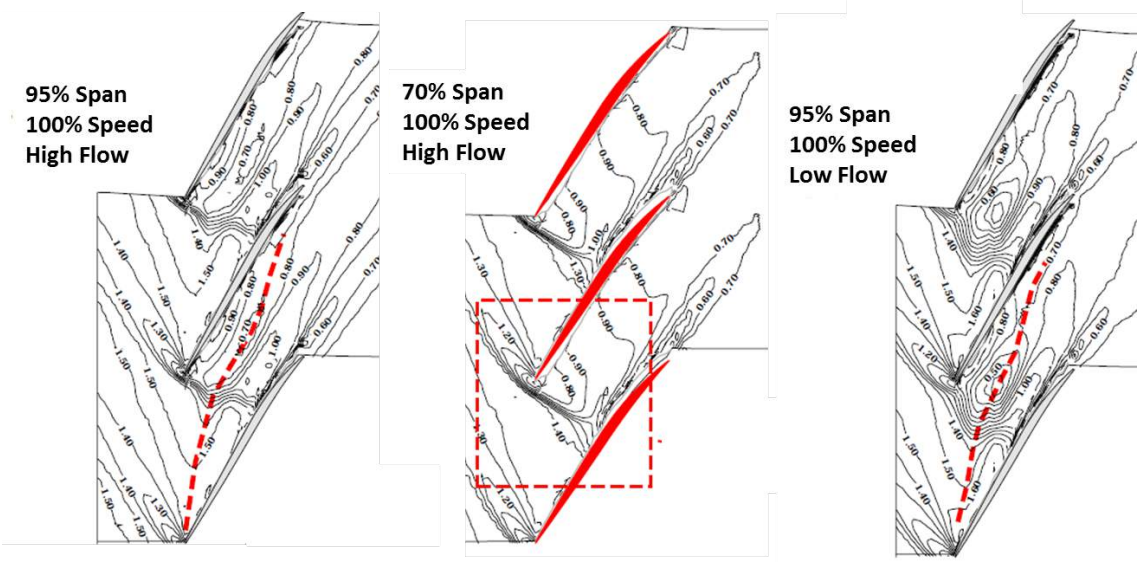

Figure 2.15: Measured blade-to-blade Mach number contours at high flow (95% and 70% blade span) and low flow (95% blade span) operation

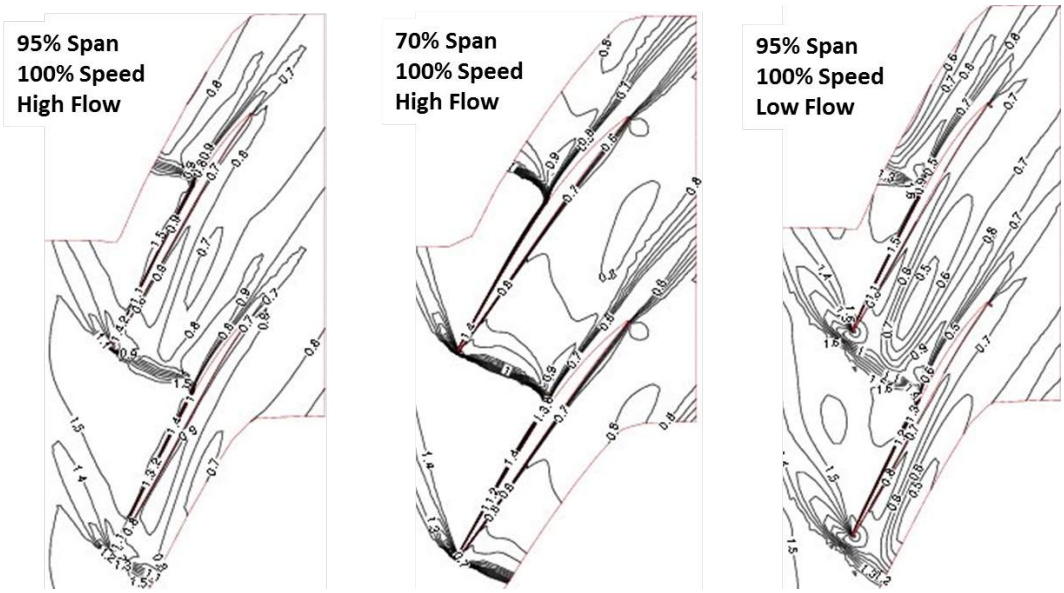

Figure 2.16: Computed blade-to-blade Mach number contours at high flow (95% and 70% blade span) and low flow (95% blade span) operation

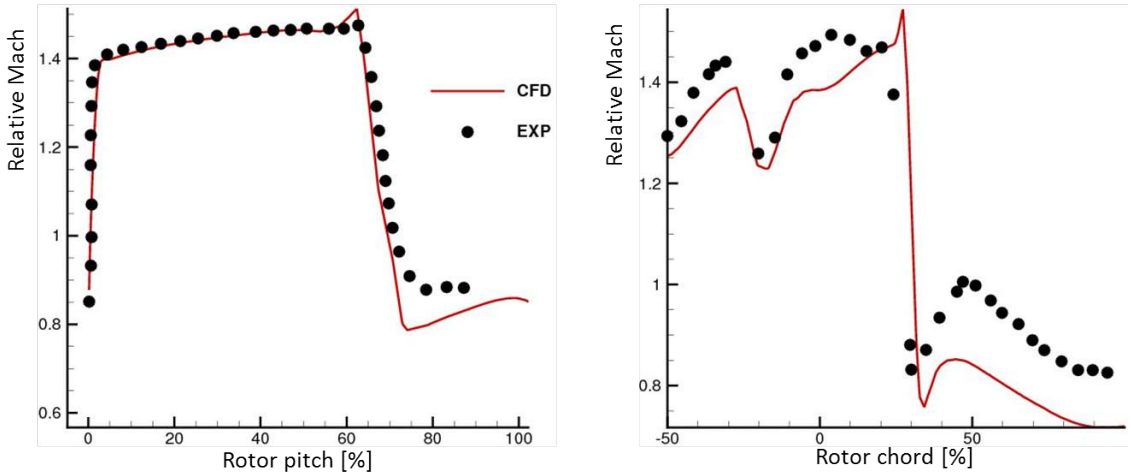

Figure 2.17: Model validation. Mid-span Mach number profiles along the rotor pitch at 20% chord (left) and mid-pitch (right) lines

Fairly good matching is also observed in terms of bow shock strength while, the passage shock is slightly over-predicted. The mid-pitch profile comparison provides further useful information in terms of shock-boundary layer interaction along the suction side. In particular, the lower increase of Mach number downstream the shock indicates a lower acceleration of the flow at mid-pitch before it diffuses towards the trailing edge. Once again, this can be mainly related to a lower predicted boundary layer thickening. Nevertheless, the general good prediction leads to good agreement between CFD results and experimental data in terms of rotor performance at mid-

span (see Figure 2.12). It may be expected however that the discrepancies observed downstream the passage shock would rise moving towards the tip, where the shock strengths and its effects increase. This is in part confirmed in Figure 2.18 where measured and predicted diffusion factor[1] (DF) spanwise variation at design condition ($\dot{m}/\dot{m}_{choking} = 0.965$) are compared. Both Leiblein and Schobeiri parameters have been calculated, indicating that accounting for compressibility effects results in higher values of diffusion factor. A fairly good comparison is observed in terms of radial averaged values. However, the predicted profile is slightly skewed backwards with respect to the measurements. Considering the high loading of the rotor, this suggests that towards the casing diffusion losses are under-predicted. This may be related to the smaller boundary layer thickening along the rear part of the blade predicted by the code.

From the above, the higher pressure ratio calculated towards the tip and observed in Figure 2.12 could be explained in terms of lower boundary-layer/wake losses at rotor exit. The prediction of a stronger shock, on the other hand, might be the reason of the higher temperature ratio and, to some extent, lower efficiency.

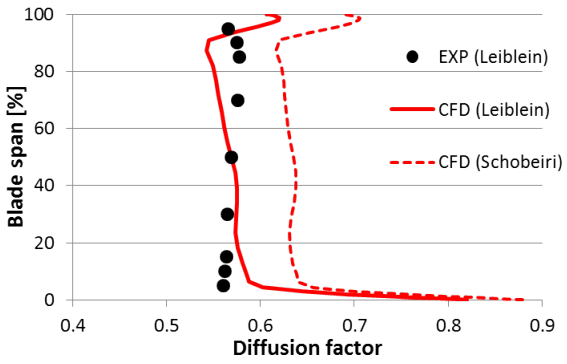

Figure 2.18: Model validation. Diffusion factor spanwise profiles at design condition

2.6 Summary

In this chapter the in-house numerical model used in the current research was described. A conventional but challenging test case was used for the code validation. Comparisons between measured data and numerical results were presented and ana-

[1]The diffusion factor will be described in the next Chapter

lysed. Predictions reported by different authors in the past were also recalled and compared with the present calculations. In agreement with most of codes, although a fairly good prediction was found in terms of global performance, discrepancies were observed when trying to resolve fine details of the flow. This was expected since CFD methods based on steady RANS calculations cannot predict accurately complex unsteady flow mechanisms such as shock/boundary layer and shock/tip leakage interactions. Nevertheless, certain mean and three-dimensional aspects of the flow field could be fairly well reproduced. It may be concluded that, despite its limitations in predicting the magnitude of complex entropy generation mechanisms, CFD turbulence modelling can provide useful insight and good qualitative understating of 3D flow features. Therefore it represents a powerful tool to the turbomachinery designer, particularly when trying to predict the trend of any changes.

Chapter 3

Transonic blade radial stacking line modifications

3.1 Introduction

In this chapter, blade geometry modifications that are considered as relevant for the purpose of the current research are explored. NASA Rotor 37, presented in the previous chapter, is used as test vehicle. First, the effect of stagger angle variation on rotor mass flow rate and performance is taken into account. The effect of applying blade sweep and lean on rotor stability margin is analysed. The main purpose is to explore the techniques that might contribute to achieve an efficient new geometry for the H2-IGCC gas turbine compressor. A possible re-design configuration of Rotor 37 to cope with a hypotethical syngas combustion is presented in the last section.

On the basis of the study discussed in the previous chapter, the design investigations performed in this work rely on the fact that the predicted changes in performance, obtained as a result of reference geometry modifications, can be considered correct and significant information.

3.2 Stage loading and flow diffusion

This section briefly describes some of the basic parameters that are used in the current thesis in order to investigate blade/stage performance variations due to modifications applied to a given baseline geometry. Flow velocities and angles, as

well as geometrical blade parameters, are also defined.

Two of the fundamental equations that describe an axial compressor stage performance are Euler equation and stage pressure ratio equation as a function of the compressor process efficiency. Referring to figure 3.1, these can be expressed respectively as:

$$\Delta h_0 = c_{p,a}\Delta T_0 = u_2 c_{w2} - u_1 c_{w1} = u c_a(\tan\beta_2 - \tan\beta_1) \tag{3.1}$$

$$\frac{p_{03}}{p_{01}} = \left(1 + \eta_{is}\frac{\Delta T_0}{T_{01}}\right)^{\frac{\gamma}{\gamma-1}} \tag{3.2}$$

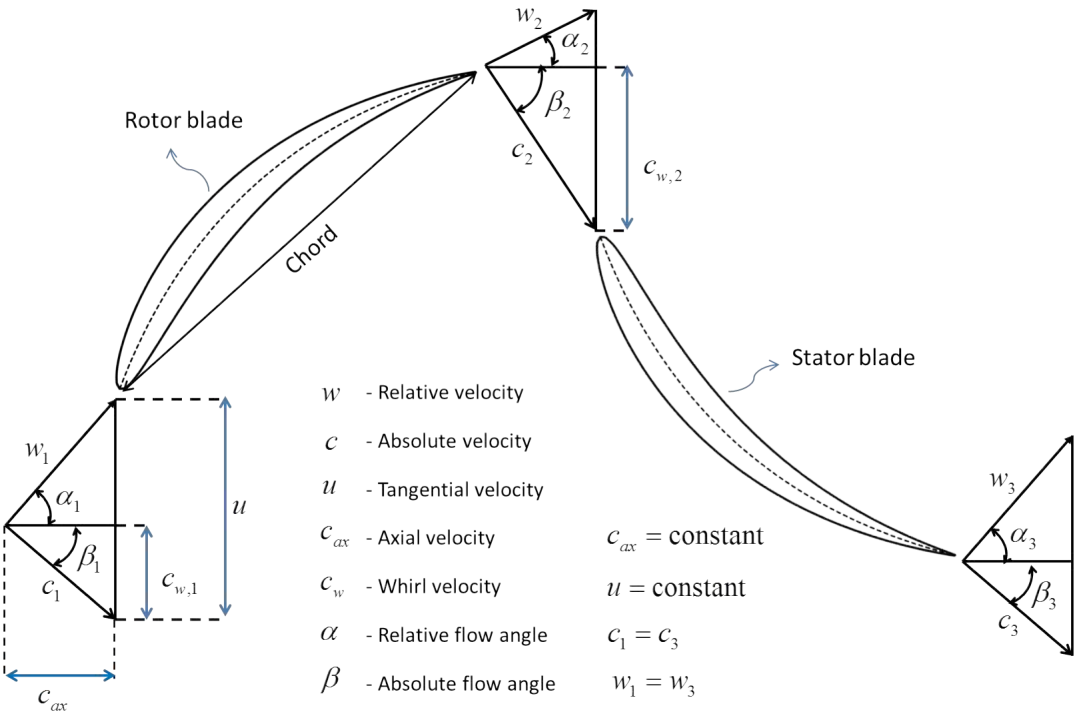

Figure 3.1: Compressor stage velocity diagrams

where Δh_0 and ΔT_0 are the specific stagnation enthalpy and stagnation temperature variations across the stage, η_{is} is the isentropic efficiency, β is the absolute

flow angle, u is the tangential velocity, c_a is the axial velocity and c_w is the whirl velocity. The subscripts 1 and 3 refer to inlet and outlet sections of the stage, while the subscript 2 refers to the rotor outlet (and stator inlet) section. The equality $\Delta h_0 = uc_a(\tan\beta_2 - \tan\beta_1)$ in Equation 3.1 is derived assuming the axial and tangential velocities constant across the stage. In addition, a typical design condition is that the air leaves the stage with the same absolute velocity with which it enters (i.e. $c_3 = c_1$).

From the above relations, by combing high blade speed, high axial velocity and high rotor flow deflection $(\tan\beta_2 - \tan\beta_1)$, it would be possible to reach high total temperature rise for a given stage. This would minimise the number of stages needed in order to reach a required overall pressure ratio. It is known however that high flow deflection means high rate of flow diffusion and stage loading coefficient $(\psi = \Delta h_0/u^2)$, the amount of which is limited by the increase of boundary layer losses and possible flow separation. In the past, several correlations have been developed to produce generalised profile loss characteristics due to flow diffusion on blade suction surface. One of the most important correlations was introduced by Lieblein in the 1950′s, the development of which was based on the theoretical velocity distribution measured on a wide range of subsonic cascade airfoil geometries (NACA 65 series and British C4 series) [54]. The correlation between a loss parameter (LP) and the diffusion factor (DF) is illustrated in figure 3.2.

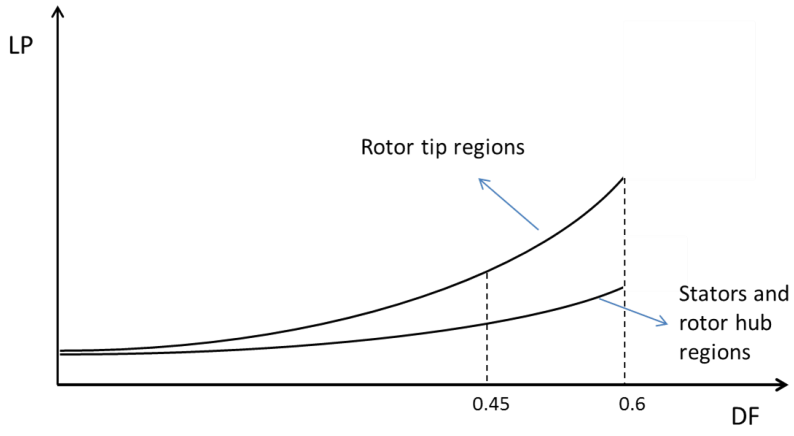

Figure 3.2: Loss parameter and diffusion factor correlation

The DF is defined as:

$$DF_{rotor} = \frac{w_{max} - w_2}{w_{max}} \tag{3.3}$$

$$DF_{stator} = \frac{c_{max} - c_3}{c_{max}} \tag{3.4}$$

where w_{max} and c_{max} are the maximum flow velocities along the suction side of rotor and stator respectively and w_2 and c_3 are shown in Figure 3.1. Since the calculation of the peak velocity could be tedious and time-consuming, the DF was approximated based on the inlet and outlet flow conditions. With reference to Figure 3.1, the analytical expressions of DF and LP are reported in Equations 3.5 and 3.8.

$$DF_{rotor} = \left(1 - \frac{w_2}{w_1}\right) + \frac{r_2 c_{w,2} - r_1 c_{w,1}}{(r_1 + r_2) w_1 \sigma} \tag{3.5}$$

$$DF_{stator} = \left(1 - \frac{c_3}{c_2}\right) + \frac{r_3 c_{w,3} - r_2 c_{w,2}}{(r_2 + r_3) c_2 \sigma} \tag{3.6}$$

$$LP_{rotor} = \frac{\xi_r \cos \alpha_2}{2\sigma} \tag{3.7}$$

$$LP_{stator} = \frac{\xi_s \cos \beta_3}{2\sigma} \tag{3.8}$$

where α is the relative flow angle, ξ_r and ξ_s are the relative and absolute total pressure loss coefficient across rotor and stator blade passages respectively, r is the

blade radius and $\sigma = l/s$ is the solidity, i.e. the chord length (l) to blade pitch (s) ratio. For a given blade-row, the blade pitch can be defined as the distance between the leading edges of two adjacent blades. The first term on the right-hand-side of Equations 3.5 and 3.6 indicates the mean deceleration of the flow, while the second term represents the flow turning. The results obtained by Lieblein show that for rotor hub regions and stator blades the profile losses are not highly affected by the variation of DF up to values of 0.6. Above this critical value an abrupt arise of the losses is generally observed, often indicating the existence of large separated flow regions. At rotor tip region, on the other hand, profile losses might start to increase rapidly at values of DF above 0.45 even though flow may not be separated. Although these results were obtained from cascade test data of specific airfoil shapes, they were found to be useful also for transonic and supersonic blades as long as shock losses are considered [55]. More complex correlations between pressure profile loss and flow diffusion can be found in the literature. For instance, Koch [56] reported the existence of a wider variation in the stall limiting diffusion related to the end-wall effects such as tip clearance and blade aspect ratio. Lei et al. [57] added to that the effect of skewed incoming boundary layers. Nevertheless, the DF introduced by Lieblein is still considered to be a useful parameter for preliminary design, primarily because of its simplicity, so that expressions 3.3-3.6 have been accepted and widely used by compressor designers. In a recent work Schobeiri provided a different version of the Lieblien DF by introducing an additional term that takes into account the change of density and the axial and tangential velocities are not assumed constant through the blade passage [58]. The modified expression for a rotor blade is:

$$DF_{m,rotor} = DF_{rotor}[1 - \frac{1}{\mu}\frac{sin\alpha_1}{sin\alpha_2}M_1^2(\frac{1}{\mu}\frac{sin\alpha_1}{sin\alpha_2} - 1)] \tag{3.9}$$

where M_1 is the rotor inlet Mach number and:

$$DF_{rotor} = 1 - \frac{1}{\mu}\frac{sin\alpha_1}{sin\alpha_2} + \frac{\chi sin\alpha_1}{\sigma(\chi+1)}[\frac{1}{\mu\chi\phi}(1-\chi^2) - cot\alpha_1 + \frac{1}{\mu\chi}cot\alpha_2] \tag{3.10}$$

$$\phi = \frac{c_{a2}}{u_2} \ , \ \chi = \frac{u_1}{u_2} \ , \ \mu = \frac{c_{a1}}{c_{a2}} = \frac{w_{a1}}{w_{a2}} \tag{3.11}$$

The concept of DF is used in this thesis as one of the tools to discuss performance variations when a baseline geometry is modified. Lieblein however never referred to the DF at incidences other than optimum efficiency. Nevertheless the utility of the correlation between the DF and LP parameters has been also assessed by following calculations performed at other incidences than design values, within a range of $\pm 2^{\circ}$ [59]. In this thesis Equation 3.9 is used since it is considered more accurate, particularly at high inlet Mach numbers. Expressions 3.5 and 3.6 are also used when validation cases are presented.

In the context of the current work it is necessary to attempt an estimation of the change in stability margin when geometry modifications are applied. Several definitions of the surge margin exist in literature. For instance, an expression widely used is $SM = (PR_{sp} - PR_{wp})/PR_{wp}$, where PR_{wp} and PR_{sp} are the pressure ratios at working and stall points respectively. In this work, however, one of the definitions suggested by Cumpsty is used [59]. This considers the variation of an outlet flow function $F_{out} = \dot{m}\sqrt{c_p T_{02}/p_{02} A}$ as reported in Equation 3.12. According to the author, using the F_{out} function would provide a measure of the throttle area changes necessary to take the compressor to stall. Considering that in this study geometrical modifications are applied to a given reference geometry, it is believed that using expression 3.12 would be more appropriate. For each case study performed in the thesis, the values of total temperature and total pressure used to predict $F_{out\,sp}$ in Equation 3.12 are those obtained with the last converged numerical simulation.

$$SM = \frac{F_{out,\,wp} - F_{out,\,sp}}{F_{out,\,wp}} \tag{3.12}$$

Another important design parameter is represented by the degree of reaction (DoR), which provides a measure of how the pressure rise (and to some extent the diffusion) across a given stage is divided between the rotor and stator. It is usually defined as rotor static enthalpy rise to stage static enthalpy rise ratio, as indicated

in Equation 3.13.

$$DoR = \frac{h_2 - h_1}{h_3 - h_1} \tag{3.13}$$

3.3 Stagger angle

Figure 3.3 illustrates the definition of blade stagger angle (ζ) and common convention of positive stagger variation.

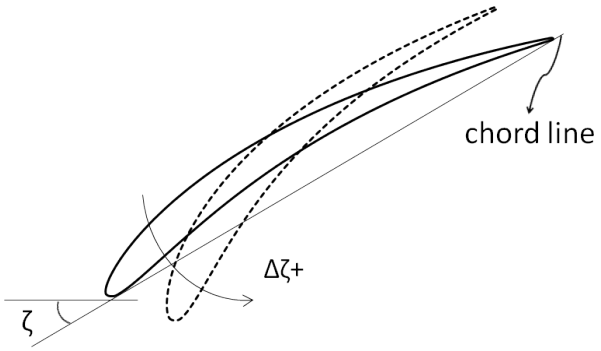

Figure 3.3: Definitions of stagger angle and its positive variation

It is known that rotor blade stagger angle increases towards the tip because of the higher tangential velocity. At a given radial level, the stagger position is function of the corresponding inlet and outlet blade angles ($\alpha_1^{'}$ and $\alpha_2^{'}$) calculated in order to achieve the required incidence (i) and deviation angle (δ) at design condition (see Figure 3.4). For a given rotor blade, the incidence and deviation angles are defined as follows:

$$i = \alpha_1 - \alpha_1^{'} \tag{3.14}$$

$$\delta = \alpha_2 - \alpha_2^{'} \tag{3.15}$$

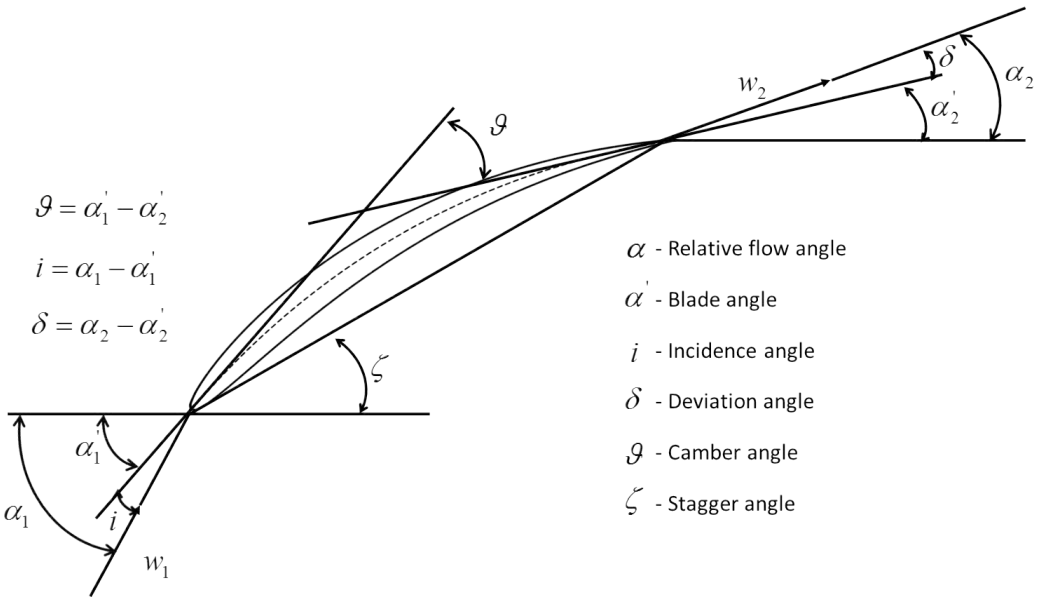

Figure 3.4: Rotor blade and flow angles definitions

Stagger angle variation can be considered as major parameter to control the passage area of a given reference blade. In particular, a positive variation means that the passage is closed by rotating the blade around its geometric centre, which results in a reduced inlet mass flow rate.

The baseline rotor has been re-staggered by 3° and 5° in both positive and negative directions, for the purpose of providing an insight on stagger angle variation effects on transonic blade performance. The simulations were performed with small increases of the back static pressure approaching the surge line, with the minimum variation set to 0.125%. Figure 3.5 shows the obtained rotor maps. For each characteristic curve, the near-peak efficiency point (black point in the figure) has been assumed to be the working point. It corresponds to 98.5% of the relative choking mass flow rate. Observing the rotor maps, the change in choking mass flow rate by stagger variation is clearly noticeable. Furthermore a general increase in efficiency and decrease in pressure ratio are obtained through positive stagger. Opposite arguments can be made for the opened blade configurations. Figure 3.5 indicates that further increases in stagger angles result in minor efficiency improvements, eventually leading to a drop in performance. Stall margin variations with respect to the reference value have been calculated and the results show that the original rotor

stability reduces for each re-staggered configuration (see Table 3.1). When comparing these values it should be however considered that the selected working point pressure ratios are different. Nevertheless, Figure 3.5 clearly indicates that the mass flow range becomes narrower as the blade is closed from its original setting.

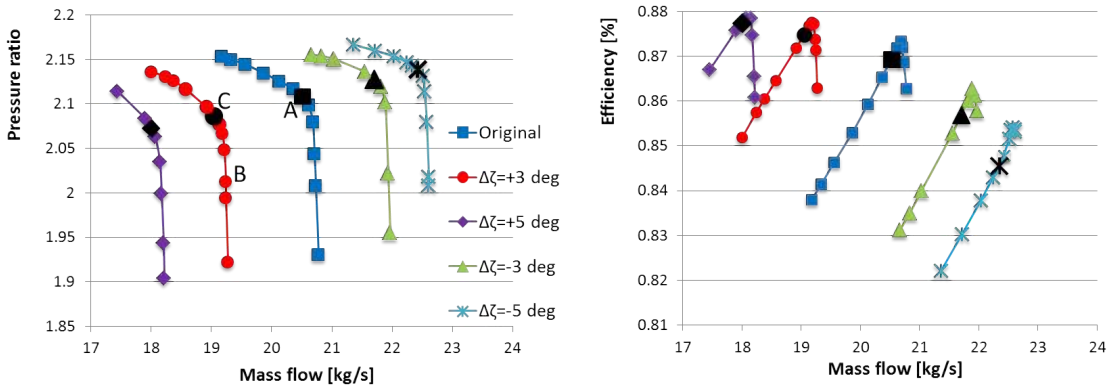

Figure 3.5: Effect of blade re-stagger on rotor maps

Table 3.1: Effect of blade re-stagger on surge margin predictions

$\Delta\zeta = +5°$	$\Delta\zeta = +3°$	$\Delta\zeta = -3°$	$\Delta\zeta = -5°$
-37.2%	-10.0%	-30.3%	-37.2%

An important factor that should be first highlighted is that the near-peak efficiency points corresponding to the different configurations are obtained at different back static pressures. For example, due to the reduction in mass flow rate (and thus dynamic pressure), the application of the baseline Rotor 37 working point back pressure (point A in Figure 3.5) to the $\Delta\zeta = +3°$ re-staggered geometry leads to a much lower pressure ratio (point B in Figure 3.5). In particular the rotor operates at choking condition. Therefore, at the new nominal point (point C in Figure 3.5) the flow is subjected to much higher adverse pressure gradient than the reference case. Given that, in order to discuss the illustrated variation in performance, the effect of blade stagger modification on inlet flow condition is firstly considered. From Figure 3.4 it can be deduced that for a given positive stagger angle variation the blade inlet angle would increase by the same amount. Simultaneously, the decrease of axial velocity together with the unchanged tangential velocity would lead to higher relative

inflow angle, as illustrated in Figure 3.6. Thus, theoretically, the effect of positive stagger variation on rotor incidence will depend on the increase of flow angle with respect to the blade angle increase, i.e. $\Delta i = \Delta\alpha_1 - \Delta\alpha_1'$. Figure 3.7 shows the radial incidence variation with respect to the original value obtained in this study. It can be noticed that for positive stagger the incidence angle reduces and the reduction is higher for higher stagger angle modifications. In addition, a non linear trend from hub to tip can be observed, where greater changes of incidence occur towards the tip.

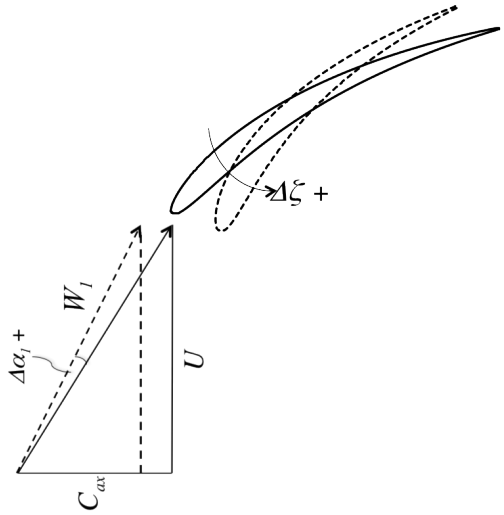

Figure 3.6: Effect of blade positive re-stagger on inlet velocity triangle

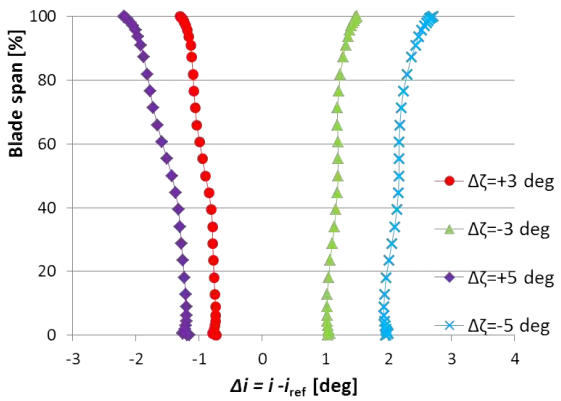

Figure 3.7: Effect of blade re-stagger on radial incidence profiles at near-peak efficiency operation

Such radial profile can be in part explained considering that the pitch-chord

ratio increases towards the tip. By applying a constant positive stagger would cause the passage area at the hub region to close quicker [60]. It should be added that the lower tangential velocity of hub regions causes higher positive changes of inflow angle with respect to tip sections. Considering the existing higher back pressure, which characterises the positive re-staggered geometries, such effect is beneficial at the tip. Opposite conclusions can be applied to the negative stagger case.

Figure 3.8 illustrates the radial distribution of pressure ratio and efficiency. It can be observed that the efficiency generally increases along the whole span when closing the blade. This should be mainly attributed to the lower relative inflow velocity (see Figure 3.6) and flow acceleration along the front part of the suction side (decrease of incidence), which mean a reduction in friction losses and, in case of transonic flow, shock losses (see Figure 3.9). In addition, a lower boundary layer thickening due to the interaction with the shock is expected.

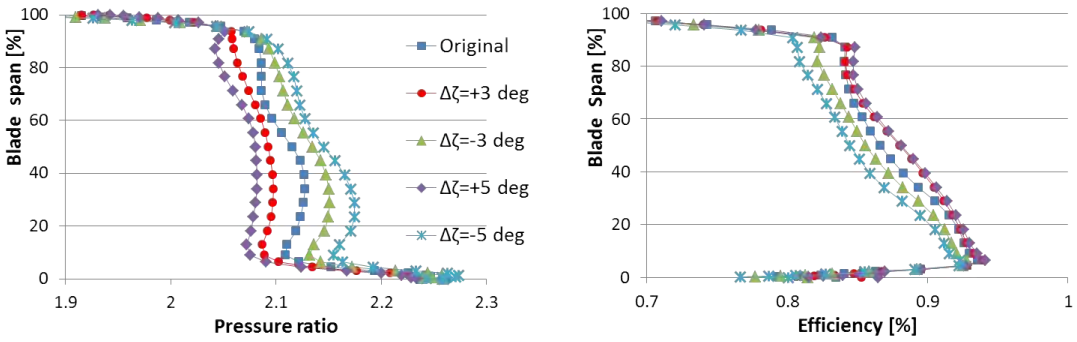

Figure 3.8: Effect of blade re-stagger on performance radial profiles at near-peak efficiency operation

The effect on profile losses, however, is not so straightforward. Due to the different compressor outlet boundary conditions and changes in effective blade passage area, the flow undergoes different diffusion processes. As shown in Figure 3.5, it is expected that the flow operating at point C would be subjected to much higher diffusion than the flow operating at point A. Within the limit of the accuracy provided by the prediction of DF, this can be further discussed observing Figure 3.10. In the case of positive stagger, the much lower outlet axial velocity leads to a increase of the absolute outlet angle and thus flow deflection ($\tan \beta_2$) with respect to the reference geometry.

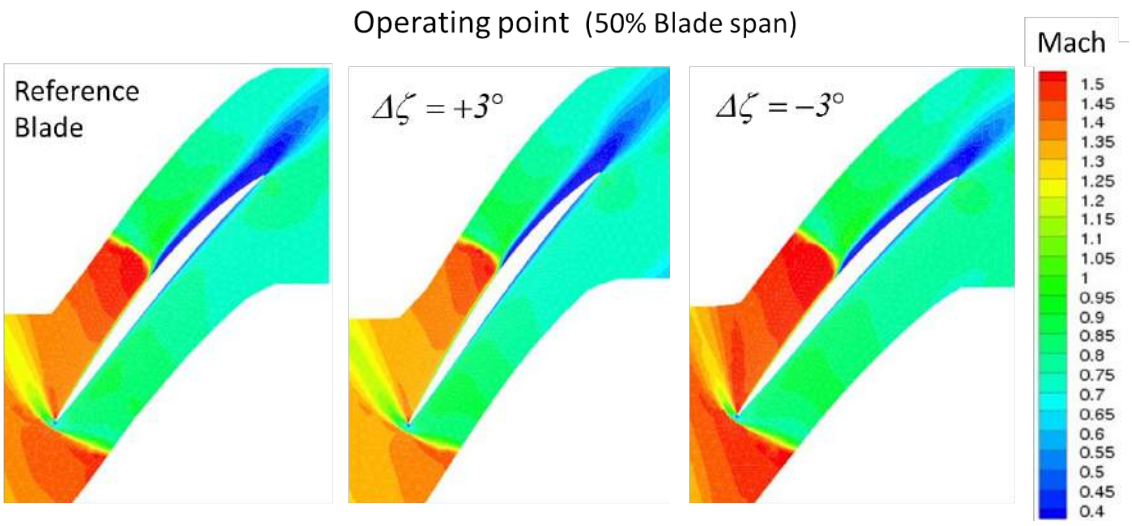

Figure 3.9: Effect of blade re-stagger on blade-to-blade Mach number contours at near-peak efficiency operation (50% blade span)

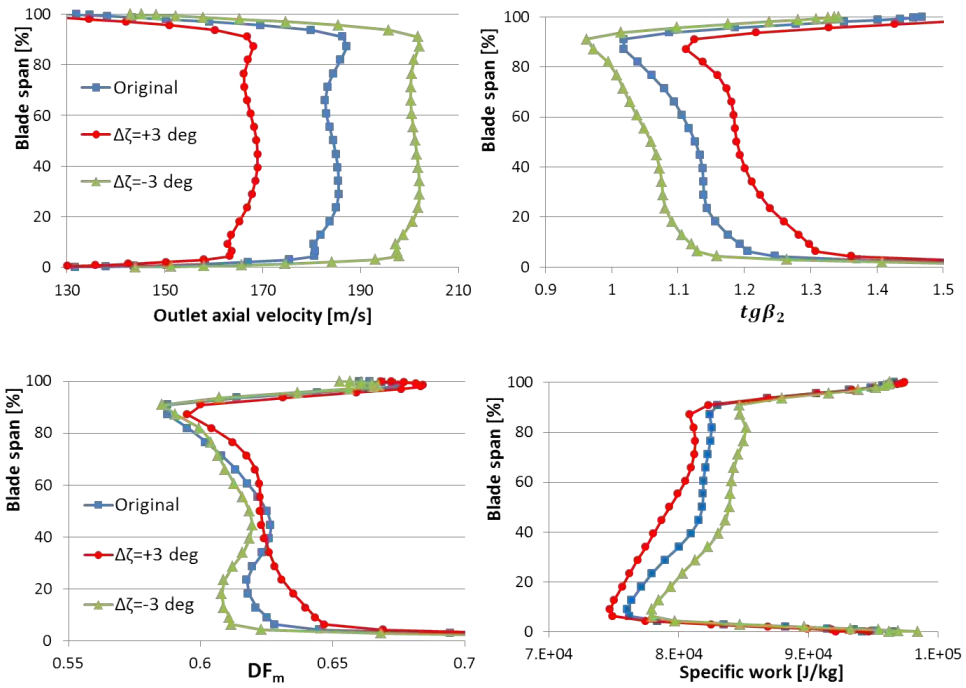

Figure 3.10: Effect of blade re-stagger on DF, specific work and outflow condition spanwise distributions at near-peak efficiency operation

Along the span, however, the increase in DF is not equally distributed. In particular, clear variations occur only towards hub, while from mid-span towards casing less differences exist between the profiles. This is believed to be related to the aforementioned changes in incidence angles at tip and strong influence of

the shock on boundary layer thickening. Considering the profile predicted for the opened blade, for instance, the stronger shock and higher incidence towards the tip might balance the much lower back pressure in terms of DF values. Nevertheless, the general rise in diffusion observed when the blade is closed would explain the increase in pressure ratio map steepness over the low flow velocity. Approaching the surge line small reductions in mass flow rate result in sharp increases in pressure rise leading the rotor to an early stall. Such sharp increase in pressure rise for small mass flow variations at low flow condition was also observed by Yoon et al. [61] and Ramakrishna et al. [60]. Although the current investigation refers to only a rotor blade, other useful information in Figure 3.10 is provided by the variation in specific work (and thus stage loading). For instance, as also indicated by the increase in outlet absolute angle, lower stage loading suggests that the flow at the inlet of a hypothetical downstream stator would be characterised by higher incidence and diffusion compared to nominal condition.

In addition to Figure 3.9, the mentioned effects on shock/profile losses are also illustrated in Figures 3.11 and 3.12 through blade-to-blade Mach contours at hub and tip. As the blade is opened, the increase of relative inflow velocity and flow acceleration around the leading edge can be noticed. On the other hand, however, despite the existence of a stronger shock, the low momentum region along the rear part of the blade and downstream the trailing edge is reduced.

According to the above, the similarity in radial efficiency profiles between the two positive stagger configurations ($\Delta\zeta = +5°$ and $\Delta\zeta = +3°$) observed in Figure 3.8 can be seen as a result of different loss mechanisms. More in general it could be discussed that for small stagger angle modifications, the main effect would be probably the decrease of leading edge and shock losses. For higher stagger angle changes the reduction in shock losses seems instead to be balanced by the rise of profile (diffusion) losses.

The pressure ratio drop observed in the case of positive stagger should be mainly related to the reduction of the axial velocity and thus specific work. Recalling Equation 3.1 and 3.2 this is further highlighted considering the discussed increase in efficiency and flow deflection, and that the current case is characterised by an axial inlet flow ($c_{w1} = 0$). The reduction in shock strength would also suggest a decrease

in pressure rise along the span. On the other hand, however, it should be again considered the counter effects on boundary layer thickening and thus consequent wake (and pressure ratio) loss. These non-linear effects are usually difficult to interpret from a qualitative analysis. In this case, however, these are believed to have minor impact, since the variation in mass flow rate should play the major role in terms of pressure ratio variations.

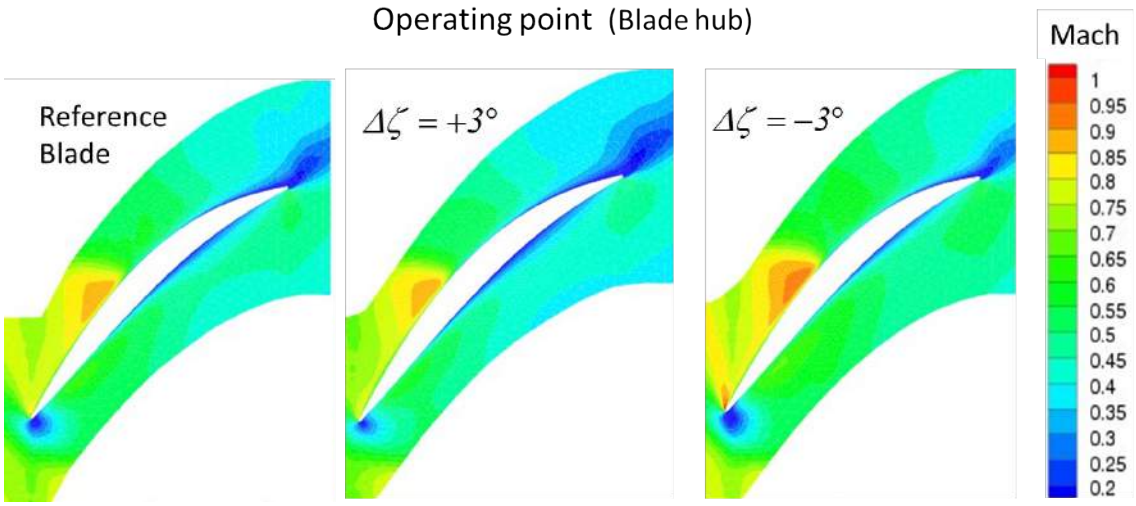

Figure 3.11: Effect of blade re-stagger on blade-to-blade Mach number contours at near-peak efficiency operation (hub section)

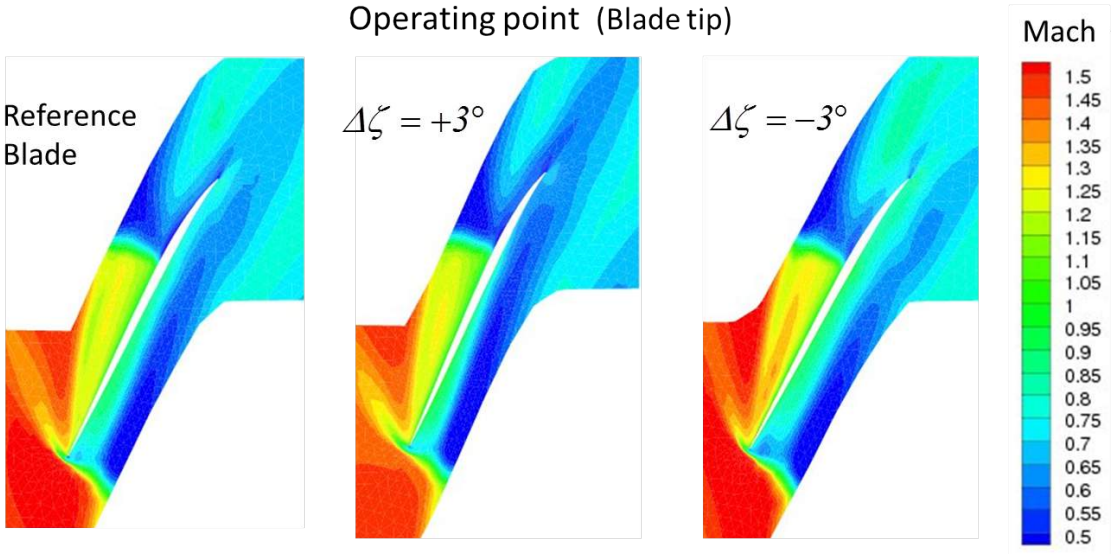

Figure 3.12: Effect of blade re-stagger on blade-to-blade Mach number contours at near-peak efficiency operation (tip section)

3.4 Sweep and lean

The introduction of transonic axial compressors has led to the development of new blade design techniques with the aim of improving the aerodynamic behaviour of the three dimensional flow. Recently the application of sweep and lean has gained wide interest, resulting advanced technologies to enhance the performance of transonic compressor stages. However, despite the large number of investigations that have been published, there are still some uncertainties about the overall effects in axial compressor design. Two different definitions of sweep and lean can be found in literature. A common choice is to define sweep and lean as the movements of blade sections in the axial and tangential directions respectively. In the other case, sweep and lean are defined to be moving the blade sections along the chord line and perpendicular to the chord line respectively. In this study, the modifications referring to the first and second definitions are used as axial sweep/tangential lean and true sweep/true lean respectively. In both cases, blade sweep is considered to be forward if the sections close to casing result curved upstream. On the other hand, blade lean is taken to be positive if tip sections are tangentially skewed towards the direction of rotation. Such definitions are illustrated in Figures 3.13 and 3.14. The two techniques will be discussed separately in the following subsections.

3.4.1 Sweep

In analogy with supersonic aircraft swept wing, the original idea of transonic blade sweep was to reduce the shock losses by decreasing the upstream Mach number component normal to the shock. It was however soon observed that the analogy was not very accurate. Several numerical and experimental tests on transonic rotors and fans revealed that beneficial effects on rotor efficiency were obtained mainly by positive sweep [62, 63, 64]. The improvement in efficiency was mostly related to the effect produced by blade sweep on shock position and structure. As described by Hah et al. (1998), for example, the passage shocks tend to remain normal to the end-wall so that if positive sweep is applied, the shock at the tip moves downstream. This would typically lead to a delay in the tip vortex-shock interaction, reducing the tip entropy generation. However, if the shock is moved too close to the trailing

edge the risk of boundary layer separation might be encountered.

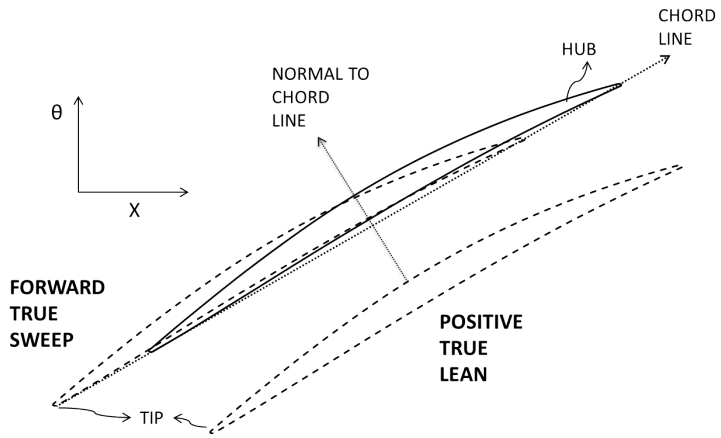

Figure 3.13: True sweep and lean definitions

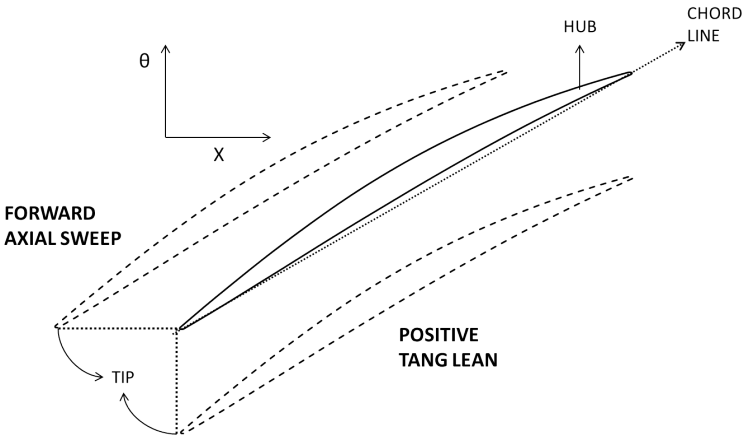

Figure 3.14: Axial sweep and tangential lean definitions

Nevertheless, it should be recalled that the gain in efficiency was not always considerable. For instance, a numerical investigation performed by Denton and Xu [65] on a transonic fan did not show noticeable influence of blade sweep on efficiency. In this regard, some investigations available in the literature did not specify if other design changes have been applied. This might complicate the understanding of the effects of individual design features. Denton and Xu also pointed out the difference of the effect produced by the shock in a rotor blade compared to an aircraft wing. It is well known that transonic rotor blades have very low camber at the tip region so

that the local pressure rise occurs almost entirely across the shock wave. Reducing the shock strength by sweeping the blade would result in lower pressure ratio. Thus, assuming that a swept blade-row is designed for the same duty of the reference blade, the flow must undergo higher flow subsonic diffusion downstream the shock. This means higher boundary layer losses so that the effect of blade sweep design on the efficiency is not obvious.

Despite such uncertainties, from the mentioned investigations it was however clearly observed that blade sweep could significantly affect the surge margin. In particular, forward sweep showed positive effect on stability range, while the opposite was generally found for backward sweep. First of all, the possibility of moving the shock position downstream would lead to rotor stability enhancement. Another important reason of stall margin improvement was attributed to the observed reduction of blade loading (in terms of static pressure coefficient) in the front part of blade tip regions [65, 66, 67]. This leads to a weaker tip leakage vortex that generates at the leading edge and thus reduced vortex-shock interaction, which is believed to be the main trigger for stall inception. As suggested by Denton et al. [65] and further discussed by Gallimore et al. [68], the reduction of tip leading edge loading can be understood considering that the spanwise pressure gradient is usually much smaller than the pressure gradient in the blade-to-blade direction. It could be assumed that the pressure profile distribution acting some distance away from the casing is imposed on the end-walls. Thus, positively swept tip sections moves the front part of the blade towards regions with lower pressure difference between suction and pressure sides. The opposite is expected along the trailing edge. More in general, by applying an appropriate blade radial stacking line modification it could be possible to optimise the matching of the loading along the blade span, as a result of spanwise pressure gradient re-distribution. In addition to the stability improvement, this would also allow for an enhancement in the balance between centrifugal and radial pressure forces in order to attenuate secondary flows [69, 66, 70]. As a consequence, the accumulation of low momentum flow region at the tip could be decreased, leading to further significant reductions in end-wall losses. This may however occur at the expenses of higher mid-span region losses. The net effect should depend on the original design flow features and it may contribute to explain why some studies

experienced a clear increase in efficiency while some others didn't. As in most of the investigations, in this work the chord-wise sweep definition was applied. This is preferred since the related stacking line modification does not introduce additional spanwise forces, while any movement in the direction normal to the chord would introduce such forces. No optimisation was performed and no attempt was made to improve the design for the new flow behavior. All the other design parameters and boundary conditions are kept the same for all the cases. Mechanical constraints were not taken into account. Considering the complexity of the flow features at the casing it was decided not to change the reference meridional position of the tip blade section relative to the annulus line. In this way, effects on end-walls losses strictly due to tip-clearance variation are neglected.

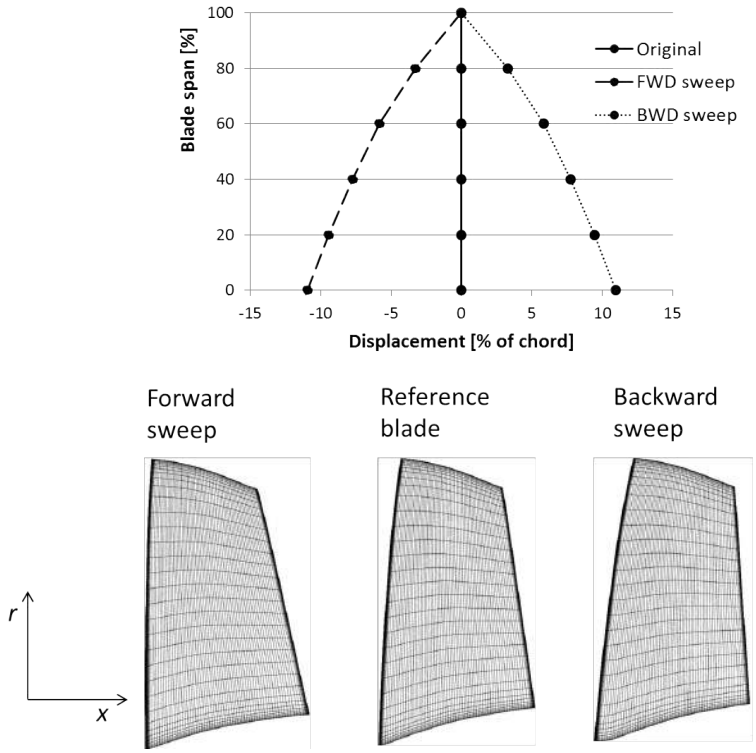

Figure 3.15: Sweep radial stacking line modifications

Figure 3.15 shows that a simple quadratic modification of the original stacking line was performed, obtained by moving five equally spaced control points along the span. A sketch of the new geometries is also illustrated. The main purpose of this set up was to explore the basic effects of blade sweep. Before proceeding with the discussion of the numerical results two additional factors need to be pointed out.

First, compared to most of studies, relatively smaller modifications of the radial stacking line have been applied here. The main reason of this choice is based on the fact that the current research also aims to explore re-design solutions for industrial multi-stage axial compressors. The applications of large geometric modifications at the end-wall might be restricted due to the presence of adjacent blade-rows and constraints on minimum axial gaps. For similar practical reasons, the hub and casing lines have not been moved and the blade has been adapted to the reference annulus according to its new meridional position. The effects on rotor performance are reported in Figure 3.16. As expected higher stall margin is obtained through forward sweep (see Table 3.2), although the near-peak efficiency pressure ratio is slightly lower than the reference one.

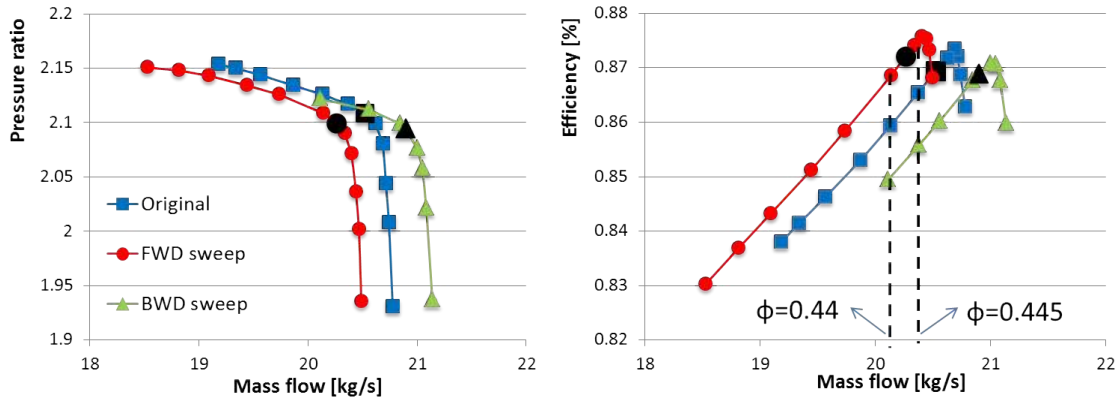

Figure 3.16: Effect of blade sweep on rotor maps

Table 3.2: Effect of blade sweep on surge margin predictions

Forward	Backward
+ 27.72%	-13.4%

From Figure 3.16 however it can be observed that using positive sweep results in larger operating mass flow range. An efficiency enhancement is predicted. On the other hand, the negative swept blade produced a decrease in efficiency, pressure ratio and surge margin. Finally, a clear variation in choking mass flow rate can be noticed. At first sight, this last effect could be attributed to the variation of the inlet annulus and thus throat area, as illustrated in Figure 3.17.

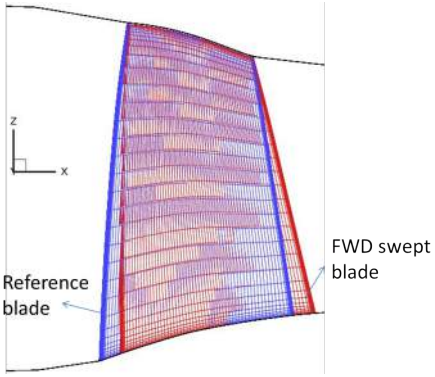

Figure 3.17: Meridional view of reference and forward swept blades

Figure 3.18 shows the radial profiles of the inlet axial velocity and inflow angle variations with respect to the reference values. Comparisons are made at two different mass flow rates (or flow coefficients, $\phi = c_{ax}/\omega r$). The results show that, at a given inlet mass flow rate, the adopted forward sweep induces an increase of axial velocity and inflow angle reduction (unloading) towards tip compared to the original inflow condition. At the hub, instead, the blade encounters the flow at lower axial velocity and higher incidence. Opposite trend can be noticed in the case of backward sweep. Such behaviour can be explained considering two different mechanisms discussed in the literature. First, forward swept tip sections may perform work on the relative incoming fluid in advance with respect to lower radii regions. Energy transfer starts at these locations and would lead to a variation of radial pressure gradient [71, 69]. As a result, the axial velocity towards the casing would increase. At the hub, on the other hand, blade sections are moved downstream with respect to the mean blade region, thus reducing the local inlet velocity. This effect would however depend on the amount of sweep applied and original variation of axial chord along the radius. Secondly, it has been observed that forward sweep would induce a vorticity component over the front part of the blade along a plane normal to the machine axis. This vortex has the opposite sense of rotation to the passage vortex, reducing the incidence and suppling energy fluid to the suction/end-wall corner [72, 73, 74]. By inspection of in Figure 3.18, another important information is related to the sensitivity to small variations of mass flows. For instance it can be observed that, as a result of a slight reduction in flow coefficient, tip regions are subjected to higher changes in inlet flow direction.

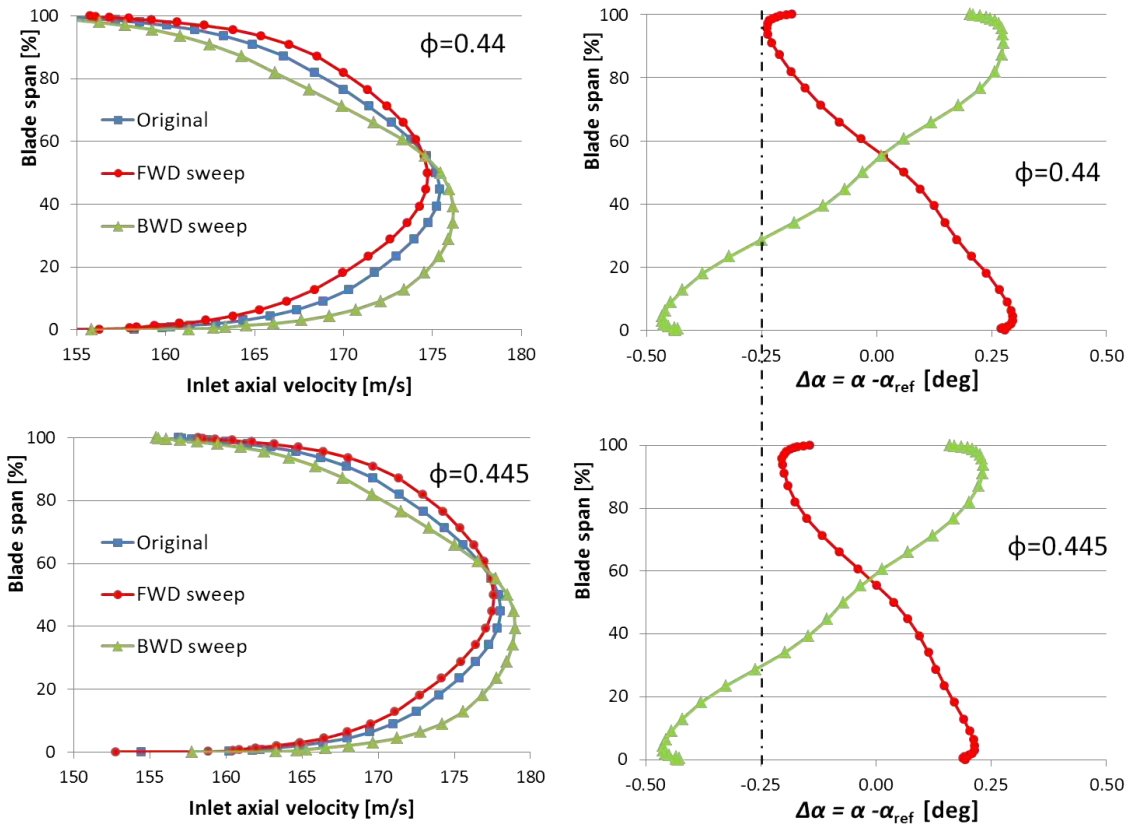

Figure 3.18: Effect of blade sweep on inflow condition at $\phi = 0.445$ and $\phi = 0.44$

This is clearly beneficial in the case of forward sweep, since higher incidence near the tip is a major cause of stall at low flow coefficients. On the other hand, the increase of inflow angle along the inner part of the blade might lead to a critical overloading, particularly for such type of rotor where the shock extends all the way down to the hub. Similar variation in inlet condition were observed in [75, 69].

Figure 3.19 shows blade pressure profile comparisons at $\phi = 0.445$ operating condition and extracted at four different radial levels along the span. Both back pressures of swept blades are lower than the reference one. The altered pressure field between the rotor blades is clearly noticeable. As expected, from the basic theory, forward sweep leads to a reduction of leading edge aerodynamic loading and thus tip clearance vortex strength. Towards the trailing edge the increase in pressure difference between suction and pressure side can be observed. The figure also indicates that the applied blade sweep has a clear influence on shock position. As the literature suggests, since the shock tends to remain normal to the end-wall it is shifted according to the tip section geometric modifications.

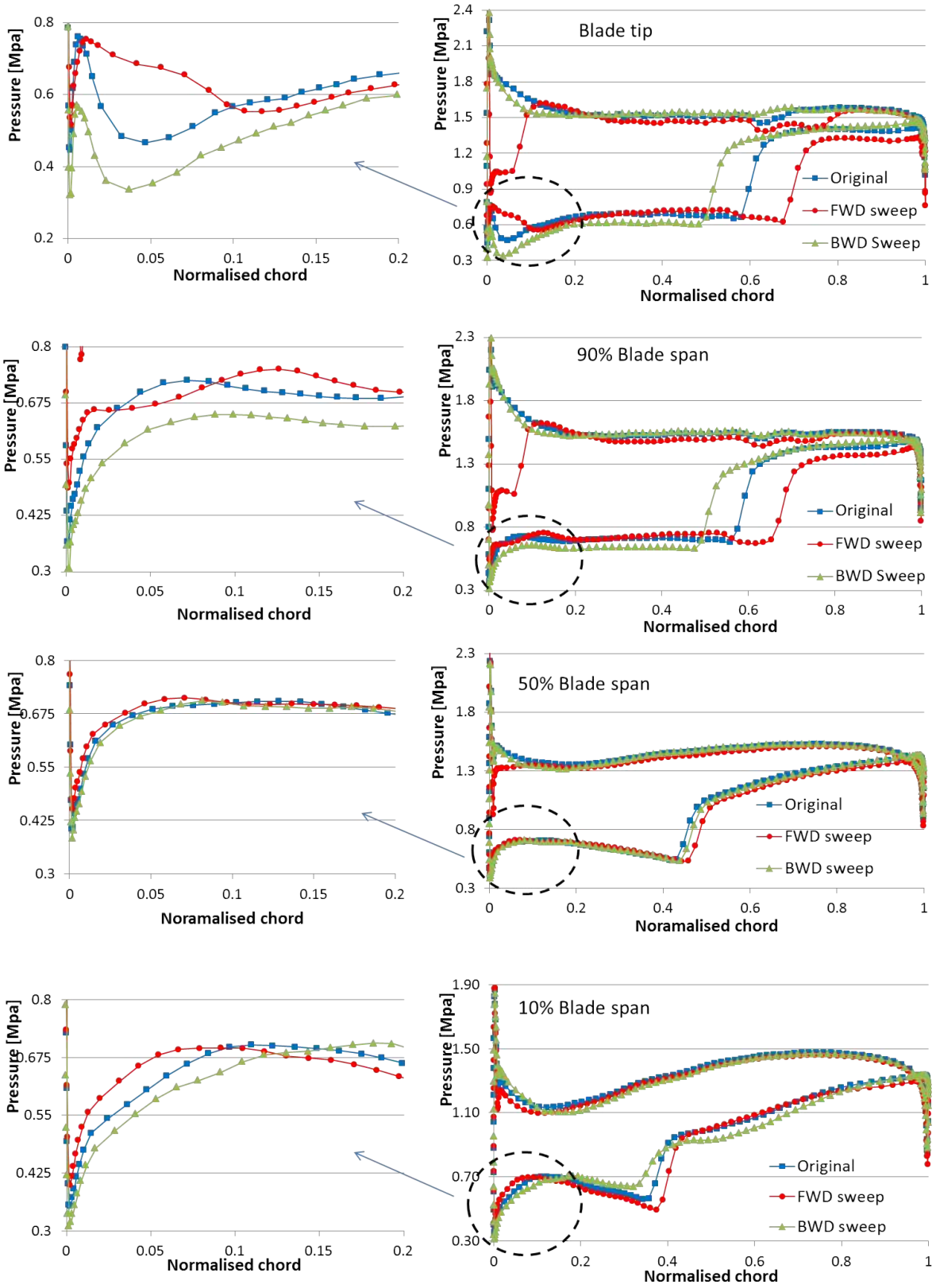

Figure 3.19: Effect of blade sweep on blade pressure profiles at $\phi = 0.445$

To further discuss the pressure profile at the tip it is necessary to illustrate the flow field contours around the leading edge (see Figure 3.20). The figure highlights that the movement of the shock has a strong impact on the inlet flow direction in the proximity of the leading edge. In particular, in the case of backward sweep the shock strengthens and moves upstream.

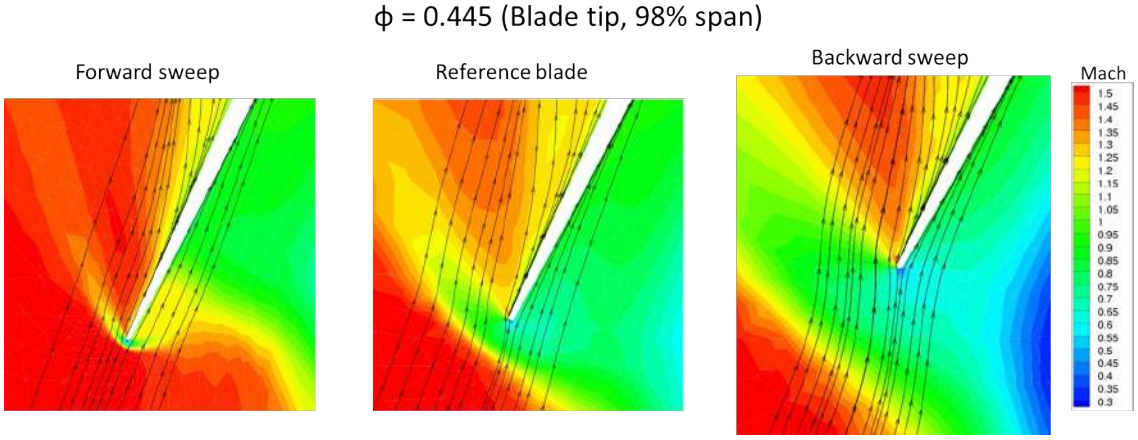

Figure 3.20: Effect of blade sweep on blade tip inlet flow field at $\phi = 0.445$

The sharp change in flow direction across the discontinuity leads to a further increase in incidence angle. In the case of forward sweep, on the other hand, the passage shock is highly curved (reduced in strength) and moved downstream inside the blade passage so that the reference incidence is reduced. It is interesting to note that the profiles shown in Figure 3.18 do not take into account these effects since they have been extracted from the solution domain at inlet section, which is about 75% of chord length upstream of the leading edge. As a result, compared to Figure 3.18, higher gradient of incidence variations would be expected. Thus, the significant decrease of incidence at the tip resulting from forward sweep reduces the maximum velocity along the suction side and moves the peak downstream. This would also contribute to move the shock backward. It can be already seen that, at such inlet mass flow rate, a further increase of back pressure would lead the backward swept configuration to an anticipated stall compared to the reference case.

Finally, two additional aspects of blade sweep should be emphasised. First, the drop in static pressure along the pressure side, due to the existence of a supersonic flow up to 0.1 % fraction of the chord, contributes to reduce the strength of the

tip leakage vortex that generates at the leading edge. Second, in addition to the argument of the blade moving across a 'frozen' pressure field determined by the radial pressure gradient, it is believed that the increase in trailing edge loading is also caused by the change in shock position.

In the following analysis, the variation in rotor performance has been investigated by comparing the three different near-peak efficiency operation, which correspond to 98.5% of the choking mass flow rates. This seems to be more appropriate rather than comparing the performance at constant flow coefficient where the backwards swept blade is operating at near-stall condition, while the corresponding forward swept configuration operation is near to peak-efficiency. Furthermore, the existence of the same back pressure for the forward sweep and reference cases made the comparison more interesting, although the backward sweep working point corresponds to a lower back pressure. Blade pressure profiles have been extracted at the same spanwise levels and reported in Figure 3.21. Comparing Figures 3.19 and 3.21 similar results can be observed. However, along the outer part of the blade, the effects previously discussed (changes in shock position and incidence angle) are reduced due to the different mass flow rates. Towards the hub, on the other hand, the effects at near-peak efficiency are magnified when compared to those illustrated in Figure 3.19. In particular, a further reduction of incidence is expected for the backward sweep case, which leads to almost the vanishing of the shock. Forward sweep, on the other hand, provokes a strengthening of the shock, which moves upstream compared to the reference case. As also reported in Figure 3.22, benefits of forward sweep along tip regions are still clearly noticeable. Overall, a reduction in flow blockage and low momentum/wake regions is observed, mainly due to the tip leakage vortex and shock strength decrease and delay in their interaction. Figure 3.23 shows the predicted streamlines along the suction side for the three different geometries, where the near-wall relative Mach number is shown in the contours. As discussed in the previous chapter the baseline geometry is characterised by a strong outward flow migration region downstream of the shock. As expected, by means of forward sweep the meridional shock at tip is skewed backward and the downstream radial flow motion is shifted downward.

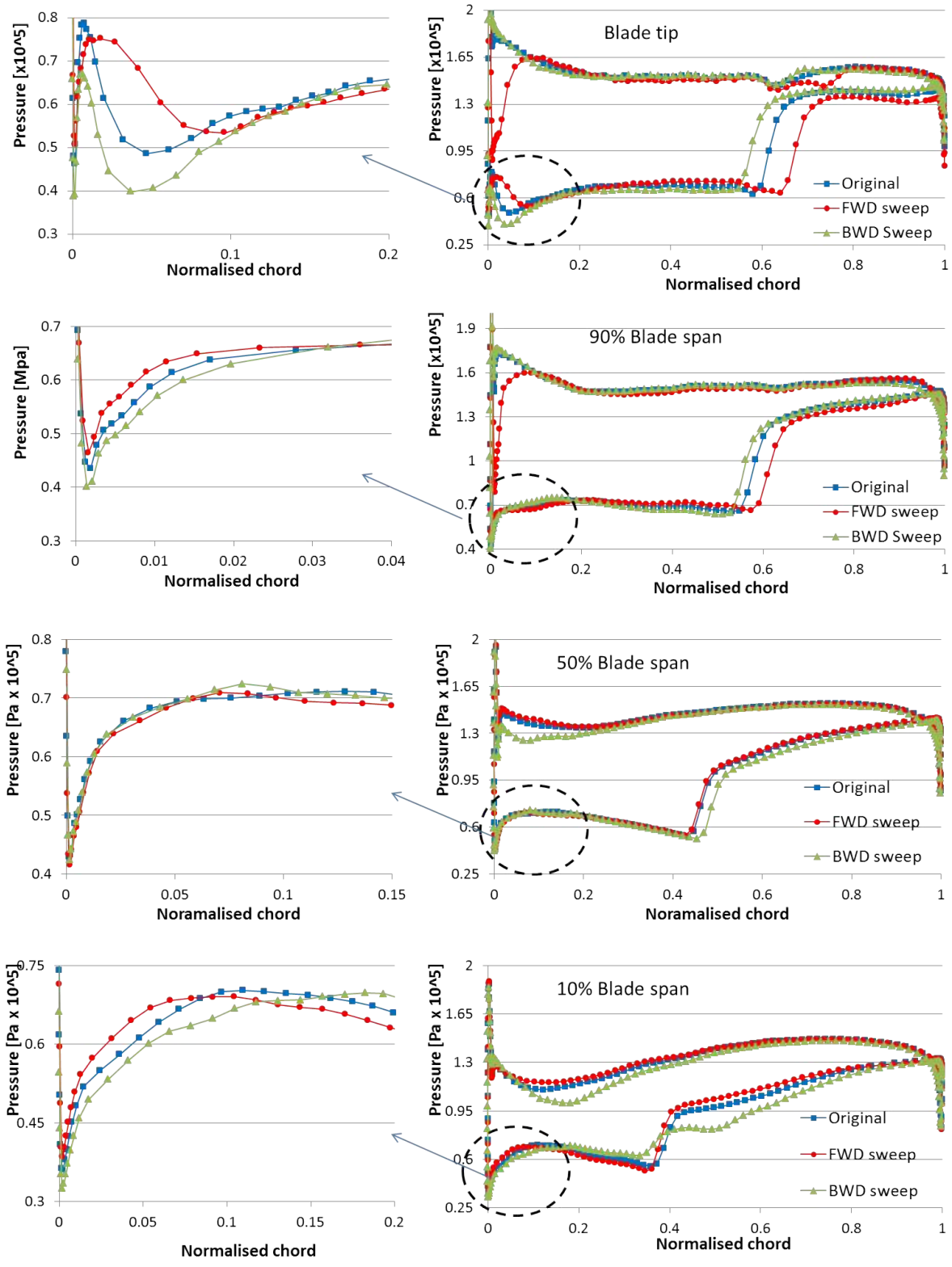

Figure 3.21: Effect of blade sweep on blade pressure profiles at near-peak efficiency operation

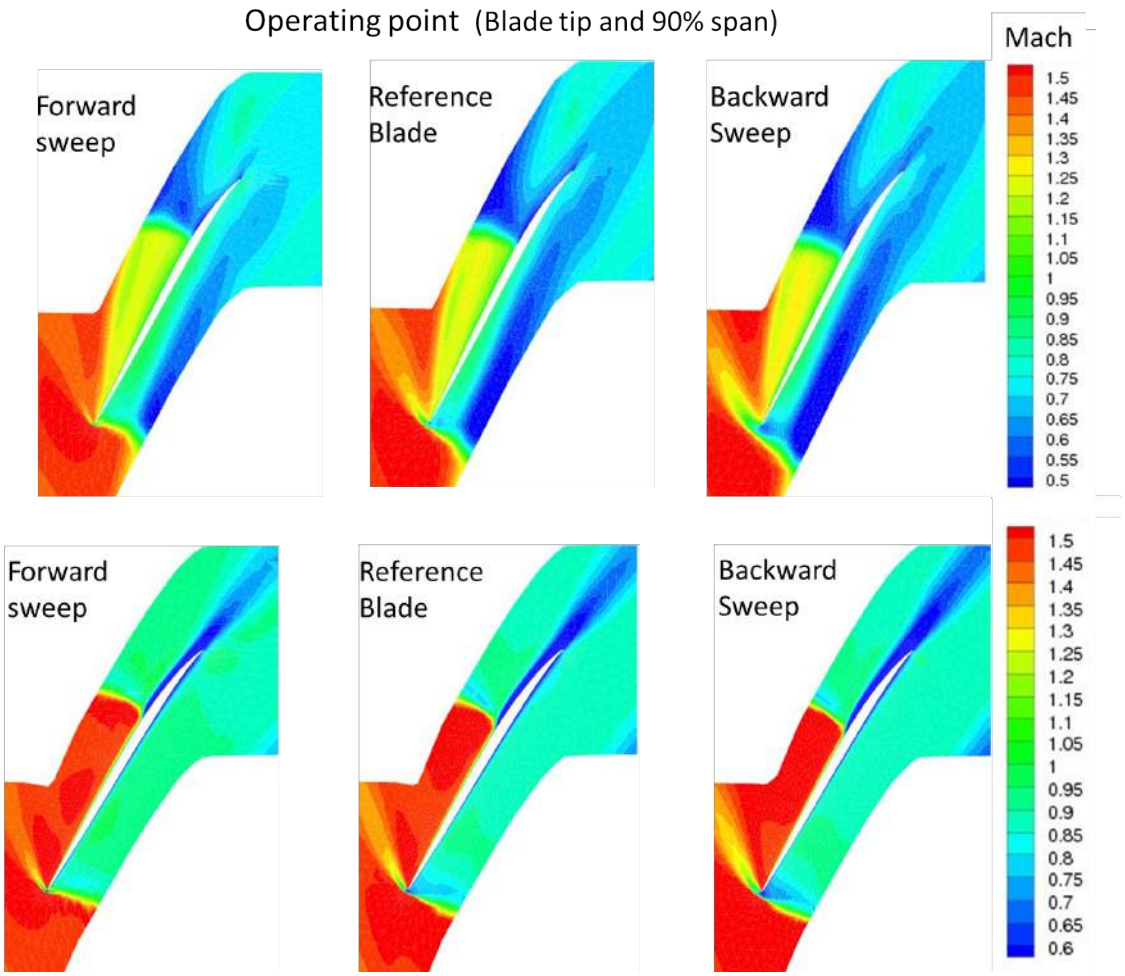

Figure 3.22: Effect of blade sweep on blade-to-blade Mach number contours at near-peak efficiency operation (tip section and 90% blade span)

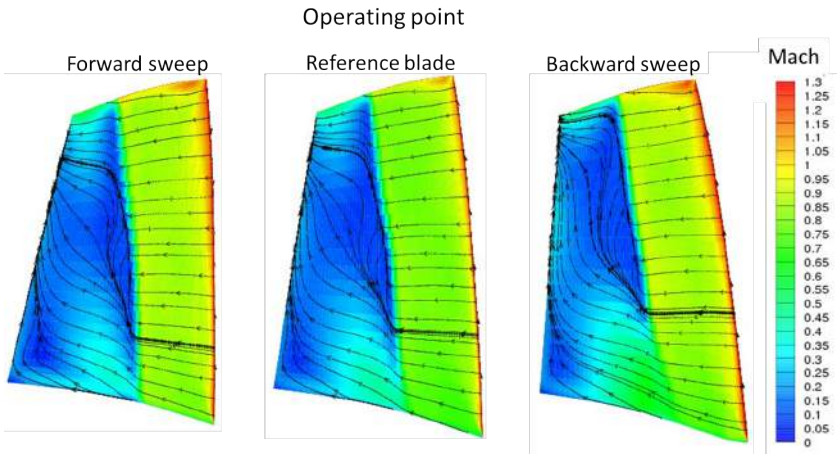

Figure 3.23: Effect of blade sweep on passage shock meridional position and radial flow at near-peak efficiency operation

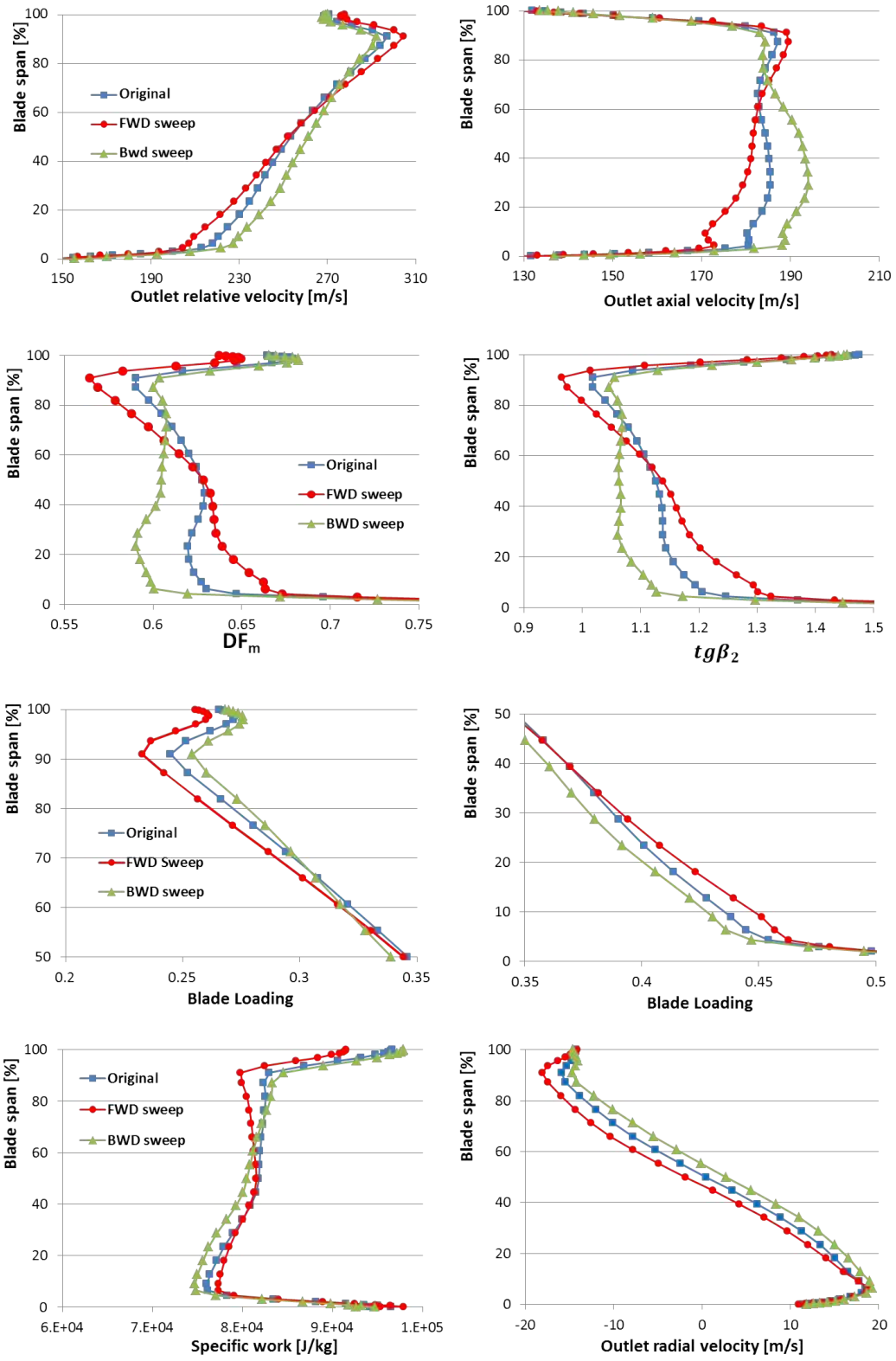

Figure 3.24: Effect of blade sweep on rotor exit flow condition at near-peak efficiency operation

It is interesting to observe the effect of blade sweep on rotor exit condition. These are summarised by the radial profiles shown in Figure 3.24. The forward sweep configuration clearly shows forward skewed radial profiles of the outlet axial and radial velocity. As indicated in the figure, this is a result of different diffusion processes across the blade passage along the span. Several mechanisms can be considered. It should be first recalled that in transonic rotors flow turning at the tip is essentially achieved through a strong decrease of the relative velocity across the shock due to the sharp density rise [76]. Thus, for forward swept blade, a reduction in shock strength would result in higher relative velocity downstream of the discontinuity. In addition, moving the shock backwards decreases the chord fraction along which the flow diffuses in the relative frame of reference. Finally, the increase of flow kinetic energy (axial velocity) in the upper part of the blade, due to the discussed decrease in flow blockage, would also lead to higher relative outlet velocity. Therefore, as a result, the flow deflection ($\tan \beta_2$) towards tip reduces. Similar variation of outlet axial velocity profiles were observed in [77, 67]. As mentioned previously, the effect of the applied forward sweep on the shock towards hub is opposite. Along the inner blade region, however, work input is also achieved by turning the flow in the absolute frame of reference. The increase of incidence probably would play a major role in the local higher diffusion. For forward sweep, the unloading of the outer blade sections reduces the local radial gradient of Euler work. This is beneficial in terms of secondary flows, which are dumped towards the casing. This is further highlighted by the higher negative radial velocity obtained towards the casing and represents another considerable contribution to the observed reduction in tip flow blockage.

Figure 3.25 illustrates the predicted rotor performance radial profiles at near-peak efficiency. As expected, by means of forward sweep, a significant increase in efficiency is obtained towards the tip due to the reduction in both shock and boundary layer (profile and end-wall) losses. Towards hub instead higher shock and, probably more important, diffusion/wake losses occur. Opposite conclusions can be deducted for the backward swept blade. The overall efficiency of both sweep configurations should be regarded as a result of different loss mechanisms at different radial levels. In terms of pressure ratio, a reduction towards tip would be expected in case of forward sweep due to the reduction of flow deflection and shock strength.

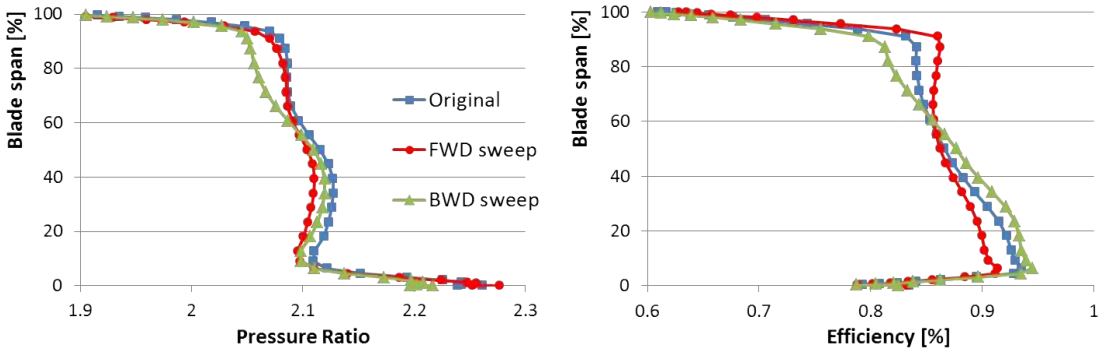

Figure 3.25: Effect of blade sweep on performance radial profiles at near-peak efficiency operation

This is however partially balanced by the local higher outlet axial velocity previously discussed. The effects revert from 70% blade span towards hub where the lower outlet axial velocity seems to have a major impact on the performance. The lower pressure rise in spite of the higher flow turning indicate an inefficient energy transfer and corrections may be required. Concerning the backward swept configuration, the higher outlet velocity compensates the lower flow turning and a slightly lower pressure rise is observed from hub to 60% of blade span[1]. The large pressure drop at tip, however, should be mainly considered as pressure losses due to the stronger shock and thus higher boundary layer thickening. Once again, this highlights the difficulty in predicting the effect of shock structure modification on pressure ratio.

Flow features near-stall have been finally analysed. Figure 3.26 shows the total pressure and Mach number outlet surface contours extracted for the baseline geometry. The results refer to a certain time step of the diverging simulation, i.e. a hypothetical point beyond the surge line. The diverging simulation has been stopped and post-processed at different time steps and all the predictions showed similar trend as the one illustrated in Figure 3.26. The purpose of such analysis is to get some information on how the rotor might be triggered to stall, within the limit of steady-state CFD analysis. As expected, both end-walls are characterised by large losses and the figure suggests that the blockage at tip would lead to flow instability.

[1]It should be here recalled that a lower back pressure exists for this case

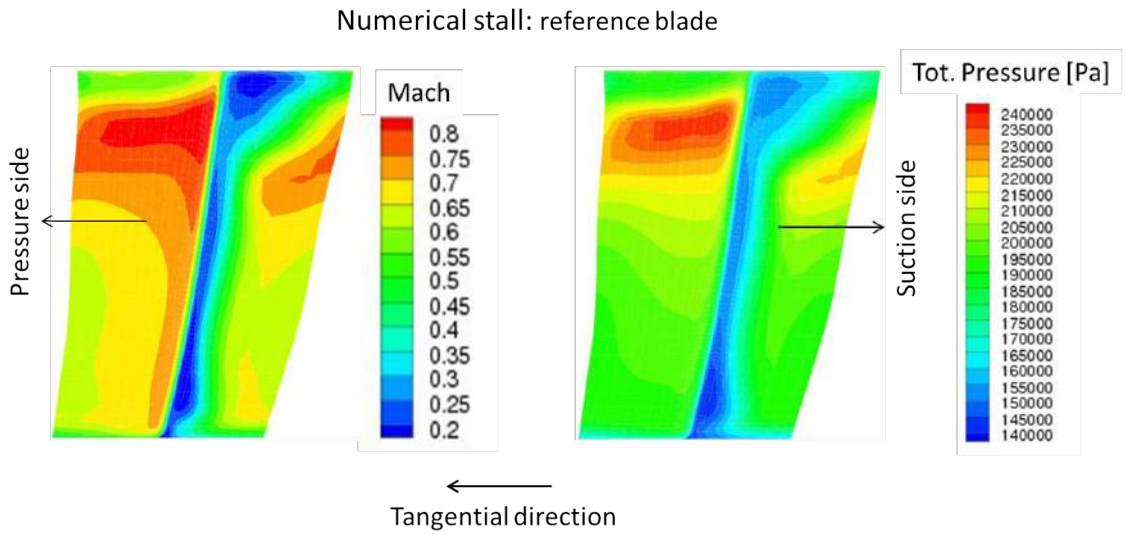

Figure 3.26: Reference blade downstream flow field at numerical stall

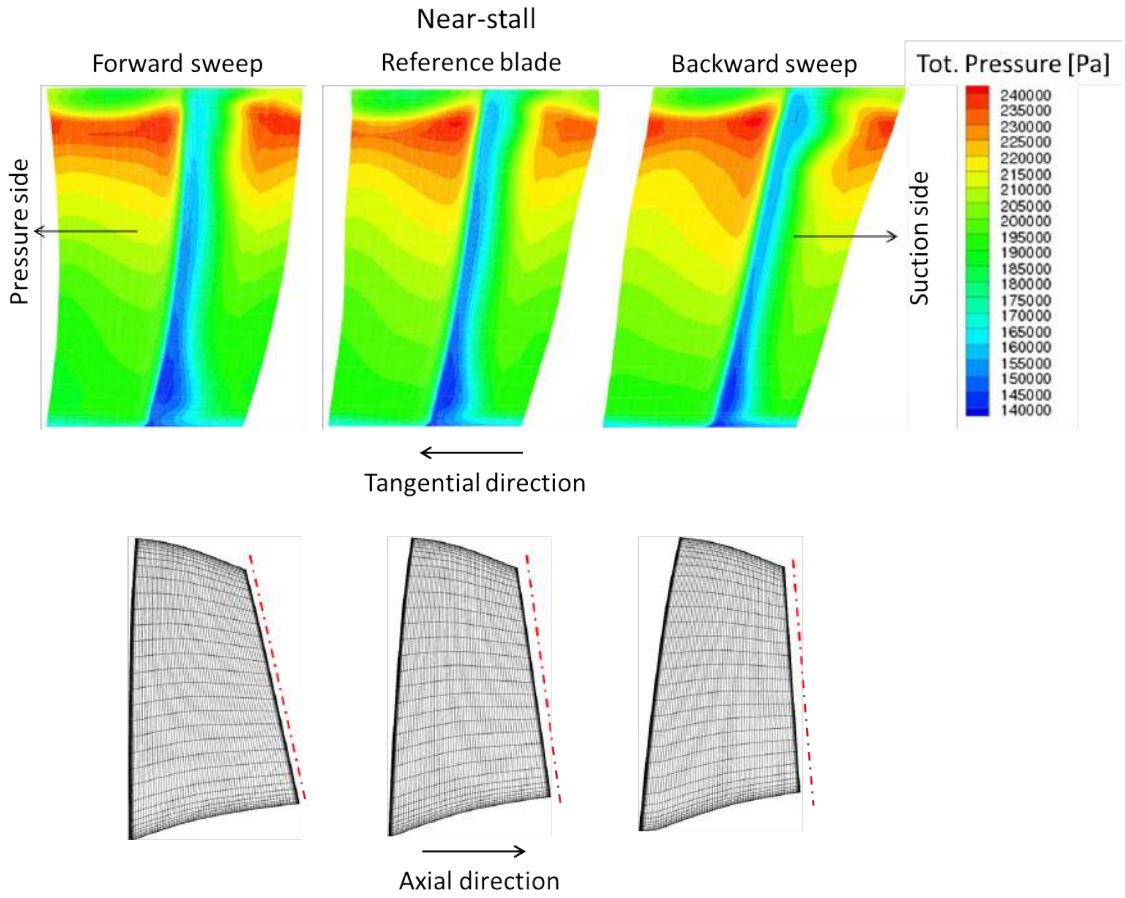

Figure 3.27: Effect of blade sweep on rotor exit flow field at near-stall operation

Figure 3.27 illustrates the stagnation pressure flow field obtained for each configuration and corresponding to last convergent simulation at low flow operation. From the contours, the change in radial wake blockage can be observed. For forward sweep, the stall margin is enhanced through the reduction in flow blockage at the blade tip. However, considering the baseline geometry flow features, the discussed increase of loading at hub might be considered a possible cause of flow instability. Clearly, the described effects are highly dependent on the quality of applied sweep and original design, on which the modifications should be based on. It would be expected, however, that an eventual optimum configuration should include a positive sweep at tip in order to reduce the phenomena related to tip leakage-shock interaction, thus improving both surge margin and local efficiency. This might be coupled with an appropriate aft swept blade curvature from hub to the mean region in order to locally correct the flow matching at the leading edge and avoid hub corner stall separation. Such type of *S-shaped* rotor has been recently investigated suggesting great potential improvements [33]. Despite the possibility of reducing end-walls losses, however, the risk in such type of transonic rotor is to overload the mid-span regions and increase the local losses and chances of large flow separation, particularly at off-design condition.

3.4.2 Lean

Unlike the sweep technique, the influence of blade lean on transonic blade performance is not widely discussed in the literature. Most of the studies on low-speed compressors observed that tilting the blade such that the angle between the suction surface and the end-wall is obtuse[2] would have beneficial effects on secondary flow losses [68, 74, 78]. In particular, the generation of induced velocities at the end-walls along the front part of the blade, and the consequent larger spanwise pressure gradient on the suction surface, would reduce the local loading and the accumulation of the low energy fluid at hub and tip. This would lead to a reduction in end-wall losses (at the expenses of mid-span regions efficiency) and moreover corner-stall delay. In transonic rotors, however, tip regions performance is dominated by the passage shock so that the effect of blade lean on shock structure may be of primary

[2]This modification has been referred in this work as negative lean

importance. Recalling that the tendency of the shock is to remain perpendicular to the wall and fixed in space, lean might also have high impact on shock position. This would mainly depend on the original orientation of the passage shock in the blade-to-blade plane [65]. Bergner et al. [79] observed that positive tangential lean can lead to a reduced strength and backward inclination of the meridional shock at the tip. Benini et al. [80] found similar results in their numerical investigations.

Recalling the sweep study, the original stacking line was changed by applying the same radial quadratic modification and keeping the original meridional position of the tip fixed (see Figure 3.28). Tangential lean was taken into account. It was observed that in the case of negative lean, numerical stall occurred once the back pressure is increased from choking condition. Nevertheless, as suggested in the literature, in case of transonic rotors interest should be on positive lean, which might provide performance improvements. This was further confirmed for the current case by adopting a smaller radial stacking line change, as reported in Figure 3.29. It was therefore decided to investigate only the positive lean. Figure 3.30 shows the predicted rotor maps where characteristic curves obtained for the forward swept blade are also reported for comparison purposes.

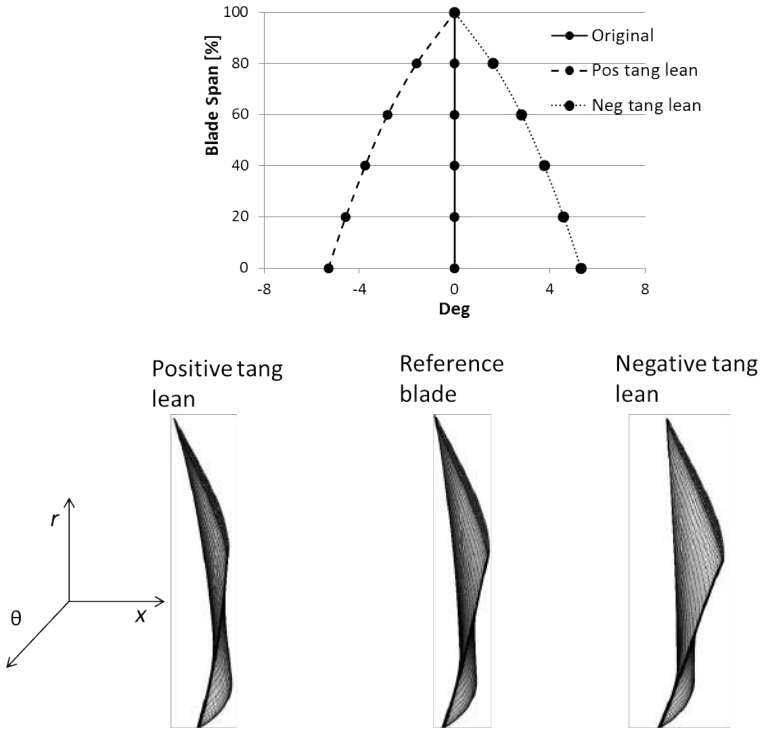

Figure 3.28: Tangential lean radial stacking line modifications

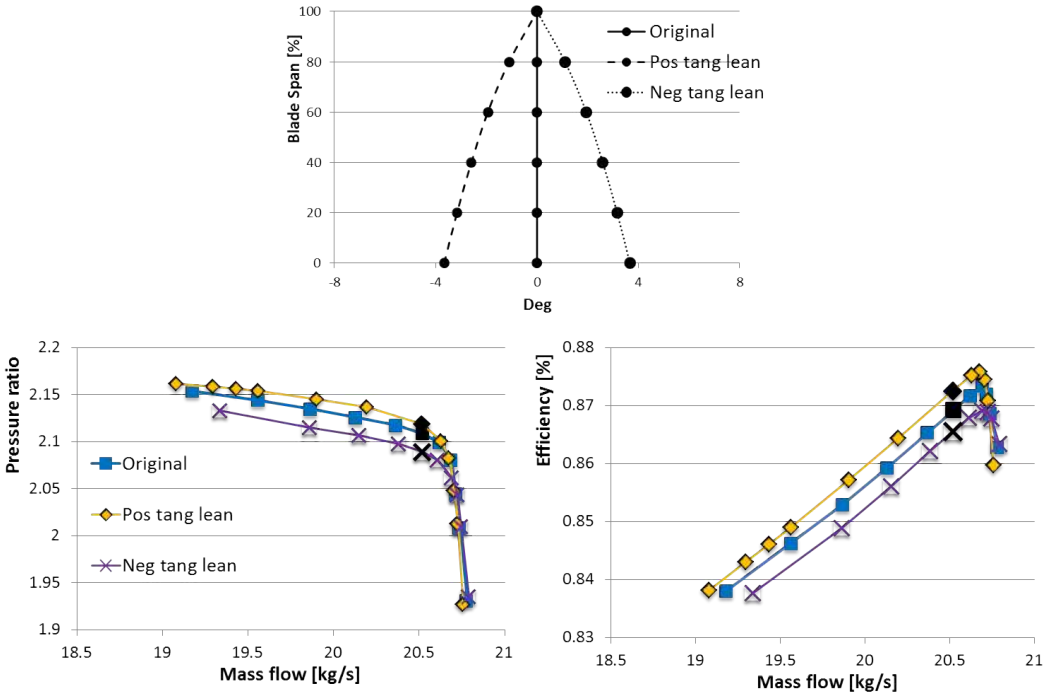

Figure 3.29: Effect of tangential lean on rotor maps. The result refer to smaller geometric modifications than those applied in the sweep study

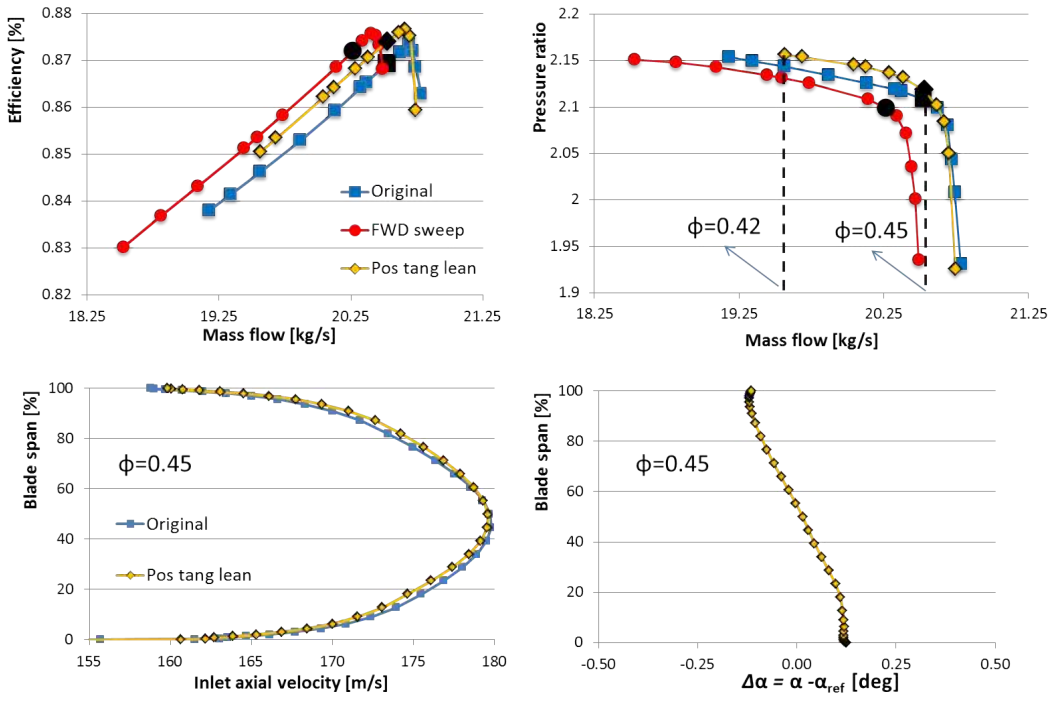

Figure 3.30: Effect of positive tangential lean on rotor maps and inflow condition at $\phi = 0.45$

The leaned blade provides a general enhancement in both pressure ratio and efficiency, while a reduction in surge margin is calculated (-25% compared to the reference value). The stability deterioration will be discussed after the flow field is analysed. No considerable variations were observed in terms of choking mass flow rate. This seems to support the theory that choking mass flow rate variations are mainly influenced by axial displacements and consequent changes in throat area. Figure 3.30 also illustrates the predicted inflow angle variation compared to the baseline geometry for the near-peak efficiency point, which for the lean case corresponds to the same reference flow coefficient ($\phi = 0.45$). Although the trend is similar to the one observed in case of forward sweep, the effect on inflow direction and axial velocity is minor.

In the following analysis the results at near-peak efficiency are compared with those obtained by means of forward sweep. It should be pointed out that the back pressure relative to the leaned blade is slightly higher than the one corresponding to the forward sweep and reference cases. Figure 3.31 shows pressure profile distributions along the span. The results indicate that positive lean has similar effects of forward sweep in terms of shock position and pressure gradient along the suction side in the upper part of the blade. This can be understood observing the reference shock swept position (see Figure 3.32) and considering a tangential movement of tip sections towards the direction of rotation across a "frozen" pressure field. As in the case of forward sweep, similar benefits are therefore expected at the tip due to lower incidence, weaker tip leakage vortex and its delayed interaction with the shock. Accordingly, the radial incidence variation should be more pronounced compared to the inflow angle distribution shown in Figure 3.30. Observing Figures 3.33 and 3.34, one can see that although the shock moves inside the blade passage, it doesn't curve as much as with forward sweep. In addition, the Mach number upstream the shock is similar to the reference case. This suggests that the shock strength has not been reduced. Nevertheless, a decrease in tip flow blockage is still achieved due to the leading edge loading reduction and downstream movement of the shock. Better results are however obtained using forward sweep.

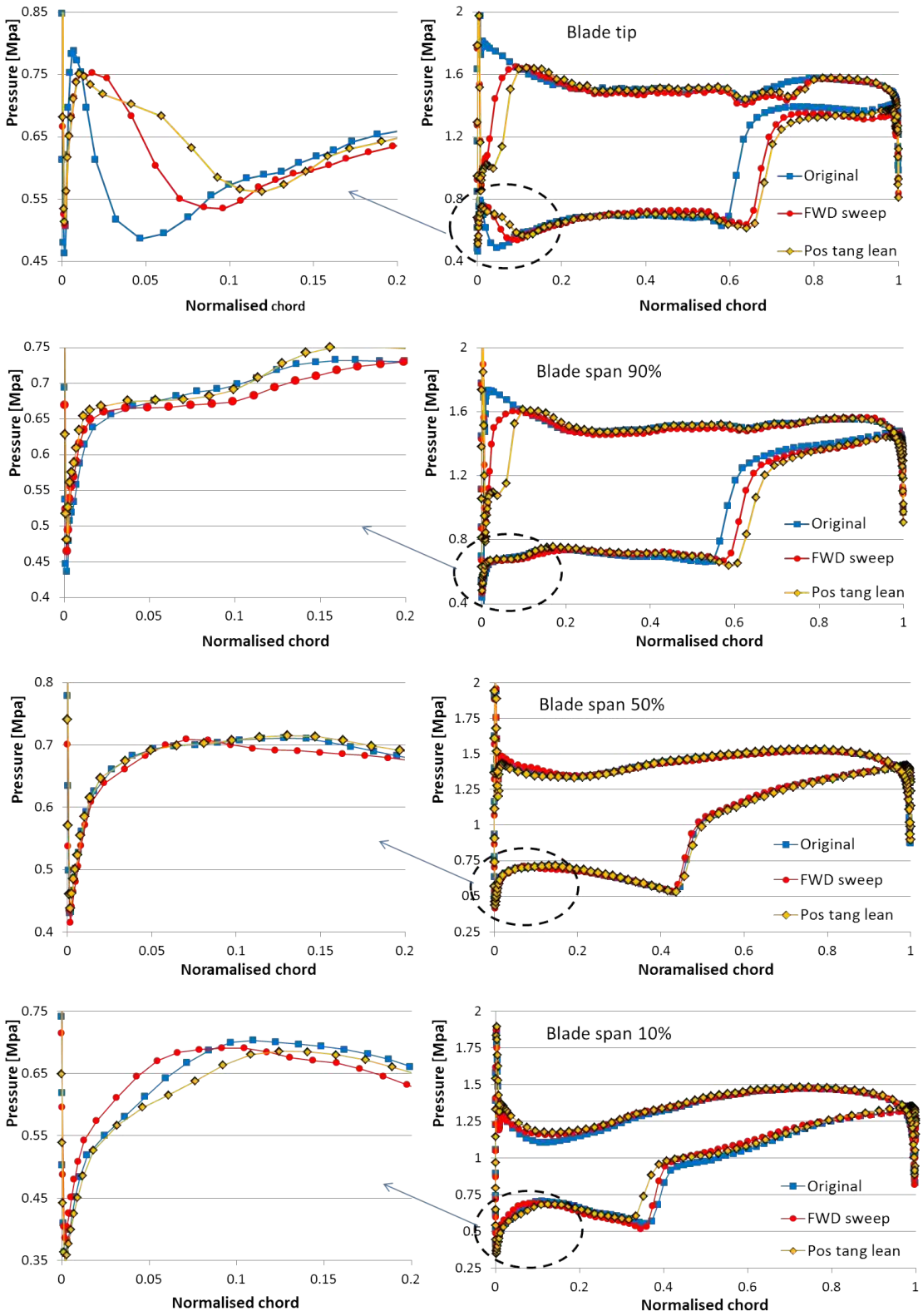

Figure 3.31: Effect of tangential lean on blade pressure profiles at near-peak efficiency operation

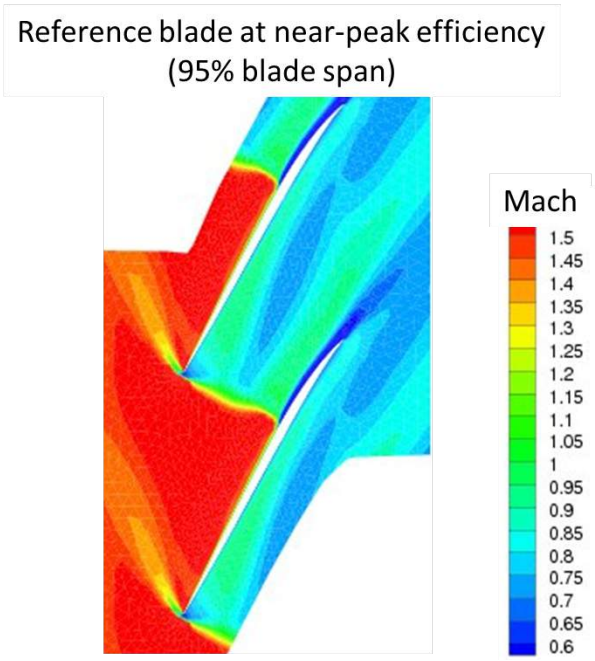

Figure 3.32: Reference blade passage shock at near-peak efficiency operation (95% blade span)

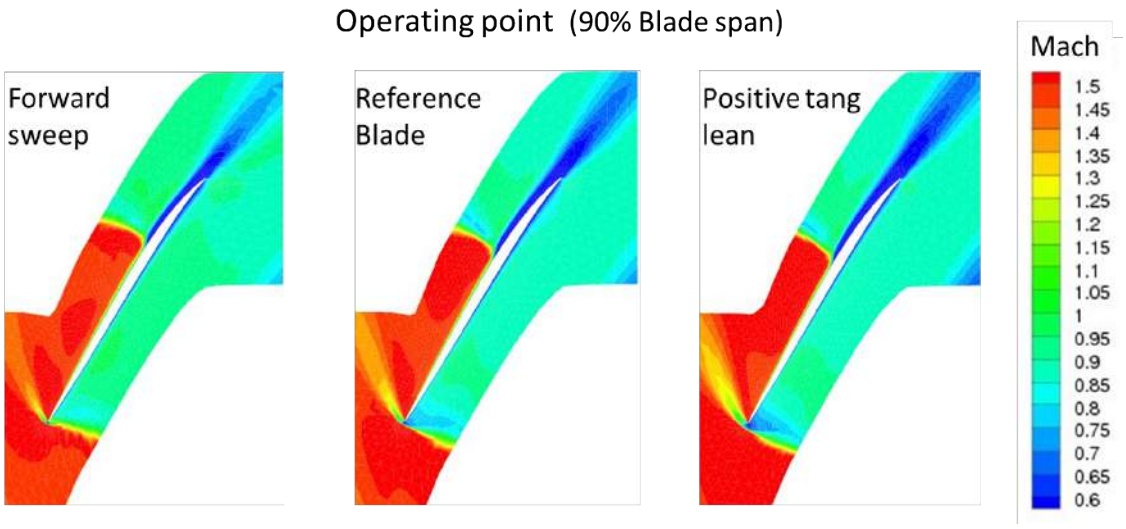

Figure 3.33: Effect of tangential lean on blade-to-blade Mach number contours at near-peak efficiency operation (90% blade span)

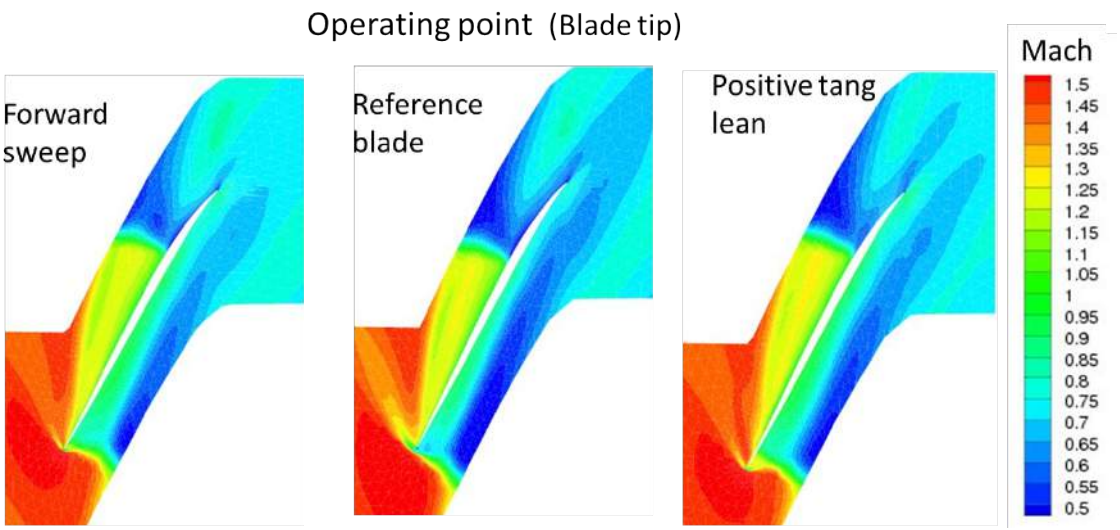

Figure 3.34: Effect of tangential lean on blade-to-blade Mach number contours at near-peak efficiency operation (tip section)

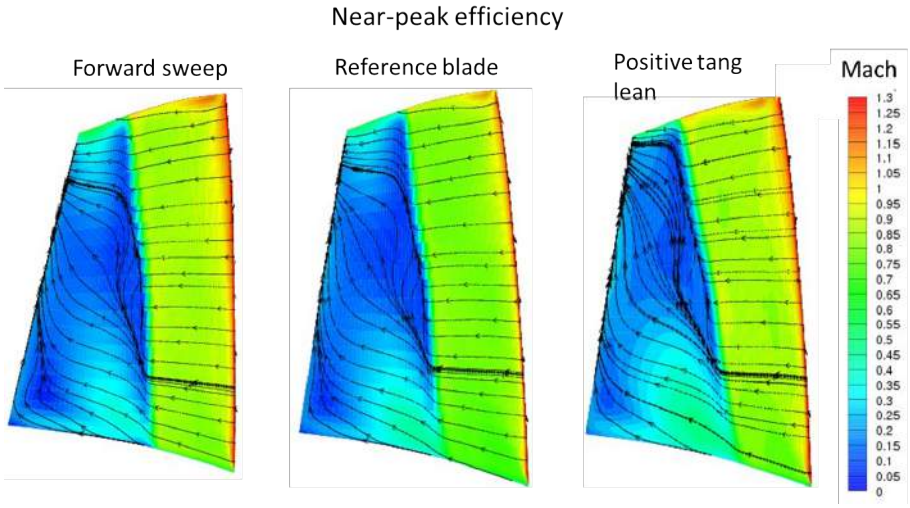

Figure 3.35: Effect of tangential lean on passage shock meridional position and radial flow at near-peak efficiency operation

Figure 3.35 shows the computed near-wall Mach number and flow streamlines on the blade suction side. For the lean case, although the shock is curved downstream in the meridional view, a larger outward flow is observed. Since the shock has not been curved in the blade-to-blade direction, such increase in radial flow should be sought, according to the literature about subsonic blade, in the lower pressure gradient along the suction side due to the applied lean. This would contrast the

benefits obtained at the tip previously discussed, playing an important role in the stalling point of the rotor.

The rotor outlet flow condition are shown in Figure 3.36. First of all it should be noted that, as a result of no significant changes in annulus and throat areas, the difference in inlet and outlet axial velocity mean values between the leaned and reference blades is relatively small. Similarly to the forward sweep case, however, the outlet axial velocity profile is bent forward at the casing, due to the local lower flow blockage. Together with the movement of the shock towards the trailing edge, this leads to higher relative velocity and thus lower flow deflection ($\tan \beta_2$). Towards hub, the leaned blade also provokes higher flow diffusion than the original case as a result of incidence increase. However, the increase in diffusion is lower than the one observed for the swept blade. This could be also related to the unchanged throat-to-outlet area ratio in the case of blade lean. Due to similar effects on blade pressure profiles along blade span, positive lean also benefits from a reduction in radial flow towards the casing at rotor exit. This seems to contrast with Figure 3.35. It might be thought however that the higher pressure difference towards the trailing edge has major influence in pushing the low momentum fluid at rotor outlet downwards. Finally, with respect to the baseline geometry, a reduction of Euler work towards the tip is as well observed. However, compared with the swept configuration, a more clear increase in specific work is predicted from 60% span to the hub suggesting that the blade is overloaded. Figure 3.37 illustrates the variation of radial performance. An improvement in efficiency is predicted towards the tip. The enhancement is however less than the one obtained with forward sweep mainly because the shock strength has not been reduced and less reduction in end-wall losses and trailing edge boundary layer accumulation is expected. In the inner part of the blade, the flow is subject to lower increase of diffusion than in case of forward sweep. Thus, the efficiency does not significantly decrease compared to the baseline profile. The pressure ratio profile at the casing could be discussed with the same argument of an existing balance between higher axial velocity and lower flow deflection proposed in the sweep section. Towards the hub, on the other hand, the outlet axial velocity is not skewed backward and higher pressure ratio is achieved.

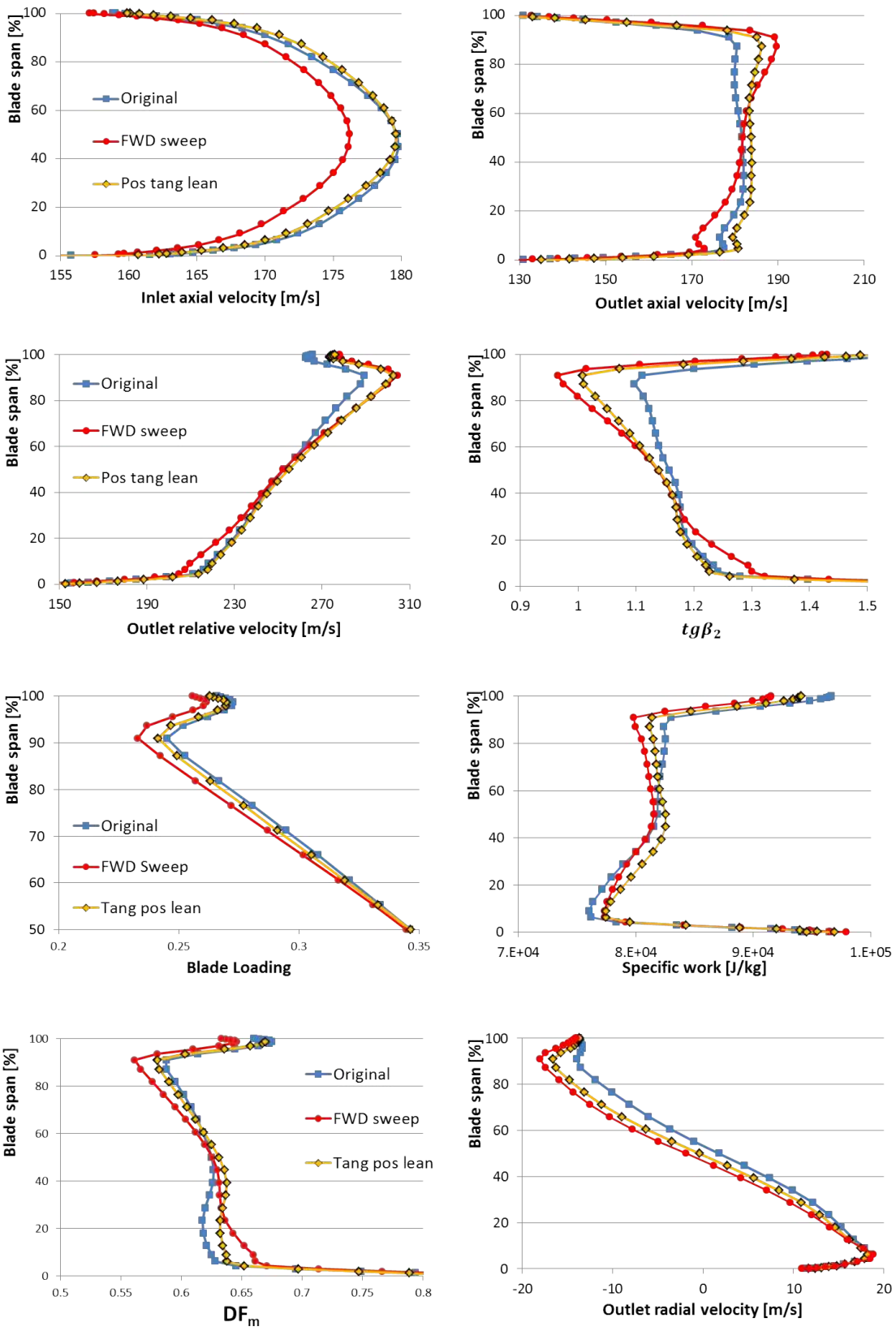

Figure 3.36: Effect of tangential lean on rotor exit flow condition at near-peak efficiency operation

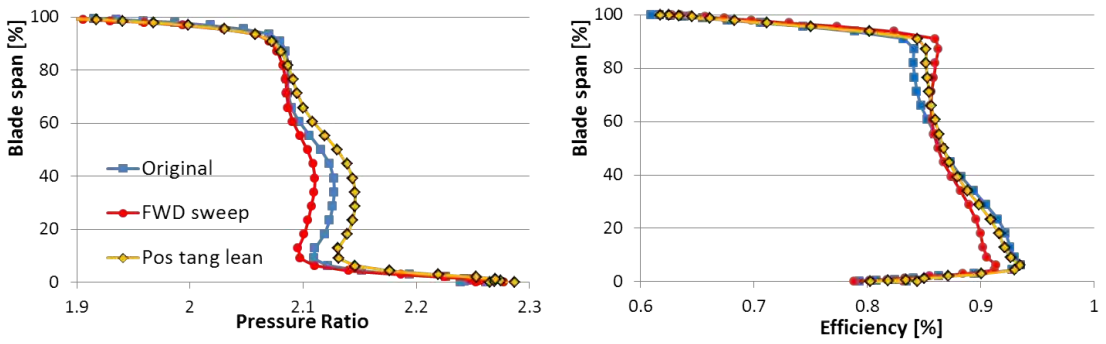

Figure 3.37: Effect of tangential lean on rotor performance radial profiles at near-peak efficiency operation

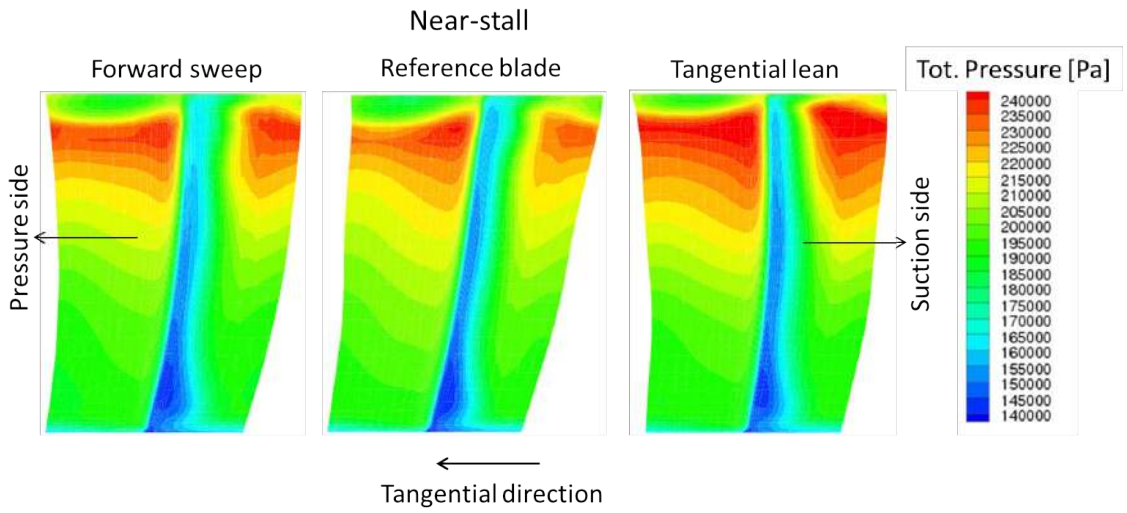

Figure 3.38: Effect of tangential lean on rotor exit flow field at near-stall operation

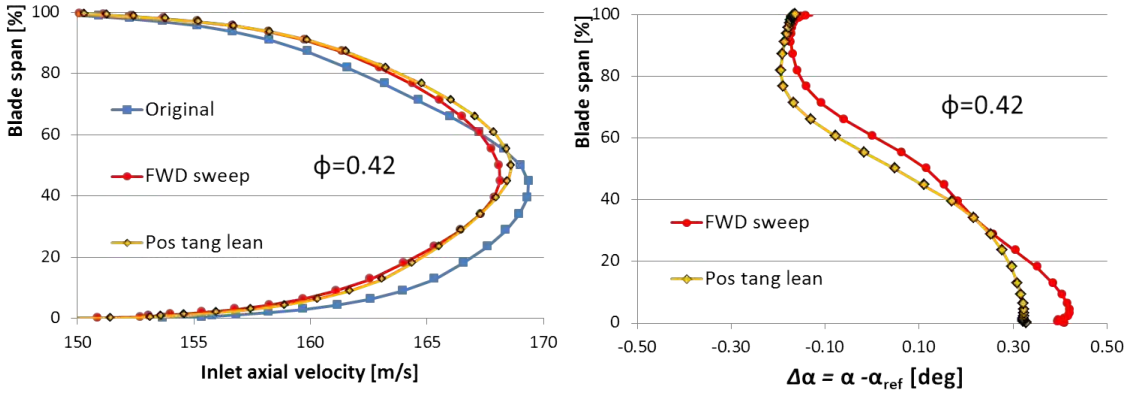

Figure 3.39: Effect of tangential lean on inlet flow condition at $\phi = 0.42$

Finally, rotor exit condition at near-stall operation are illustrated in Figure 3.38. The contours suggest that the alleviation of tip flow blockage is slightly lower than that obtained using forward sweep. Nevertheless benefits would have been expected in terms of surge margin. This is further highlighted in Figure 3.39 which shows that at a given low flow coefficient ($\phi = 0.42$), lean and sweep configurations have similar effects in terms of inflow direction changes compared to the reference case. In addition to the argument of a higher radial outward flow, an explanation of the surge margin reduction could be also found in the pressure ratio map which, from peak-efficiency to stall boundary, is shifted up compared to the original one. Observing the high sensitivity of Rotor 37 to small changes in back pressure at low mass flow rates, it might be argued that the higher operating pressure ratio at high flow condition leads the blade to an early stall. This seems to be confirmed by the fact that using a less radially stacked blade led to stall margin enhancement, as observed in Figure 3.29.

3.5 Possible configuration for hypothetical syngas combustion

Based on the performed investigations, in this section a possible efficient re-design of the baseline geometry in order to meet hypothetical syngas combustion operation is proposed. For the scope of this study, the reduction of air supply is estimated through a simple combustion model. The fuel/air ratio for a generic natural gas combustion is first calculated by applying the enthalpy balance of the process:

$$\dot{m}_a c_{p,a} T_{in} + \dot{m}_f (c_{p,f} T_{in} + \eta_b Q_f) = (\dot{m}_a + \dot{m}_f) c_{p,g} T_{out} \tag{3.16}$$

where the subscripts *in* and *out* refer to the inlet and outlet sections of the combustion chamber. The subscripts a, f and g refer to air, fuel and exhaust gas respectively. Q_f and η_b represent the fuel LHV and combustion process efficiency respectively. Rearranging Equation 3.16 gives the fuel/air ratio:

$$f = \frac{c_{p,g}T_{out} - c_{p,a}T_{in}}{c_{p,f}T_{in} + \eta_b Q_f - c_{p,g}T_{out}} \tag{3.17}$$

The assumed/calculated values for Equation 3.16 are reported in Table 3.3:

Table 3.3: Combustion enthalpy balance assumed values

	Natural Gas	Syngas
$c_{p,a}$ [KJ/K· kg]	1.005	1.005
$c_{p,f}$ [KJ/K· kg]	2.4	7.4
$c_{p,g}$ [KJ/K· kg]	1.4	1.6
Q_f [MJ/kg]	49.5	17.2
η_b [%]	0.97	0.97
T_{out} [K]	1400	1400

Typical values for natural gas combustion were assumed. Syngas properties are taken from [8], where several fuel compositions are provided. Thus, it was possible to roughly calculate the specific heat values of the fuel entering the combustion chamber ($c_{p,f}$). A slight increase of the combustion exhaust gases specific heat ($c_{p,g}$) was assumed compared to natural gas operation. Considering Rotor 37 near-peak efficiency condition ($\dot{m}_a$=20.52 kg/s , T_{in}=350 K), from Equation 3.17 the fuel/air ratio, the fuel mass flow and total mass flow rates for natural gas combustion can be calculated ($f = \dot{m}_f/\dot{m}_a = 0.034$, $\dot{m}_f$=0.7 kg/s, $\dot{m}_{tot}$=21.22 kg/s). Assuming a constant turbine inlet mass flow rate, the fuel and air mass flows for the syngas combustion could be finally estimated ($\dot{m}_f$=2.2 kg/s , $\dot{m}_a$=19.04 kg/s) leading to a reduction of compressor air supply of about 7%. Such model represents a simplification since, in reality, what determines the required reduction in compressor air delivery is the inlet turbine volumetric flow. This should be determined also considering other factors, such as the variation in molecular mass of the combustion products and amount of fuel diluent in order to keep the reference TIT. However the accurate prediction of the different combustion processes is beyond the scope of this section.

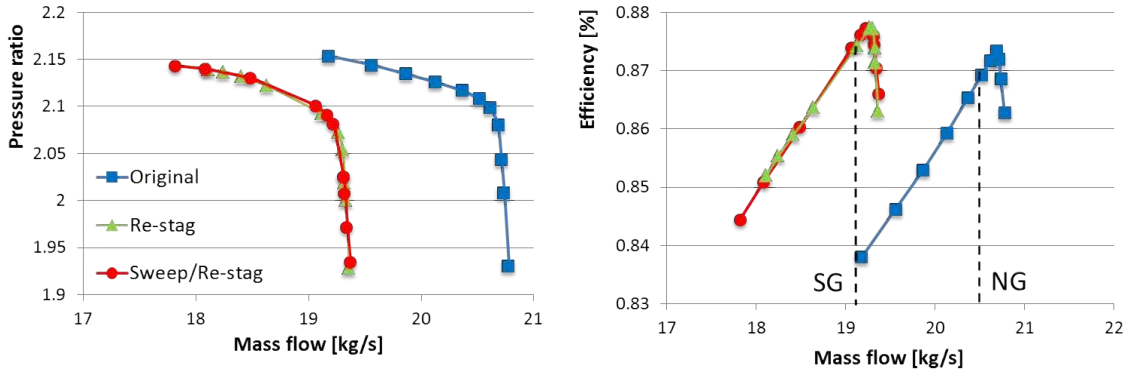

Figure 3.40: Possible configuration for syngas combustion operation

Recalling Figure 3.5, by positively re-staggering the reference blade it would possible to operate with high efficiency at lower mass flow rate. However, as discussed in the related section, stagger modifications cause a reduction of surge margin. An improved design, for instance, could be obtained through an appropriate combination of sweep (or lean) together with positive stagger. In particular, considering the general purpose of the current research, the possibility of improving the surge margin and efficiency while reducing the choking mass flow rate makes the forward sweep a very interesting technique. In this study, the forward swept blade previously presented has been re-staggered by 2.3° in order to provide the required reduction in air supply. The overall performance have been compared with those of a 2.8° re-staggered blade, necessary to shift the original rotor maps towards the lower mass flow range only by closing the blade. The results, shown in Figure 3.40, confirm the expected stability enhancement. Finally, Table 3.4 reports the performance variations obtained with the re-designed geometry compared to the baseline rotor.

Table 3.4: Performance variation with respect to the baseline case

	Re-stag	Sweep/Re-stag
Efficiency	+ 0.7%	+0.75%
Surge margin	-9.5%	+8.5%
Pressure ratio	-0.7%	-0.7%

3.6 Summary

The effect of blade re-staggering has been first explored, with the purpose of providing suitable compressor re-design solutions for syngas combustion operation. The shift of the working line towards lower mass flow range by means positive re-stagger is accomplished with a slight increase of efficiency and reduction of surge margin.

As indicated by most of the previous investigations, stability (and tip efficiency) enhancements are achievable through the application of forward sweep. In particular, the study supports that the main advantage results from the reduction of flow blockage due to the weaker tip leakage vortex-shock interaction and lower low momentum flow accumulation at rotor tip. In addition, this work highlighted that a considerable contribution to the performance enhancement is due to the reduction in incidence at the leading edge consequent to downstream movement of the shock. Similar performance improvements towards the casing are possible through the use of positive tangential lean. In this work, however, the surge margin was reduced. This was believed to be related to the higher pressure ratio and overloading obtained with blade lean, especially when considering the throttling characteristic of Rotor37. Such hypothesis was further sustained by the fact that applying a lower stacking line modification led instead to higher mass flow operating range. Overall, however, the results showed that greater benefits at the tip are achievable using positive sweep. Both re-stacked configuration caused an undesired increase of incidence towards hub where the rotor is highly loaded. Better configurations would therefore include combination of forward and backward sweep as well as positive and negative tangential lean. Optimisation procedures may be necessary in order to avoid undesired overloading in the mean region of the blade.

Finally the possibility of shifting the working line towards lower flow rates (without affecting the original machine performance) by means combination of sweep and stagger should be considered as an interesting solution in the context of this research. For instance, this could be included among the possible re-design options for the transonic front stages of an industrial gas turbine compressor, depending on the original design and behaviour at off-design condition.

Chapter 4

Multi-stage compressor modifications for syngas operation

4.1 Introduction

In this chapter the investigation of possible compressor re-design solutions to cope with hypothetical syngas operation is extended to a three stages axial compressor with an IGV. Two different analyses are performed with the objective of identifying trends rather than producing optimum design. In the first study the shifting of the working line towards lower flow rates is obtained through the re-staggering of the four stator vanes. The purpose is to gain some insight on the variation of design flow features when using VSVs. The possibility of considering such vanes as variable would allow for a fast adaptation of the compressor to the two different types of combustion. The second study includes the application of blade modifications discussed in the previous chapter in the subsonic compressor stage. In particular the effect of blade sweep on a highly loaded stator flow field and overall compressor performance is considered. Only the new nominal (full-load) operating condition for syngas combustion is taken into account. As discussed in Chapter 1, however, part-load condition are of high relevance in terms of combined cycle performance. These will be considered for the H2-IGCC compressor in Chapter 6.

4.2 Test case and model validation

In this work the IDAC compressor is used as test case. The high speed three stage axial compressor with an IGV was built and tested at the Institute of Jet Propulsion and Turbomachinery at RWTH Aachen University [81]. Figure 4.1 shows the compressor meridional view and design details are reported in Table 4.1. One of the purposes of the test rig design was to study the effect of high loading on compressor stability. This was done by providing very high flow diffusion in the last stator, where a large flow separated region exists even at design condition (see Figure 4.1). As discussed in [81, 82] the compressor is trigged to stall at design speed by the last stator flow separation.

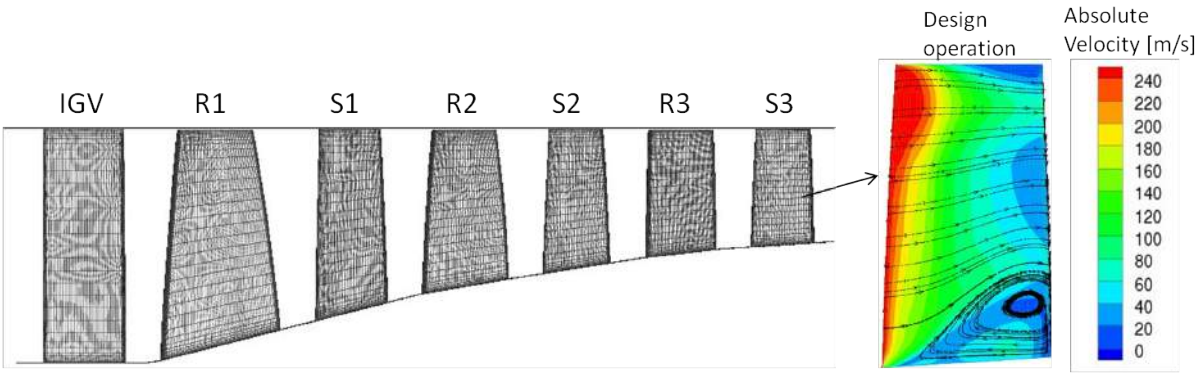

Figure 4.1: IDAC mesh meridional view and stator 3 (suction side) absolute velocity contour and streamlines

Due to this specific design, it may be argued that the IDAC compressor is not an ideal test vehicle for the current study, since it does not represent a typical industrial gas turbine compressor. The main reason for such choice is related to the difficulty of getting geometric data and test results for a more representative compressor. Nevertheless, the high loading and consequent flow separation at last stator hub may be seen as a typical near-stall condition that would lead an industrial compressor stage to stall. The study of the application of radial stacking line modifications in order to locally reduce the separation region and improve the stability margin can be therefore considered of relevance. In addition, the small number of stages made it ideal for a parametric exploratory study.

Table 4.1: IDAC compressor design parameters

Rotational speed [rpm]	17000
Mass flow rate [kg/s]	13.40
Power [kW]	920
Total pressure ratio (1^{st}, 2^{nd}, 3^{rd} stage)	2.03 (1.30, 1.28, 1.22)
Total temperature rise [K]	68
Max relative inlet Mach number	0.89
Inlet outer diameter [mm]	387
Inlet inner diameter [mm]	213.60
Rotor tip clearances [mm]	0.35

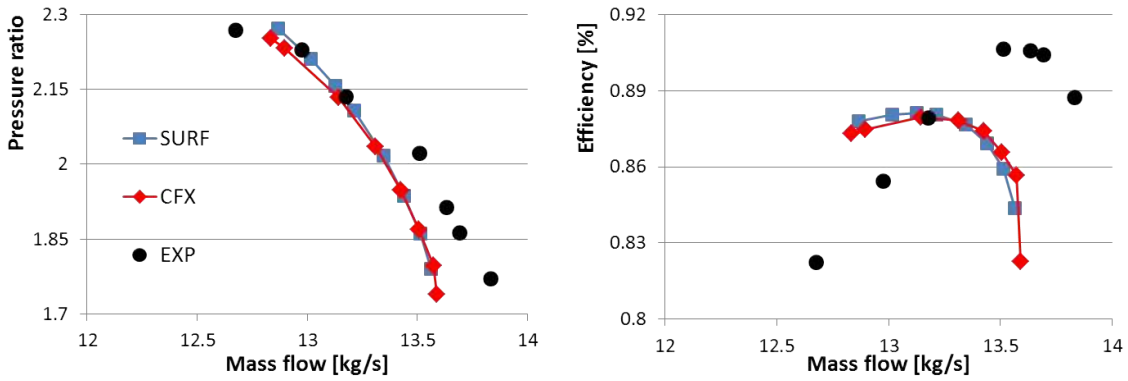

Figure 4.2: Model validation. IDAC compressor maps

First of all, numerical model validation with the available experimental data was attempted. The procedure for CFD calculation is the same as the one described in Chapter 2. Figure 4.2 shows a comparison in terms of compressor characteristics. While a fairly good agreement was found in terms of pressure rise, the trend of the measured efficiency is not well reproduced particularly for the low-speed flow range. Furthermore the choking mass flow rate predicted from computations is smaller than the measured one by about 2%. Discussions with RWTH who conducted the experiments revealed that the tests were done with bifurcated inlet duct with a 90° bend upstream of the compressor with no measures to reduce the effect of flow inlet

distortion. In addition measurements were taken in the upper sector of the annulus because the main purpose for the experiments was to study the unsteady flow behavior. Measurements of the flow variation around the annulus were not performed. In this study, numerical simulations were carried out by imposing a uniform total pressure profile and assuming an axial flow at the compressor inlet and applying mixing planes at the inter-blade row boundaries. The parametric studies here needed to be done using steady flow analysis for computational efficiency. A reassurance of the current calculations was given through predictions using the commercial code CFX(C) (shown in Figure 4.2) which showed similar results to those produced by SURF when applying the same boundary conditions. Nevertheless, in addition to the results discussed in Chapter 2, the code has been successfully validated with different compressor flow cases in the past [37, 38].

The IDAC design mass flow rate is 13.40 kg/s (corresponding to about 97% of the choking mass flow rate), at which the compressor operates at peak efficiency condition. The peak efficiency predicted using CFD simulations is also obtained for a mass flow rate equal to 97% of the corresponding choking value. It was therefore decided to consider such operating point as the nominal one for CFD flow analyses. The predicted nominal pressure ratio, however, is higher than the measured value.

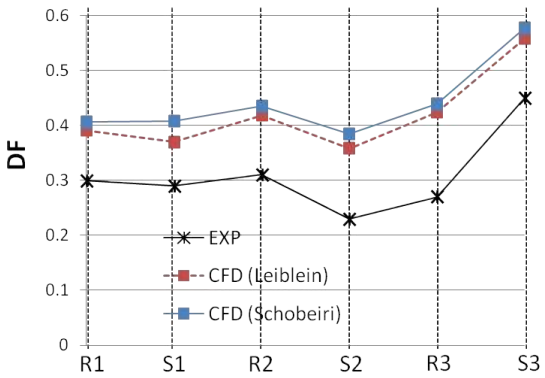

Figure 4.3: Model validation. Diffusion factor variation across the compressor at design condition

Figure 4.3 shows a comparison between numerical results and experimental data in terms of flow diffusion variation across the compressor at design condition. Similarly to Rotor 37 study, the diffusion was also calculated using the expression proposed by Schobeiri showing again that accounting for compressibility effects results

in a slightly higher DF. In any case, it is interesting to observe that the trend of the diffusion variation through the compressor obtained from measurements is fairly well reproduced by the calculations. In particular it can be seen that the first two rotors exhibit higher loading with respect to the downstream stators while, as expected, stator 3 shows the highest DF. However the numerical predictions are higher than the measurements; this could be related to the difference in experimental and numerical setups mentioned earlier.

4.3 Re-staggered machine for hypothetical syngas combustion

In this section the possibility of re-staggering the compressor guide vanes in order to meet hypothetical syngas combustion operation is discussed. The required reduction of air from the compressor has been estimated using the same procedure and assumptions described in Chapter 3. In this case, considering the nominal working point ($\dot{m}_a$=13.125 kg/s , T_{in}=360 K) the new air supply was predicted to be $\dot{m}_a$=11.93 kg/s, which means a reduction of about 9% of the original value.

A first modification to shift the operating point towards the estimated lower value was made by only closing the IGV. The blade was staggered around the centre of curvature of the leading edge. The required decrease of compressor air supply was achieved by closing the IGV by about 14°, which resulted doubling of the nominal stagger angle at mid-span. As expected, considerable reduction in pressure ratio (-7.75%), efficiency (-1.20%) and surge margin (-20.5%) was obtained at the new operating point (see Figure 4.4). It was observed that in terms of pressure ratio and efficiency, the major drop occurred in stage 1. The decrease in pressure ratio is mostly related to the high mismatch at rotor 1 inlet due to the IGV blade-row closure. In order to explain this further, Figure 4.5 shows the change in the velocity triangles at mid-span. It can be noticed that, despite the reduction of axial velocity (which would push the rotor inflow towards higher incidence), the increase of both absolute flow angle and velocity at IGV outlet leads to a reduction of rotor 1 relative inflow angle. This causes a decrease of blade loading and flow diffusion along the suction surface.

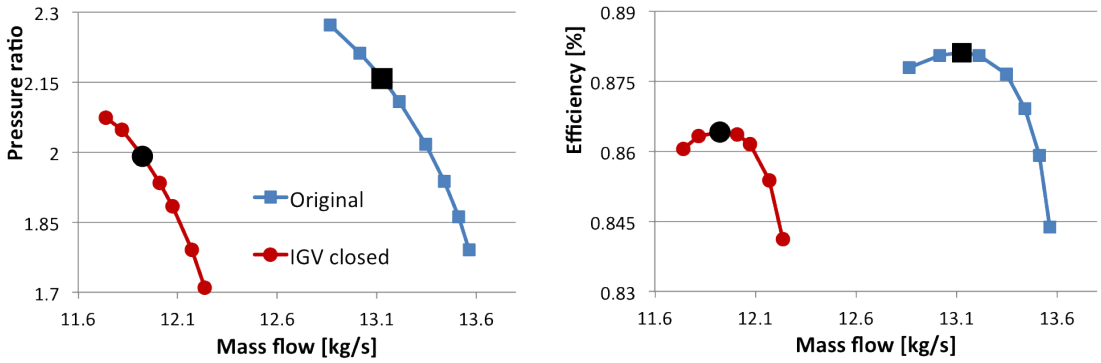

Figure 4.4: Drop in overall compressor performance when closing the IGV

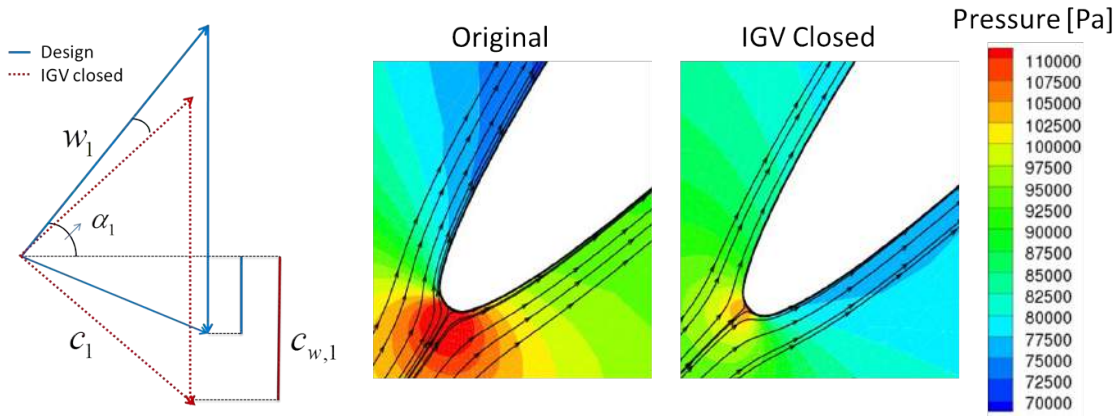

Figure 4.5: Rotor incidence angle variation due to IGV closure. Contours refer to mid-span section

Figure 4.6 shows however that such an effect rises moving from blade tip towards hub. In particular, in the lower part of the blade the pressure distributions on the front of the suction and pressure surfaces swap and the diffusion on the pressure surface is increased (negative incidence). This behavior can be explained by observing Figure 4.7 which shows the radial variation of the axial and absolute velocity. The axial velocity profile for the reference machine is typical after the IGVs [76]. The figure shows a more significant axial velocity reduction in the outer part of the blade when closing the IGV while, on the other hand, higher increase of absolute velocity is predicted towards the hub. The strong unloading of the blade clearly results in a less efficient flow compression through the first rotor and higher losses occur towards the hub, due to the incidence variation. The bad axial matching along the inner part of the blade is also reflected to the downstream stator where further losses arise. Finally, an efficiency drop occurs across the IGV, mainly due to the strong

flow acceleration around the leading edge and narrowing of the blade passage [83]. These results are illustrated in Figures 4.8 and 4.9, which highlight that major losses arise from the IGV and stator 1.

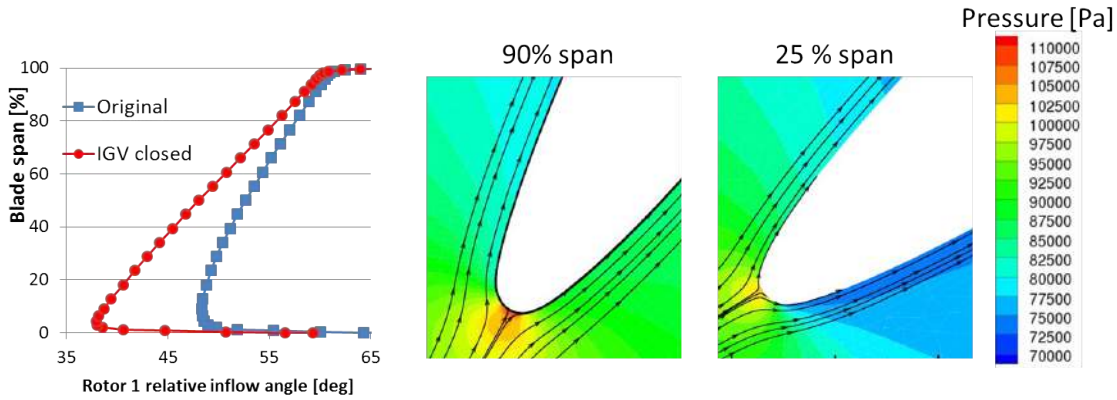

Figure 4.6: Spanwise variation in relative inflow angle due to IGV closure

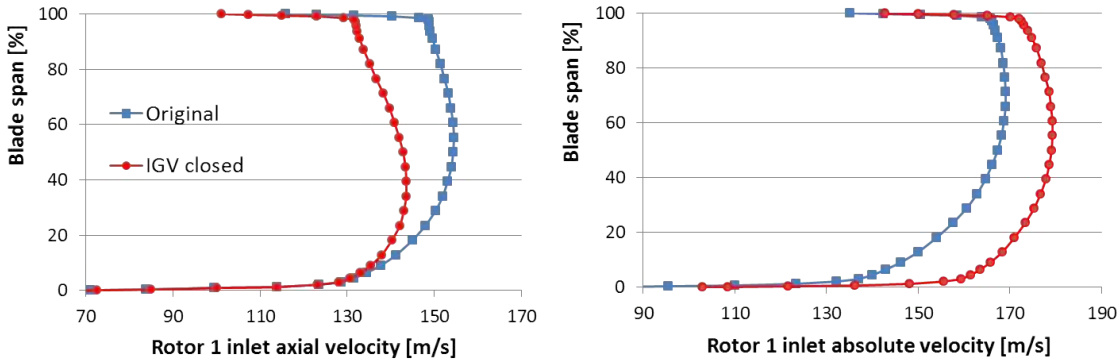

Figure 4.7: Axial and absolute velocity radial variations at rotor 1 inlet due to IGV closure

The change in stage loading was also investigated in stages 2 and 3. A general small increase in DF was observed, as a result of the new axial flow matching which led to a slight increase in incidence at each blade-row. Considering the moderate loading, however, no significant changes in pressure losses were predicted up to rotor 3. For the last stator, the increase in flow diffusion resulted instead in an augmentation of losses at hub due to an enlargement of the separated flow region, which can be seen in Figure 4.10. This is a consequence of the local high flow diffusion which characterises the compressor at design condition.

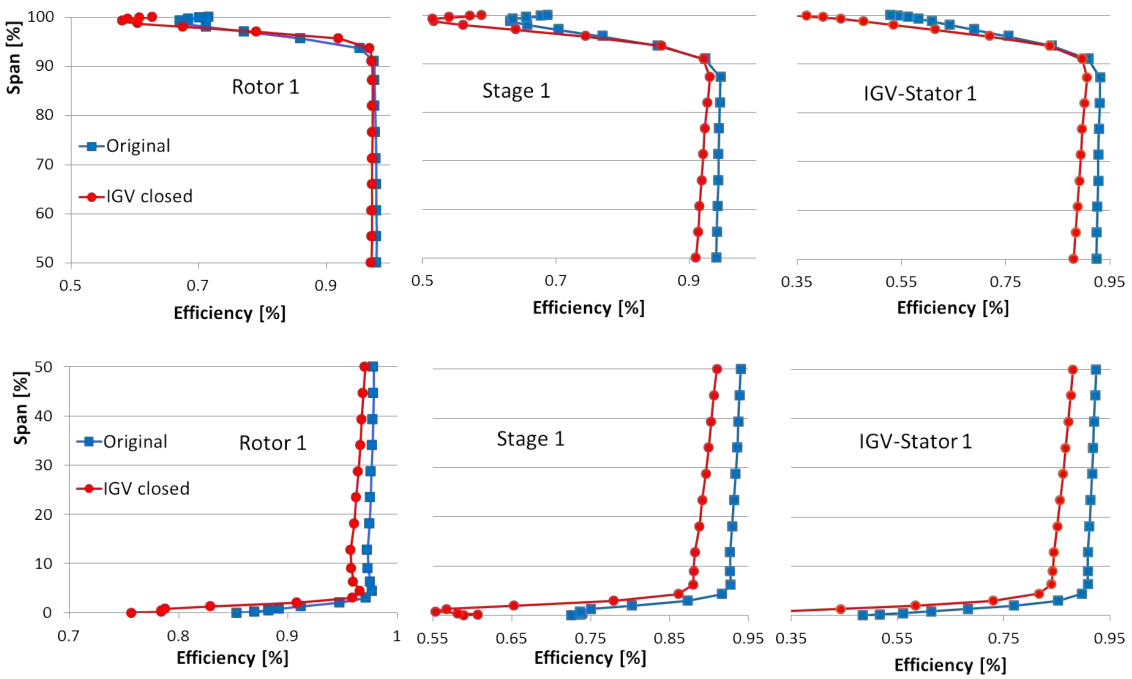

Figure 4.8: Radial efficiency profile variations across the first three blade-rows

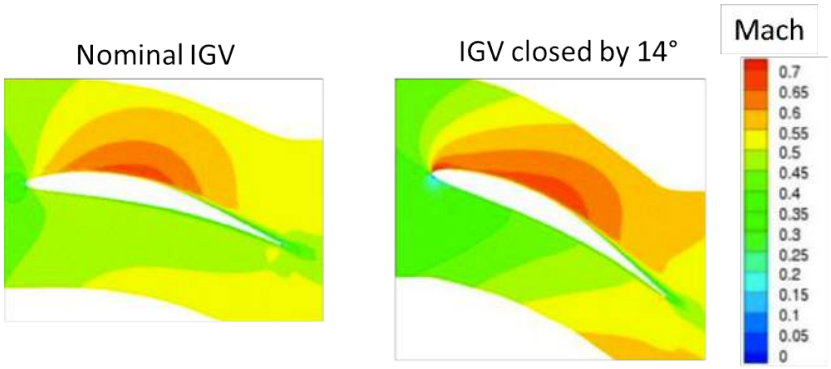

Figure 4.9: Change in flow field (Mach) across the IGV when closing the blade. Contours refer to mid-span

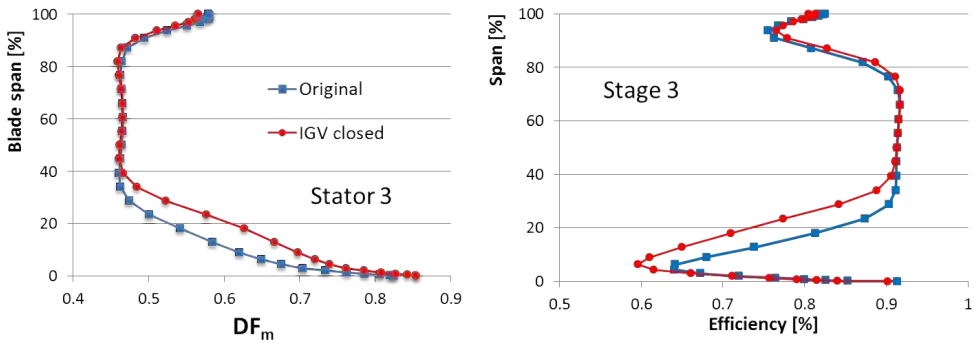

Figure 4.10: Stator 3 diffusion factor and stage 3 efficiency radial profiles

Having evaluated the decrease in compressor performance, the objective was to investigate possible guide vane stagger variations, which could lead to considerable improvements at the predicted lower operating mass flow range. In order to reduce the complexity of the problem and propose an educated guess, stage 1 was first only considered. According to the above analysis, closing stator 1 would alleviate the detrimental effects obtained in the first three blade-rows. First of all, considering an unchanged IGV setting, a further reduction of axial velocity would result in an increase (and thus enhancement) of rotor 1 incidence. Moreover, re-opening the IGV in order to maintain the same air flow rate would allow for an additional and probably more important recovery of stage 1 inflow condition and thus performance. A reduction in IGV losses would also be expected. Figure 4.11 shows the calculated incidence angle spanwise variations with respect to the baseline geometry at the front of the compressor, where the *IGV-S1* configuration refers to the IGV and stator 1 closed by 10° and 6.2° respectively.

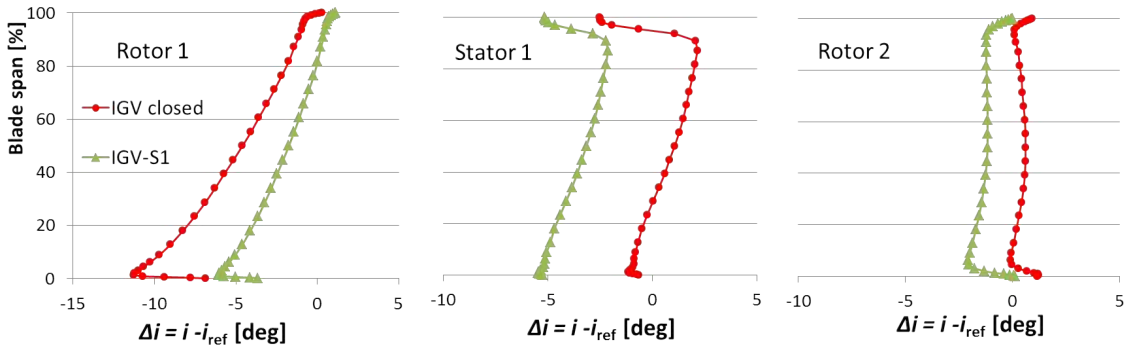

Figure 4.11: Effect of IGV and stator 1 re-staggering on spanwise incidence variations at the front of the compressor

The enhancement of rotor 1 inflow condition can be noticed. The figure also indicates that closing stator 1 leads to a reduction of stator 1 incidence and thus flow pressure rise. In addition, as expected, rotor 2 incidence also decreases. The achieved improvements across the first three blade-rows are illustrated in Figure 4.12, while Figure 4.13 shows the circumferential mass averaged values of the DF_m, DoR, efficiency and pressure ratio for the three different compressor configurations.

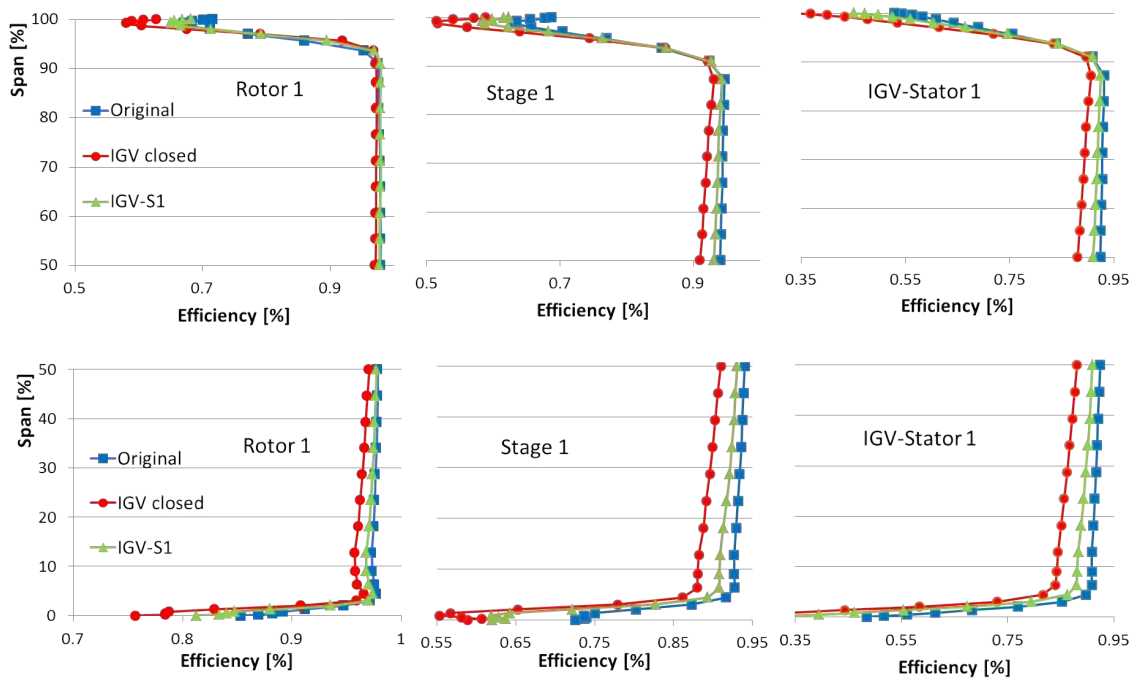

Figure 4.12: First stage performance improvements through IGV and stator 1 re-staggering

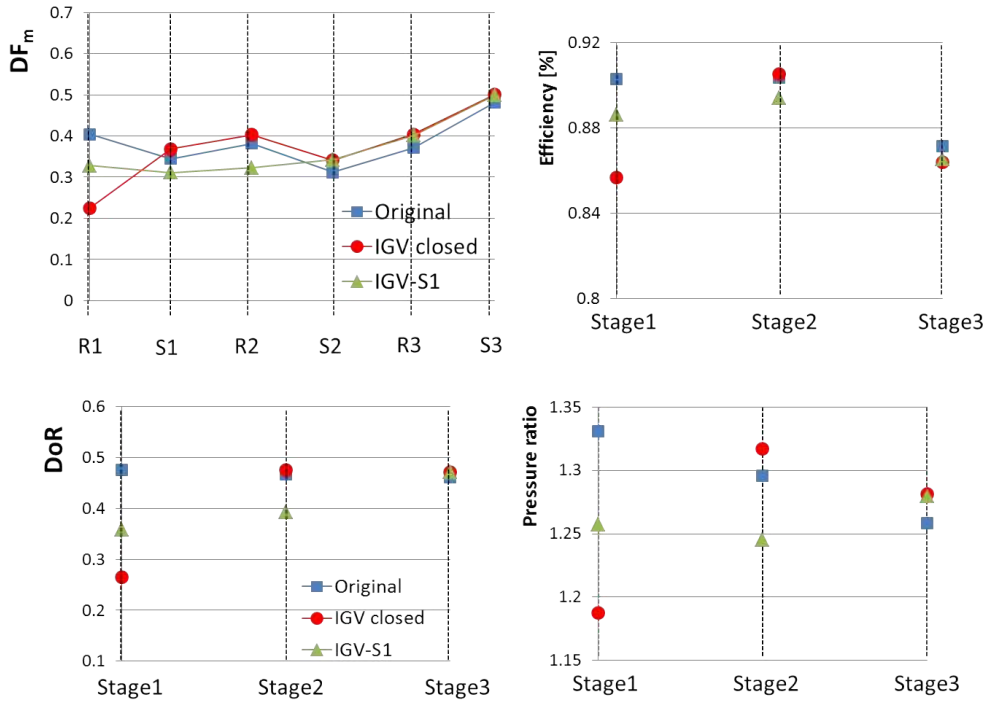

Figure 4.13: Circumferential mass averaged blade and stage parameters (IGV and stator 1 re-staggered configuration)

The results highlight that even an optimisation of the first two guide vanes might not lead to significant overall performance improvement, particularly due to the drop in stage 2 pressure ratio and efficiency that occurs when closing the first stator. From the above, it is believed that a reasonable attempt to provide an efficient level of flow turning across the compressor would be to close the IGV till the point where the IGV profile losses do not increase significantly. The further shift of the working line should be achieved by an appropriate closure of the downstream guide vanes. It may be expected that an optimum VSVs schedule would not be too far from a configuration where the stators are equally re-staggered. A simple re-design was obtained after few trial and error attempts with the intent of re-establishing the original flow diffusion across the machine. In the following figures the results obtained with the new design are referred to as *VSVs*, corresponding to the IGV closed by 7.2° and each stator closed by 6°. First of all it is interesting to highlight the recovery of the original aerodynamic features at the inlet of rotor 1, as shown in Figure 4.14. For completeness the spanwise incidence variations for each blade are shown in Figure 4.15. It can be observed that for the VSVs configuration each rotor operates near its original condition, although a relatively small overloading at the hub regions of rotors 2 and 3 is predicted. The figure finally highlights that each stator guide vane is subjected to a clear reduction of incidence angle along the radius.

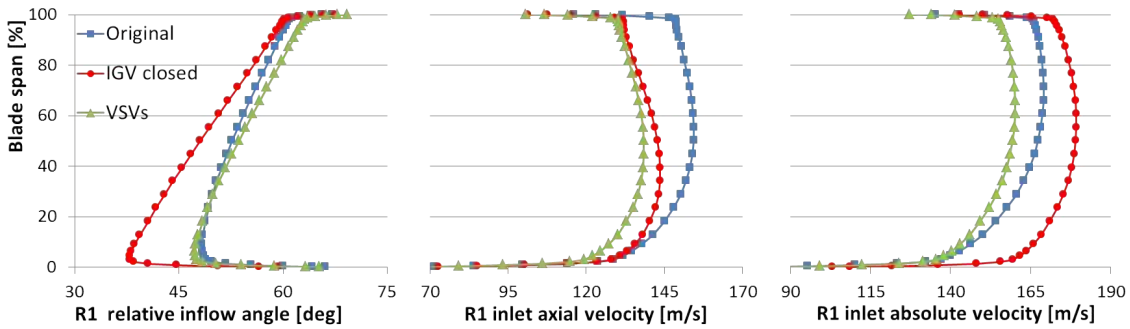

Figure 4.14: Rotor 1 inflow condition re-establishment

The improvements in performance obtained with the re-staggered machine are shown in Figures 4.16 and 4.17.

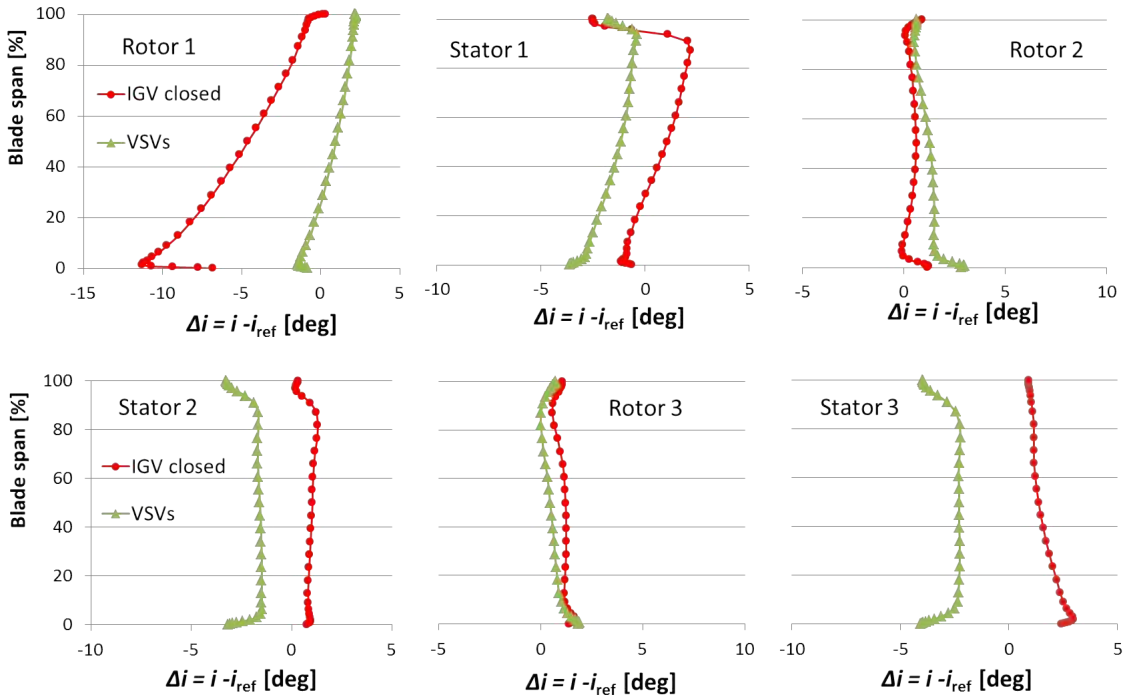

Figure 4.15: Compressor blades spanwise incidence variations

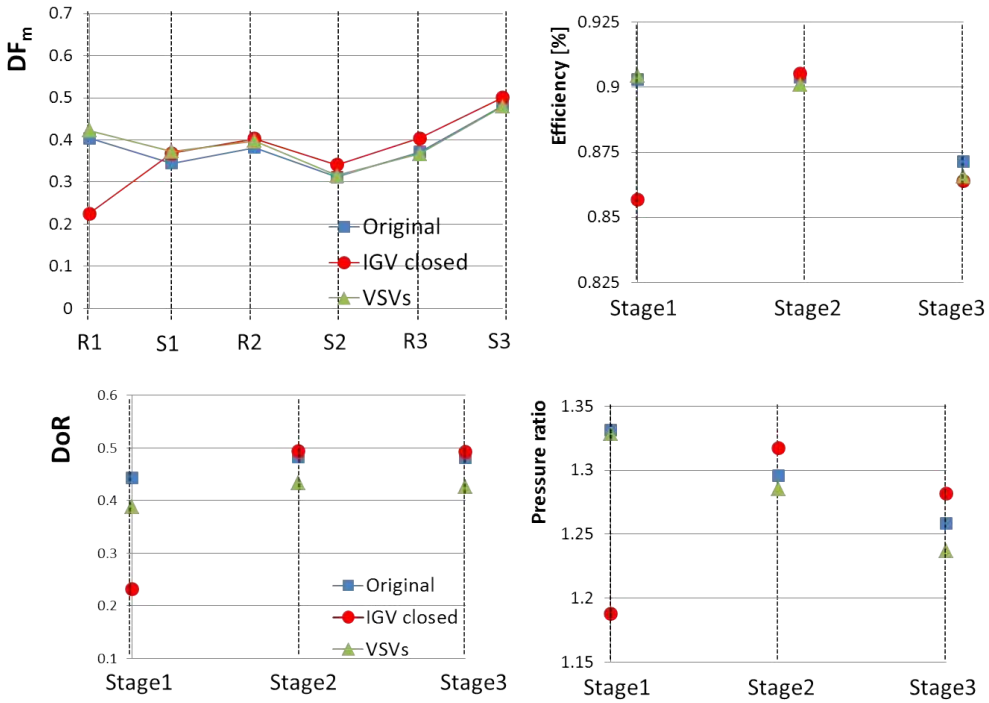

Figure 4.16: Circumferential mass averaged blade and stage parameters (guide vanes re-staggered configuration)

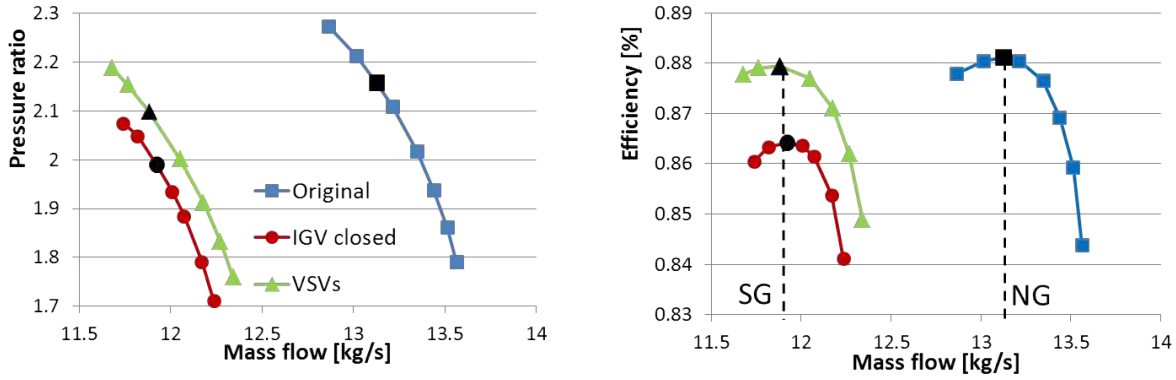

Figure 4.17: Efficient VSVs schedule to accommodate syngas combustion and fuel flexibility

The original stage efficiency is re-established although a decrease in pressure rise is observed across stage 2 and stage 3 mainly due to the expected lower flow turning across the stators and reduction in axial velocity. Overall, at the required mass flow rate (11.93 kg/s) the new compressor operates with similar efficiency (-0.19%) and surge margin (+0.4%) but lower pressure ratio (-3.70%) compared to the reference geometry. An optimisation procedure using stator stagger angles as design parameters may lead to higher improvements but it is believed that, in agreement with conventional part-load operation, a reduction in working pressure ratio is most likely to occur. However, an additional re-design option to further increase the performance and in particular the compressor maximum pressure is discussed in the next section.

4.4 Stator sweep effect on highly loaded subsonic stage

It is known that compressor end-wall regions are critical in terms of overall losses. End-wall losses are generally considered to be of the same order of magnitude as profile losses and, in case of transonic stages, shock losses. In addition, stator end-wall regions of highly loaded stages might be subjected to high diffusion such that large flow separation and pressure losses may occur. In order to optimise the design of a compressor, the application of both sweep and lean has been investigated in stator vanes, with the general aim of reducing the loading of the end-wall sections.

Some studies can be found on the effect of the so called bowed stators, which involve the application of positive lean angle at hub and negative lean angle at the casing (see Figure 4.18). A common result for such configuration is the possibility of shifting low energy fluid regions from both tip and hub towards the mid-span, thus reducing end-wall losses and the tendency of corner stall [84, 85, 86]. This is mainly obtained by the alteration of the radial pressure gradient (and thus imposition of a new radial equilibrium), as a consequence of additional radial forces generated by bowing the stator vanes. In particular, in the front part of the blade (acceleration region) the fluid is driven from the end-walls towards mid-span while the opposite occurs in the aft part of the blade (deceleration region) [84]. Thus, end-wall bowed sections are characterised by lower acceleration with respect to the reference geometry resulting in a reduced adverse pressure-gradient and tendency of the flow to separate in the rear part of the profile. On the other hand, the consequent higher loading at the front part of mid-span regions leads to higher local losses and possibly to trailing edge flow separation. This is why bowed stators might have strong impact on compressor efficiency mainly at near-stall operation and optimum configurations strictly depend on the original flow features. Furthermore, few studies demonstrated that major positive effects of bowed stators are obtained at the hub where aerodynamic loading is higher and separation usually first arises [84, 86].

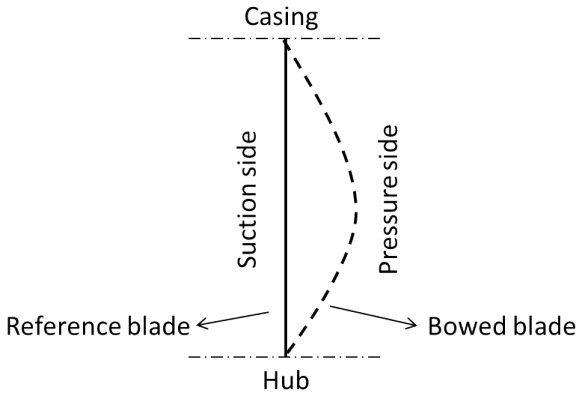

Figure 4.18: Bow stacking line modification

The application of an appropriate sweep might lead to similar improvements by reducing leading edge blade loading and initiating less secondary flows at hub and tip. For instance, Friedrichs et al. investigated the effect of blade sweep in a

highly loaded single-stage stator of a low-speed compressor [87]. Their work showed that the application of forward sweep towards hub and tip regions resulted in surge margin enhancement and significant increase of efficiency and pressure rise in the near-stall operating range.

On the basis of the study reported in Chapter 3, the purpose of this section is to investigate benefits of blade true sweep on the IDAC compressor last stator and thus overall performance. Two different radial stacking line modifications (indicated as *SW-1* and *SW-2*) are considered, as illustrated in Figure 4.19. Recalling Figure 4.10, both configurations involve an increasing positive sweep angle towards the hub from the mean blade region where the CFD predictions indicated the increase in flow diffusion and loss in efficiency. The maximum sweep angle at hub is slightly different in order to explore the sensitivity of the flow field to small geometry variations. Finally, the second re-designed blade also includes tip forward sweep in order to investigate possible benefits at the casing.

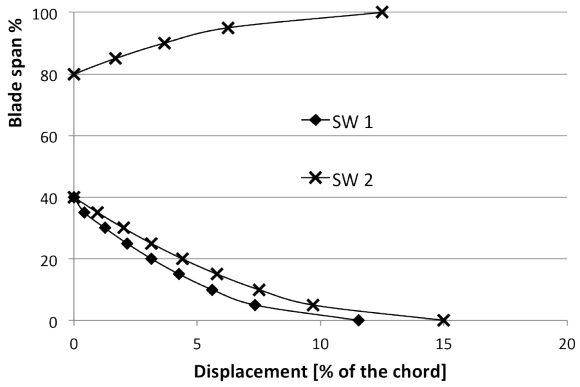

Figure 4.19: Sweep radial stacking line modifications

Figure 4.20 illustrates stator 3 suction side absolute velocity contours (with added streamlines) and static pressure contours. The results are for the same compressor back pressure boundary condition at which maximum efficiency is obtained for the reference blade. The application of sweep reduces the flow separation and considerable improvements are obtained with the second swept blade where the separation region is almost eliminated. It is interesting to observe how a slight increase in the sweep angle at the hub highly enhances the ability to prevent flow separation.

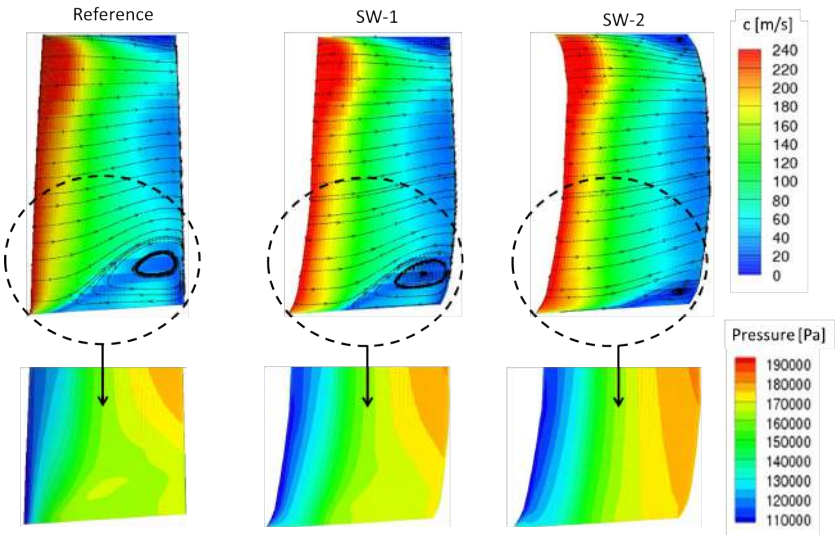

Figure 4.20: Blade sweep effect on stator 3 suction side flow field. Contours refer to absolute velocity (up) and static pressure (down) at peak-efficiency operation

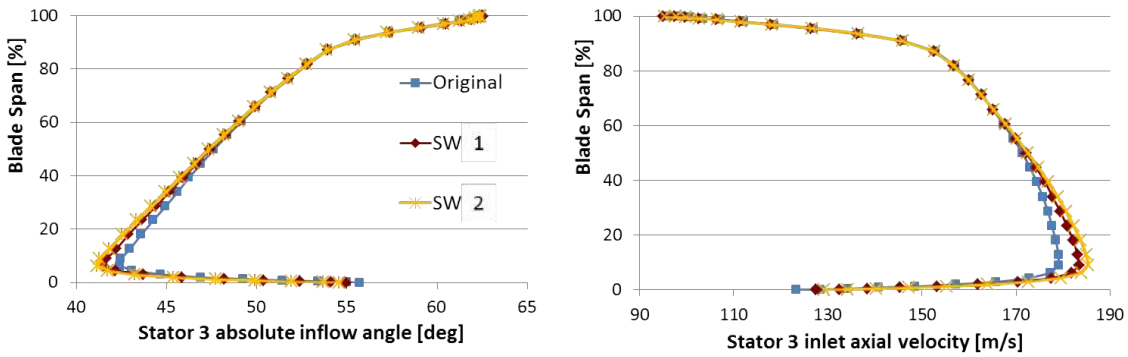

Figure 4.21: Blade sweep effect on stator 3 inflow condition at design point

The static pressure contours suggest that the high acceleration region (low pressure) in the front part of the blade at hub is shifted away from the hub region as a result of a local decrease in incidence and higher axial velocity (see Figure 4.21). This is better highlighted in Figure 4.22, which shows the variation of blade pressure profile near-hub, at mid-span and near-tip sections. It can be observed that the hub leading edge loading and the adverse pressure gradient in the front part suction surface are reduced for both swept configurations, and such effect varies depending on the different swept configurations. Shifting the low momentum fluid away from the hub leads to higher pressure gradient at mid-span and, more in general, flow diffusion towards blade tip regions. This causes small local loss increase and stage performance drop, as can be noticed by inspection of Figure 4.23. Finally, the figure

suggests that the effect of forward sweep at tip is almost negligible, probably due to the fact that compared to hub regions a lower local aerodynamic loading exists.

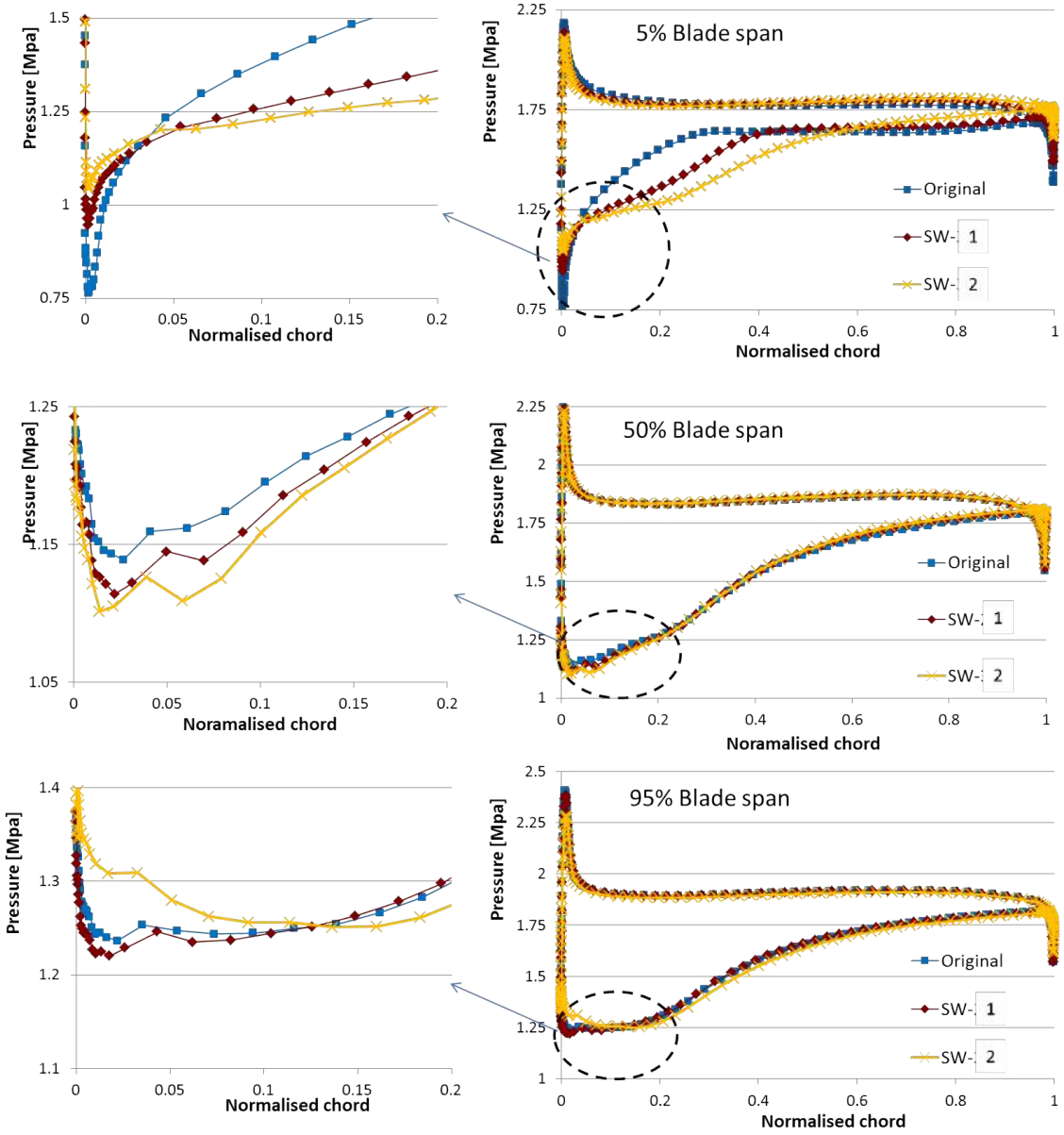

Figure 4.22: Blade sweep effect on stator 3 pressure profiles near-hub, at mid-span and near-tip. Profiles refer to peak efficiency condition

The analysis was repeated at near-stall condition and similar results were obtained. Figure 4.24 shows the predicted compressor maps where the improvements in performance are shown. From the figure it can be deduced that, by reducing the separation region, further increases in efficiency and pressure ratio are achieved.

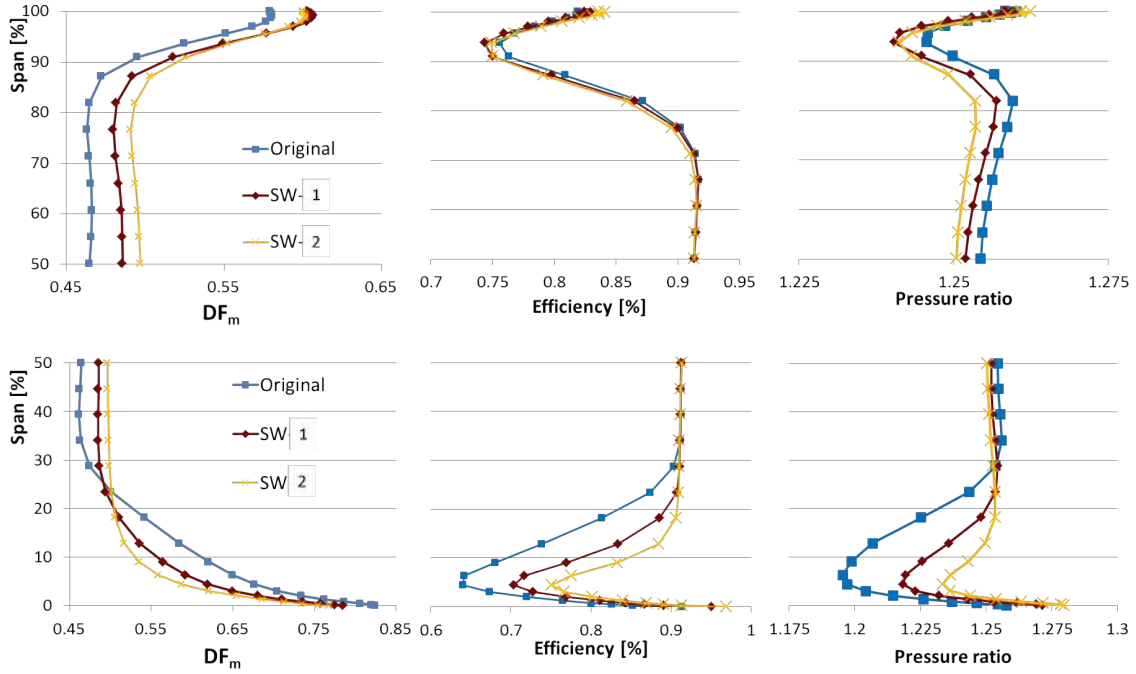

Figure 4.23: Blade sweep effect on stator 3 diffusion factor and stage 3 performance radial profiles at peak-efficiency condition

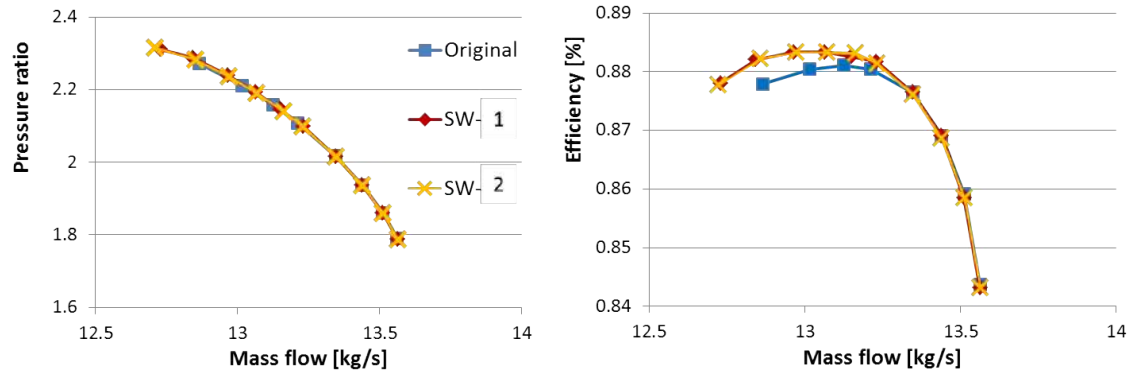

Figure 4.24: Effect of blade sweep on IDAC compressor maps.

The peak-efficiency point moves towards a lower mass flow rate leading to a higher operating flow range and maximum pressure rise. In particular, a surge margin enhancement of about 48% and 52% are provided by the first and second swept blades respectively. It is finally worth noticing that there is no impact on choking mass flow and corresponding performance since at high flow condition the compressor is not subject to flow separation and, more in general, geometry modifications applied to the back of a given compressor typically have lower influence on the inlet mass flow rate.

In the previous section, the proposed VSVs configuration allowed to shift the

working point towards the estimated lower mass flow rate while maintaining the original machine efficiency and surge margin. However, a decrease in pressure ratio was predicted and, as reported in Figure 4.16, the drop in performance was almost equally divided between stage 2 and 3. This is clearly undesirable because the quantity most required from the compressor is reduced. Consequently, the use of blade sweep would allow for a further pressure rise enhancement. For instance, Figure 4.25 shows the performance obtained by applying the SW-2 configuration to the re-staggered compressor geometry (indicated as *VSVs-SW* in the figure). Compared to the reference baseline, the compressor has now an increased surge margin of about 23%. This means that the working line of such compressor could be slightly moved towards higher mass flow rate through a small re-opening of the last two guide vanes. This would allow for a further shifting up of the pressure map at the expense of the compressor stability, as long as the surge margin does not reduce compared to the original value. An attempt has been made by opening stators 2 and 3 by 1° and the results are reported in Figure 4.25, indicated as *VSVs(2)-SW*. This last configuration has slightly higher efficiency and surge margin and almost completely recovered pressure ratio with respect to the baseline compressor.

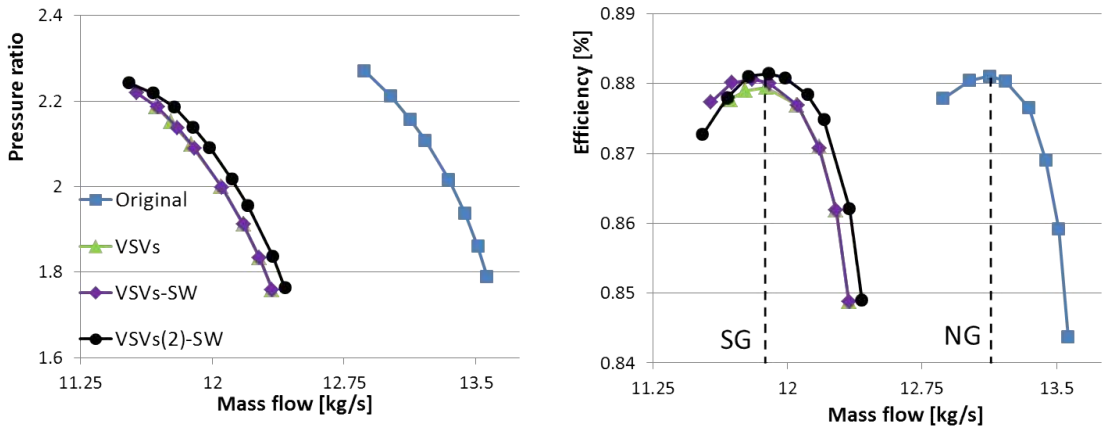

Figure 4.25: Effect of blade sweep on re-staggered geometry compressor maps.

4.5 Summary

In this chapter the benefits of VSVs application within the context of this research have been explored on a multi-stage axial compressor. The shifting of the working

line towards lower mass flow range due to syngas combustion could be thought of as a typical combined cycle part-load operation. The results showed that an appropriate re-staggering of the guide vanes would lead to an efficient flow matching at the inlet of the rotors, suggesting that a desirable blade flow turning and diffusion can be achieved for the new operating range. However, the large stator re-staggering, required in order to re-establish rotors loading while avoiding excessive IGV pressure losses, imply a reduction of stator flow incidence and pressure rise. This may explain the reduction in pressure ratio typically observed during conventional power modulation operation. Since for the new nominal condition the original pressure ratio should be maintained, further modifications need to be adopted. For instance, in this work it was shown that by applying blade true sweep in highly loaded stators would allow to increase the compressor maximum pressure and extend the mass flow range. Benefits are provided at different flow rates, wherever stator end-wall flow separations are believed to be the major trigger for compressor stall. As a result, a combination of VSVs schedules and blade sweep would represent a viable solution for the fuel-flexibility requirement. Considering that power control strategy would be also required for the new machine, the installation of a relatively high number of variable guide vanes is mandatory. However, hypothetical syngas part-load operation have not been here considered. These will be discussed in Chapter 6 for the more conventional compressor.

Chapter 5

Compressor 3D geometry design for NGCC power plants

5.1 Introduction

At the start of the H2-IGCC project, it became apparent that a reference gas turbine operating with natural gas needed to be designed for the study as actual designs are protected by industrial confidentiality. Such design, if used in the project, will not be available for public distribution. Thus, it was decided to generate a generic geometry based on known features of modern gas turbines, which will be termed as *baseline geometry*. The basic outline of the gas turbine is produced by a project partner using a validated energy conversion power plant simulator (ECPPS) based on available manufacturers data of similar machines. The simulator provides the preliminary and through-flow analyses. Once the through-flow design is completed the 3D blading of both compressor and expander, as well as cooling channels geometric details, are defined. The specific task of the present work is to produce an efficient 3D blade design for the 15 stage axial compressor that would match the performance predicted by the ECPPS in terms of pressure ratio at different load condition. This chapter focuses on the methodology used in this study to generate the geometry of the different compressor blades and the resulting 3D flow features at nominal and off-design condition are analysed. The baseline machine will be used as reference for the investigation of required compressor modifications in order to accommodate specific syngas combustion operation. These are discussed in the following chapter.

5.2 Baseline gas turbine

In this section the design parameters and performance of the baseline gas turbine provided by the ECPPS are presented. Detailed description of the ECPPS model is beyond the scope of this thesis and full details can be found in [88, 89, 18, 90]. A qualitative brief description of the model will be given in the next section.

The simulator has been developed taking into consideration the specifications of the 250-340 MW F Class gas turbines latest technologies, based on available Original Engine Manufacturers (OEMs) data (Alstom, Ansaldo, GE, Mistsubishi and Siemens). In particular, in agreement with H2-IGCC partners, the Siemens SGT5-4000F [91] and the Ansaldo AE94.3A [92] have been selected as the main reference gas turbines. The procedure of modelling, sizing, analysing and matching each component of the baseline gas turbine is illustrated in [90]. The resulting design parameters at nominal condition are given in Table 5.1.

The baseline gas turbine consists of a 15 stage axial compressor and 4 stage expander. Based on the overall system design, compressor bleeds are extracted from stages that allow a sufficient over pressure compared to that of the expander blade-rows to be cooled. The first three bleed extractions are located along the compressor casing, while the last extraction is taken at the compressor outlet. The through-flow shape of the machine is shown in Figure 5.1, with arrows showing extraction and cooling flow streams. Figure 5.2 shows the pressure ratio maps predicted by the ECPPS at different load operation. These have been obtained using the TIT constant and IGV only control strategy, which has been discussed in Chapter 1. A lowest allowable surge margin (LASM) line is given together with the expected compressor safe operation limits (surge and choke lines).

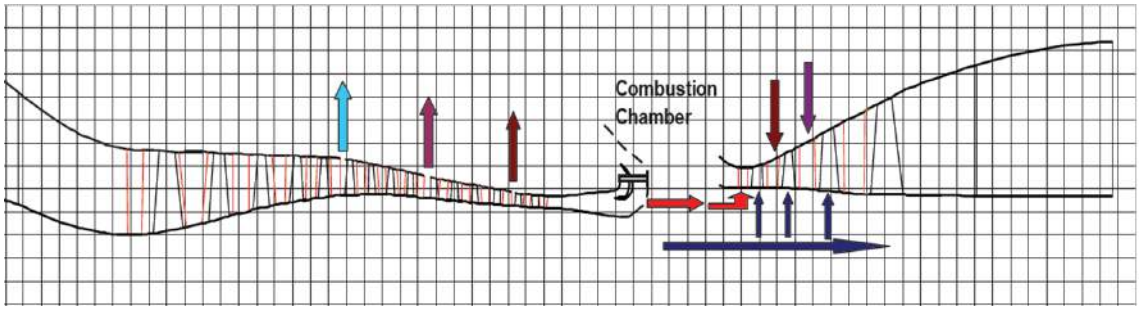

Figure 5.1: Baseline gas turbine through-flow shape

Table 5.1: Design parameters and performance of the baseline gas turbine

Compressor	
Inlet pressure (kPa)	101.3
Inlet temperature (°C)	15
Inlet mass flow rate (kg/s)	685.4
1^{st} bleed mass flow rate (kg/s)	13.71
2^{nd} bleed mass flow rate (kg/s)	26.73
3^{rd} bleed mass flow rate (kg/s)	52.78
4^{th} bleed mass flow rate (kg/s)	82.25
Exit temperature (°C)	398.6
Pressure ratio	18.2
Power consumption (MW)	262.9
Combustion Chamber	
Fuel LHV (MJ/kg)	50.1
Fuel flow rate (kg/s)	15.0
Power introduced by the fuel (MW)	752.7
Expander	
TIT (°C)	1440.0
TET (°C)	568.0
Mechanical power (MW)	573.6
Gas turbine	
Net electric power (MW)	299.6
Specific consumption (kJ/kWh)	9042.0
Thermal efficiency (%)	39.8

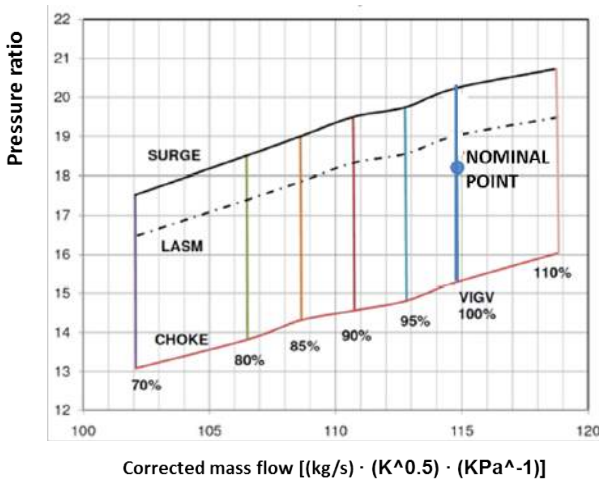

Figure 5.2: Pressure ratio maps for the baseline (natural gas combustion) compressor geometry predicted by the ECPPS

5.3 ECPP Simulator

The methodology is based on a number of steps. A preliminary evaluation of the thermodynamic cycle is first performed assuming suitable values of global quantities, such as compressor inlet mass flow rate, pressure ratio, fuel composition and its LHV, TIT, coolant temperature, compressor inlet and expander outlet boundary conditions and gas turbine power output and efficiency. Most of these quantities are typically selected on the basis of available manufactures data of similar machine level class. Choosing the power plant efficiency or power output as objective function, an optimisation can be applied in order to calculate thermodynamic quantities at inlet and outlet of main system components. Once the cycle is determined, the sizing of the power plant components (compressor, combustor, expander, bottoming cycle elements and other minor components) is performed. Geometrical and other global quantities available from commercial machines and technical background are constrained in order to search for unknown data using an inverse sizing problem. This allows for the prediction of the off-design and part-load behaviour of each component. Components matching is the last step.

The modelling approach is based on a finite volume (FV) discretisation of the gas turbine elements [90]. For example, Figure 5.3 shows a multi-stage compressor model. The compressor is divided into sub-components (FVs) each representing a blade-row cascade. For each control volume, the governing equations that describe

the behaviour of the flow are applied at the inlet and outlet nodes laying on an approximate streamline. For the compressor, the equation set contains conservation laws (mass, momentum and energy) and empirical correlations for calculating the different type of losses as well as incidence and deviation angles. In addition, isentropic and polytropic process relations are used in order to determine the thermodynamic properties. The cascade features are averaged in the central node. Similar approaches are adopted for other components. Clearly, depending on the system element, different equations are involved that account for other type of process, such as, for instance, heat transfer and chemical reaction. The simulator models include equations and empirical correlations that describe phenomena of stress, corrosion, creep and other significant aspects needed to evaluate the lifetime of the gas turbine. Emissions, cost and control aspects are also taken into account. Each component is therefore described by a highly non-linear set of equations and the different sets of equations are solved in parallel. The results are iterated until a desired sizing of the gas turbine elements is achieved. This is done using an optimisation method [89].

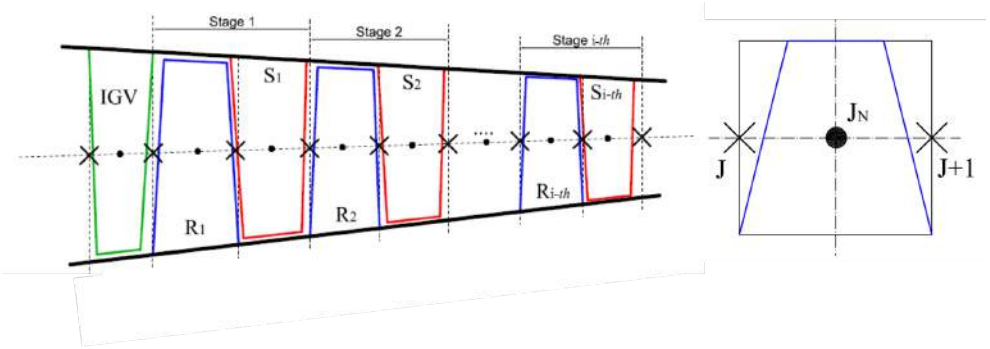

Figure 5.3: Compressor row-by-row scheme. Stations and central node of a generic finite volume row

5.4 3D compressor blade design and mesh generation

This section focuses on the compressor 3D blade design. The main purpose is to generate an efficient compressor geometry that would match the stability margin at different load condition suggested by ECPPS. The baseline geometry will be used for

exploring re-design strategies in order to cope with the surge margin reduction when a specific H_2-rich syngas is burned. The ECPPS provides the compressor annulus line at hub and tip, number of stages and number of blades for each blade-row. It also provides a two dimensional profile used for the through flow analysis at a nominal radial section (type of profile, thickness distribution, stagger angle, flow and blade angles). Transonic profiles (double circular arc, DCA) are used in the first three stages, while NACA 4-digitis and NACA 65-series are used from stage 5 to stage 8 and from stage 9 to stage 15 respectively. In terms of aerodynamic performance, the most advanced 3D blade design technologies are represented by the so called *controlled diffusion* (CD) and *prescribed velocity distribution* (PVD) airfoils [93]. There are no general rules that can be applied, and typically these types of airfoil are a result of Mach number blade profile optimisation. However, specific profiles of the desired characteristics must be at least initially designed. In this work, this is achieved via analytic tools and design refinement using CFD.

5.4.1 Flow and blade angle spanwise distribution

Knowing the velocity diagram at a given reference radius, the first step for determining the 3D blade geometry parameters is the calculation of the spanwise variations of the flow angles. These could be accurately calculated by applying streamline curvature methods. At each flow station, these methods typically solve the 3D full radial-momentum equation while manipulating the annulus area until a desirable velocity triangle radial distribution is obtained [94]. This requires an iterative procedure and, particularly for high number of stages, high computational effort. Consequently, for preliminary 3D design, simpler criteria exist. These are based on the design condition of *constant specific enthalpy at all radii* ($dh_0/dr = 0$), which sets the coupling relation between whirl and axial velocity at any inter-row plane. Recalling Figure 3.1, a general form of a given rotor blade-row inlet and outlet whirl velocity radial distributions is given by [12, 27]:

$$c_{w,1} = aR^n - \frac{b}{R} \quad ; \quad c_{w,2} = aR^n + \frac{b}{R} \tag{5.1}$$

where a, b and n are constants and R is the radius-to-"reference radius" ratio r/r_{ref}, with r_{ref} typically corresponding to a mean diameter. Particular cases that consider specific values of the index n are described in the literature [12]. For a given criterion, a and b are not arbitrary constants but depend on the values of the degree of reaction (DoR) and stage stagnation temperature rise provided by the preliminary design at the reference radius. In particular, a and b can be determined by calculating the whirl velocities at the reference radius using the following equations [12]:

$$c_{p,a}\Delta T_0 = u(c_{w2} - c_{w1}) \tag{5.2}$$

$$DoR = 1 - \frac{c_a}{2u}(\tan\beta_2 - \tan\beta_1) = 1 - \frac{c_{w2} + c_{w1}}{2u} \tag{5.3}$$

Once the spanwise variations of the whirl velocities are determined, the distribution of axial velocity can be found by integrating the simplified radial equilibrium equation:

$$\frac{1}{r^2}\frac{d}{dr}(r^2 c_w^2) + \frac{d}{dr}c_{ax}^2 = 0 \tag{5.4}$$

Equation 5.4 is derived by imposing the balance between pressure and inertial forces on the fluid element and considering the constant specific enthalpy design condition along the radius. The equation, however, does not take into account the additional pressure gradient due to the change of radius of streamlines along the compressor stages. Therefore, 3D blade design obtained from criteria based on the assumption of $dh_0/dr = 0$ require geometric corrections, particularly at the end-walls of low hub-to-tip ratio blades. These can be applied using feedback from three-dimensional CFD analyses. Design refinement should be carried out calculating the DF, blade inlet Mach number spanwise distributions and DoR. In particular, as discussed in Chapter 3, maintaining the DF below 0.6 for rotor hub

and stator vanes end-wall regions is considered a fundamental design criterion [94]. Furthermore, as the DF approaches the critical value, stator hub end-walls might experience significant flow separation and losses would increase more rapidly than compared to rotor hub regions. It is known that for constant work input the stage loading coefficient decreases towards the tip. The reason why stator vanes are more sensitive to hub-corner separation than rotor blades seems to be related to the centrifugal forces that push the rotor blade suction surface boundary layer outwards, thus reducing any separated regions at the hub [95]. As discussed in Chapter 3, rotor tip regions instead become particularly critical in the case of strong shock/boundary layer interaction which may cause local flow separation. According to the above, another desirable requirement is to avoid relatively low values of DoR towards hub, which imply high stator diffusion [87]. In many cases, however, the DoR is not a free design parameter since it might be constrained by more stringent conditions established by DF and Mach number [12, 76].

In this work, the use of the design criteria known as *constant degree of reaction* and *exponential* with the imposition of the simple radial equilibrium have been first attempted. For a given rotor blade-row, the reference radius r_{ref} was derived from the inlet and outlet tangential velocities provided by the ECPPS at the nominal section. For both criteria, however, due to the low hub-to-tip ratio of the front stages, the 3D analytical calculation led to unrealistic shapes of the rotor outlet velocity diagrams at the tip. In particular, because of the significant reduction of the axial velocity towards the casing, both inlet and outlet relative flow angles of the first two rotors were very large, suggesting a tip stagger angle slightly lower than 90°. It is believed that, if required, designers apply some *a priori* corrections at the end-wall based on experience.

Consequently, another analytical method has been adopted. The design criterion is known as $\beta_2 = \text{constant}$ [27], with β_2 being the rotor outlet absolute angle, as indicated in Figure 3.1. The method is briefly described as follows. The following rotor whirl velocity distributions are imposed:

$$c_{w,1} = c_{w,2} - \frac{b}{R} \quad ; \quad c_{w,2} = k \tag{5.5}$$

where b and k are constants determined from the knowledge of the inlet and outlet velocity diagrams at the reference section provided by the ECPPS. The specific enthalpy along the span is given by:

$$c_{p,a}\Delta T_0 = u(c_{w,2} - c_{w,1}) = \omega b = \text{constant} \tag{5.6}$$

From Equation 5.3, the DoR varies with the radius with the following relation:

$$DoR = 1 - \left(\frac{c_{w,2}}{\omega r} - \frac{b}{2\omega r^2}\right) \tag{5.7}$$

The axial velocity is assumed constant. Most of the criteria that impose a constant axial velocity typically lead to a lower degree of stagger from hub to tip and do not satisfy Equation 5.4. However, as discussed, the overall radial equilibrium is not guaranteed in any case when the flow is subjected to curvature in the axial-meridional plane and adjustments are needed.

Once the inflow and outflow angle radial distributions for each rotor blade-row are established, the geometrical blade parameters are calculated. Referring to Figure 3.4, the blade inlet angle ($\alpha_1^{'}$) is first determined assuming the incidence angle provided by the ECPPS at the reference section to be constant along the radius. Such a preliminary assumption is based on the fact that for relatively low inlet Mach number (≤ 0.75) the performance is tolerant to a range of incidence [59]. As it will be illustrated, this is the case for all the blade-rows with the exception of the front transonic rotor tip regions. Howell modification of Carter's rule, based on empirical correlations, has been used to calculate the deviation angle (δ) [96]:

$$\delta = m\theta(s/l)^{0.5} \quad ; \quad m = 0.23\left(\frac{2q}{l}\right)^2 + 0.1\left(\frac{\alpha_2}{50}\right) \tag{5.8}$$

where s is the blade pitch, l is the blade chord length and q is the distance of the point of maximum camber from the leading edge. The pitch/chord ratio is

a key parameter of the mean line design. In order to provide high stage loading (which allows to a reduce the number of stages) and maintain an acceptable level of diffusion, a low value of s/l is required. On the other hand, this implies a large number of airfoils and therefore higher wetted area and profile losses. For this reasons s/l values are typically in the range 0.8 to 1.2. The pitch/chord ratios provided by the ECPPS have been fixed for the purpose of this study. Assuming the frequently adopted circular arc camber line ($2q/l = 1$) and a constant rotor blade chord length along the radius, the camber angle (θ) can be determined:

$$\theta = \alpha_1^{'} - \alpha_2^{'} = \alpha_1^{'} - \alpha_2 + \delta = \frac{\alpha_1^{'} - \alpha_2}{1 - \left[0.23 + 0.1\left(\frac{\alpha_2}{50}\right)(s/l)^{0.5}\right]} \tag{5.9}$$

Consequently, the blade outlet angle ($\alpha_2^{'}$) and deviation angle can be determined from Equation 5.9. The stagger angle is calculated as $\zeta = \alpha_1^{'} - \theta/2$. A radial variation of the maximum thickness (t_{max}) is considered. For example, for this type of machine, a suitable value of t_{max} for DCA tip profiles is about 2% of the blade chord (for instance 6 mm for the first rotor). The spanwise variation is simply calculated by linear interpolation using the values at tip and reference radius, the latter provided by the ECPPS. Rotor tip clearances have been set to 0.7%, 0.6% and 0.5% of the relative blade length of the front (DCA), middle (NACA 4-digits) and rear (NACA 65-series) stages respectively. This choice was made in order to keep the tip gap size nearly constant along the compressor, with a suitable value of about 1 mm. Stator blade geometric parameters are calculated in a similar manner, since the inlet and outlet velocity diagram radial variations are known from the adjacent rotors. According to Equation 5.5, stator blades are not twisted at the inlet and are twisted at the outlet. Stator chord lengths are not assumed constant. In particular, the chord length is linearly increased from hub to tip in order to match the value provided at the reference radius and maintain a nearly constant stator axial chord along the span. This allows to avoid a large increase of axial gaps between blade-rows towards the casing. The three-dimensional IGV geometry is generated assuming an inlet axial flow and using the following correlation for the deviation angle: $\delta = m\theta(s/l)$ where $m = 0.19$ [12].

5.4.2 Geometry generation

The in-house mesh generator requires a formatted input file for blade geometry data. For a given blade, this file must contains an appropriate profile point (cylindrical coordinates) distribution at different spanwise levels. A FORTRAN program has been written for this purpose. The following sections describe the methodology adopted in the program in order to discretise the pressure and suction sides of the different types of profiles used in the H2-IGCC compressor. In addition to the annulus lines, the ECPPS provides the leading and trailing edge coordinates at hub and tip for each blade-row. However these data are only indicative of the position of a given blade since they strictly depend on the 3D twisting criterion adopted. Therefore only the leading edge hub coordinates predicted by the simulator are fixed and provided to the 3D geometry program. Additional input data are the geometric parameters needed to define the airfoil section at different radial levels (chord length, blade geometry angles, maximum thickness and maximum camber). As previously mentioned, the blade shapes have not been optimised, thus a circular camber line is always considered (maximum camber at 50% of the chord length) and the chord-wise position of maximum thickness is fixed as that of the basic profile. In the next subsections the basic features of the type of profiles used in the H2-IGCC compressor are described.

DCA profiles

The basic DCA profile is constructed with both surfaces formed by circular-arcs with the maximum thickness at 50% of the blade chord (see Figure 5.4). This type of blade section is widely used at high (transonic and supersonic) inlet Mach number, since it allows for better performance and wider operating range (in terms of pressure losses as function of incidence angle) compared to other type of airfoils [59]. Generally, DCA profiles provide a more satisfactory pressure distribution on both pressure and suction surfaces and in particular minimise the velocity peak on the front part of the suction surface. Within the limits of mechanical integrity constraints, the sharp leading edge and flat suction surface allow to decrease the Mach number in front of the passage shock, thus reducing the shock-boundary layer interaction. For high blade speed and high relative supersonic inlet flow, the maximum thickness chord-

wise location plays a fundamental role in terms of blade performance. Typically, a desirable location for tip sections would be in rear part of the blade within a range from 55% and 65% of the chord length [33]. This allows to minimise the effects produced by the shock-boundary layer interaction while avoiding the risk of trailing edge boundary layer separation. However, for the reasons previously discussed, changes in maximum thickness positions have not been taken into account in this work.

The construction of the blade is based on the methodology described in [97]. Referring to Figure 5.4, first of all the blade leading edge coordinates are assumed to be $(-l/2, 0)$ and the stagger angle is considered equal to zero at each radial level. The circular-arc camber line is defined by the blade camber angle (θ) and chord length (l). The centre of the curvature of the camber line C is found from the intersection of the segments $\overline{LC}$ and $\overline{TC}$. These are perpendicular to the tangents to the camber line at the leading edge and trailing edge points respectively. The coordinates of C are $(0, y_C)$ where y_C and the radius of curvature R_C are given, after some algebra, by the following expressions:

$$y_C = -\frac{l}{2\tan(\theta/2)} \tag{5.10}$$

$$R_C = \frac{l}{2\sin(\theta/2)} \tag{5.11}$$

The camber line coordinates at the midchord are $(0, y_Q)$ where $y_Q = R_C + y_C$. Pressure and suction surfaces circular-arcs are constructed. The suction surface construction is illustrated here. The distance from midchord to the centre of the trailing edge is given by:

$$\Delta x_S = (R_S - r_0)\sin(\theta_S/2) = l/2 - r_0\cos(\theta/2) \tag{5.12}$$

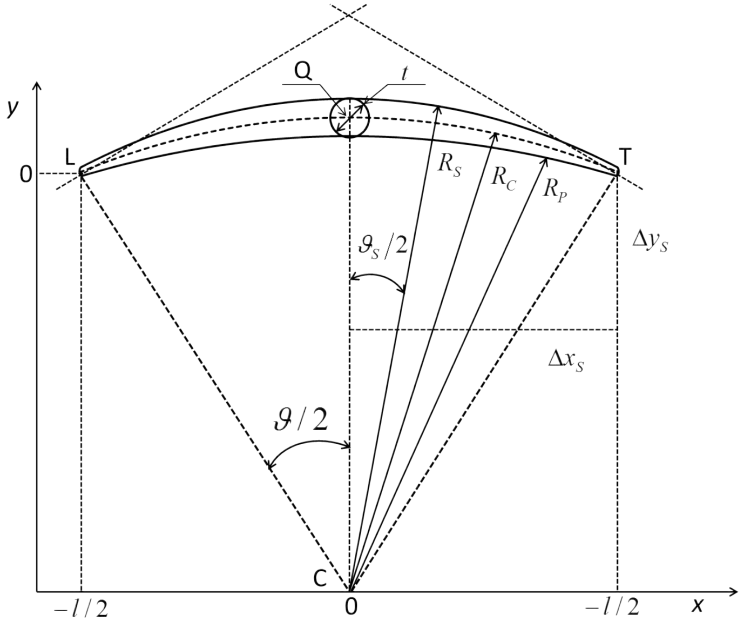

Figure 5.4: Double circular arc profile construction

where $r_0 = 0.12t_{max}$ is the blade nose radius, t_{max} is the maximum blade thickness, R_S is the suction side radius of curvature and θ_S is shown in Figure 5.4. The distance Δy_S is calculated as:

$$\Delta y_S = R_S - y_Q - t_{max}/2 + r_0 \sin(\theta/2) \tag{5.13}$$

Defining $d = y_Q + t_{max}/2 - r_0 \sin(\theta/2)$, after some algebra the suction surface curvature radius can be expressed as

$$R_S = \frac{d^2 - r_0^2 + [l/2 - r_0 \cos(\theta/2)]^2}{2(d - r_0)} \tag{5.14}$$

The origin of the radius is at $(0, y = y_Q + t/2 - R_S)$. Once R_S and its origin are determined, the upper surface of the blade is discretised using polar angles from $-\theta_S/2$ to $-\theta_S/2$. The construction of the pressure side surface is similar, expect that the parameters t_{max} and r_0 are taken as negative. The leading and trailing edges are constructed around their center at $(x = \pm[l/2 - r_0 cos(\theta/2)], y = r_0 \sin(\theta/2))$ to blend with the suction and pressure circular arcs.

NACA 4 digits profiles

The blade profile is described by four digits. The first digit indicates the maximum camber (m) as percentage of the chord. The second digit specifies the distance (n) of maximum camber from the profile leading edge in tens of percents the chord, while typically the maximum thickness is found at 30% of the chord. The last two digits define the maximum thickness as percentage of the chord. The camber line is calculated as follows:

$$y_c = \begin{cases} mx(2n - x)/n^2, & \text{for } 0 \leq x \leq n \\ m[(1 - 2n) + 2nx - x^2]/(1 - n), & \text{for } n \leq x \leq l \end{cases} \tag{5.15}$$

The suction and pressure side coordinates, (x_s, y_s) and (x_p, y_p), are determined and discretised using the following relationships:

$$\begin{aligned} x_s &= x - y_t \sin\theta \\ y_s &= y_c + y_t \cos\theta \\ x_p &= x + y_t \sin\theta \\ y_p &= y_c - y_t \cos\theta \end{aligned} \tag{5.16}$$

where $\theta = tan^{-1}(dy_c/dx)$ and y_t is the thickness distribution of the related symmetric profile given by:

$$y_t = \frac{t_{max}}{0.2}(0.2969\sqrt{x} - 0.126x - 0.3516x^2 + 0.2843x^3 - 0.1015x^4) \tag{5.17}$$

Differently from the DCA, the leading and trailing edge radii end their origins are not defined *a priori*. The methodology used in this work to construct the leading and trailing edges is shown in Figure 5.5. For instance, the leading edge radius centre (located on the camber line) is determined by the intersection of the normals to $\overline{AB}$ and $\overline{DE}$ passing by the mean points of such segments. According to the

literature, $\overline{AB}$ and $\overline{DE}$ are defined in such a way to produce a leading edge that approximates a cylinder with a radius given by $r_{o,LE} = 1.102t^2_{max}$. Similar approach is used to construct the trailing edge. The trailing edge radius is set to equal approximately 0.8% of the chord length, in agreement with the NACA 65 airfoil thickness distribution for compressor applications discussed in the next section.

To the knowledge of the author NACA 4 digits are not widely used in compressor design. The reason of choosing this type of profile to generate the middle stage compressor blades has not been clarified by the project partner. However a possible explanation is discussed in Section 5.6, where the predicted compressor flow features are analysed.

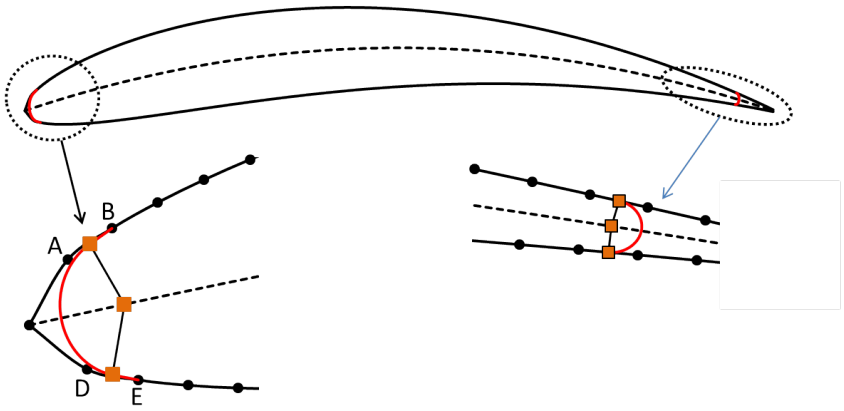

Figure 5.5: Leading and trailing edge constructions for NACA blade profiles.

NACA 65 series

NACA 65 profile was derived from NACA aircraft wing airfoils with a particular distribution of camber and thickness in order to provide an approximately uniform pressure difference (loading) between suction and pressure surfaces along the chord. The maximum thickness always occur at 40% of the chord. These airfoils are specified by their lift coefficient C_L and maximum thickness-to-chord ratio.

Table 5.2: Camber and thickness of NACA 65-(10)10 profile

% chord	Half thickness (% chord)	Camber line (% chord)
0	0	0
0.5	0.772	0.25
0.75	0.932	0.35
1.25	1.169	0.535
2.5	1.74	0.93
5	2.177	1.58
7.5	2.647	2.12
10	3.04	2.585
15	3.666	3.365
20	4.143	3.98
25	4.503	4.475
30	4.76	4.86
35	4.924	5.15
40	4.996	5.355
45	4.963	5.475
50	4.812	5.515
55	4.53	5.475
60	4.146	5.355
65	3.682	5.15
70	3.156	4.86
75	2.584	4.475
80	1.987	3.98
85	1.385	3.365
90	0.81	2.585
95	0.306	1.58
100	0	0
LE Radius	0.687	-
TE Radius	0.0	-

For example, the basic airfoil ($C_L = 1.0$ and $t_{max}/l = 10$) specification is given as 65-(10)10, where the number in parentheses is the lift coefficient in tenths and the final number is the thickness-to-chord ratio as a percentage. The camber line and thickness distribution coordinates of the basic profile are given in Table 5.2, where the half thickness is applied perpendicularly to the local camber line at the chord-wise specified location. The reference profile has a cusped trailing edge radius, which is inappropriate for compressor applications from a structural point of view. Therefore different thickness distributions exist in the rear part of the blade and the modification proposed by Kovach and Sandercock is used in this work [97]. In this variant the baseline thickness distribution is kept the same from the leading edge to 60% of the chord and then varied linearly to match a trailing edge radius equal to 0.8% of chord. The camber line given in Table 5.2, defined for $C_L = 1.0$, becomes infinite at the leading and trailing edges leading to a not simple analytical form. Thus, in practical applications a circular camber line passing through the end points and the point of maximum camber at mid-chord is typically adopted, which differs slightly from the original one. Multiplying the coordinates of such camber line by different values of C_L allows to determine other camber lines. The construction of the leading and trailing edge radii is obtained as described in the NACA 4 digits section.

Mesh generation

Once the required spanwise distributions of camber and thickness of a given blade are defined, each section is staggered by rotating the airfoil around its geometric centre. The blades are shifted in the axial direction according to the leading edge hub coordinates and interpolated with the annulus lines provided by the ECPPS. For each blade, the related file containing the point (cylindrical coordinates) distribution is provided to SURFM and the mesh is generated. Figure 5.6 shows the meridional view of the 15 stage compressor as well as the top view (tip surfaces) of the IGV and first stage grid resolution. Table 5.3 shows the averaged number of points used for each rotor blade and guide vane including the radial and tip gap level distributions. For completeness the number of points used to generate the bleed mesh blocks is also reported. The total number of points of the compressor domain is about 4,400,000.

The boundary conditions and procedure adopted in order to perform steady state CFD simulations for the 15 stage compressor are described in the next section.

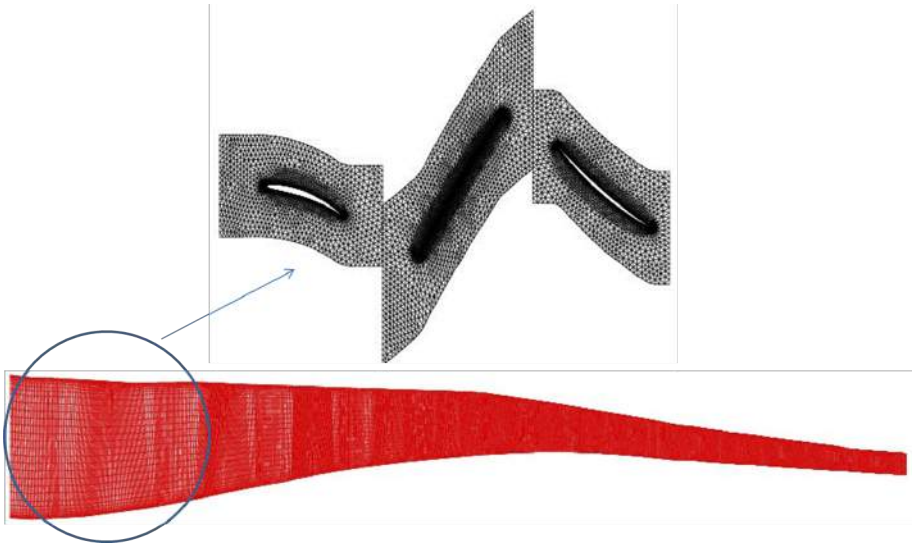

Figure 5.6: H2-IGCC compressor grid

Table 5.3: H2-IGCC compressor grid resolution

	No. of Points	Radial Levels	Tip Gap Levels
Rotor blade	160,000	35	6
Stator vane	120,000	35	-
Bleed	25,000	35	-

5.5 Design refinement using CFD

The first stage (including the IGV) is first simulated and characteristic curves are mapped considering ambient conditions (total temperature and total pressure) and uniform axial flow at inlet and imposing a suitable static pressure downstream. The outlet flow conditions are used as inlet conditions for the next stage, and so on. Bleeds are simulated using mesh blocks at the specified inter stage locations and applying static pressure outlet boundary condition along the casing surface in order to extract the desired amount of coolant (see Figure 5.7). For any given stage, it is

unlikely that at the first iteration the peak efficiency operation is obtained at the mass flow rate and pressure ratio suggested by the ECPPS. Small modifications are therefore required. Constant blade re-stagger is first considered. On the basis of the knowledge acquired in Chapters 3 and 4, rotor and stator blades are re-staggered in order to shift the stage working line as necessary, while maintaining the incidence within acceptable values. DF and inlet Mach number profiles are extracted for each blade-row and the values at the reference radius are compared with the those predicted by the ECPPS. The achievement of a desired division of pressure rise between rotor and stator is further guided by spanwise predictions of DoR.

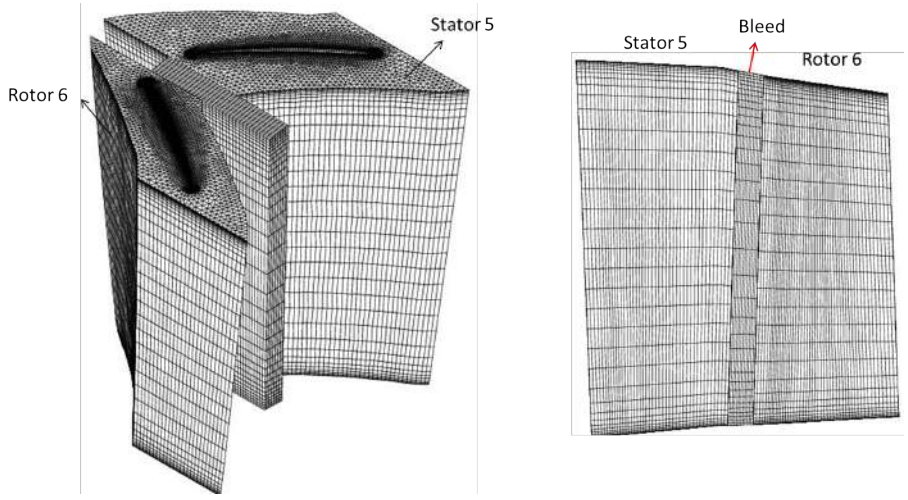

Figure 5.7: Three-dimensional and meridional views of mesh block used to simulate compressor inter-stage bleed

Subsequently, the individual stages are assembled and the whole compressor is simulated. The performance of a generic stage may slightly change mainly due to the initial guess of back-pressure boundary conditions. On the basis of the study illustrated in Chapter 4, if a better re-distribution of rotor loading is required across some adjacent stages the matching can be improved by stator re-staggering. The calculation of DF and DoR radial profiles might indicate the need for geometry modifications at the end-walls. An optimisation procedure with the objective of producing CD or PIV profiles based on stagger angle, solidity, camber angle and thickness distribution (maximum thickness and thickness-to-chord ratio) would be preferable. However, due to the high number of stages, this would require an expensive and time-consuming numerical effort. In addition, stagger angle, solidity

and camber angle are considered the most important variables for the overall performance, while other parameters become important only in blade regions where the flow has supersonic features [59]. For this type of machine, a relatively weak passage shock only occurs at the first rotor. Therefore the type of profiles are kept the same, recalling that the main purpose of this study is to generate a stable and efficient baseline design. Blade end-wall region modifications are applied where excessive high incidence is predicted, in order to enhance the local inflow condition. Generally the aim is to increase the inlet blade angle in order to cope with the reduced axial velocity due to the end-wall boundary layer [68]. Adjustments of the outlet blade angle and thus camber angle may be required if undesirable changes in flow turning are predicted. Another possibility is to positively re-stagger the blade towards the end-wall in order to locally reduce the incidence, in agreement with the study performed in Chapter 3. Blade pitch is fixed by the ECPPS, thus another option to further modify the local DF is to increase the chord length [54]. This would however result in a larger wetted area and profile losses. The use of blade sweep and dihedral angles at the end-walls represent the major techniques to improve end-wall flow performance at off-design condition. Thus, these will be taken into account after CFD solutions at off-design operation are analysed.

5.6 3D baseline compressor flow features

In this section the overall performance predicted from numerical simulations are compared with the predictions provided by the ECPPS. Flow features are illustrated in order to assess the aerodynamic design of the 3D compressor geometry. Figure 5.8 shows the compressor maps obtained by CFD calculations, where the surge line, choke line and anti-surge line predicted by the ECPPS are also illustrated. Comparing Figure 5.8 obtained from CFD simulations with Figure 5.2 obtained using the simulator, good agreement is found in terms of stability range at any given corrected mass flow. It is known that steady-state solutions do not predict compressor stall accurately and better predictions would be obtained by unsteady simulations. Nevertheless, for each load compressor map, CFD results provided a slightly higher maximum pressure (not shown in the figure). This, to some extent, is

reassuring considering that unsteady simulations would typically result in relatively lower stall margin.

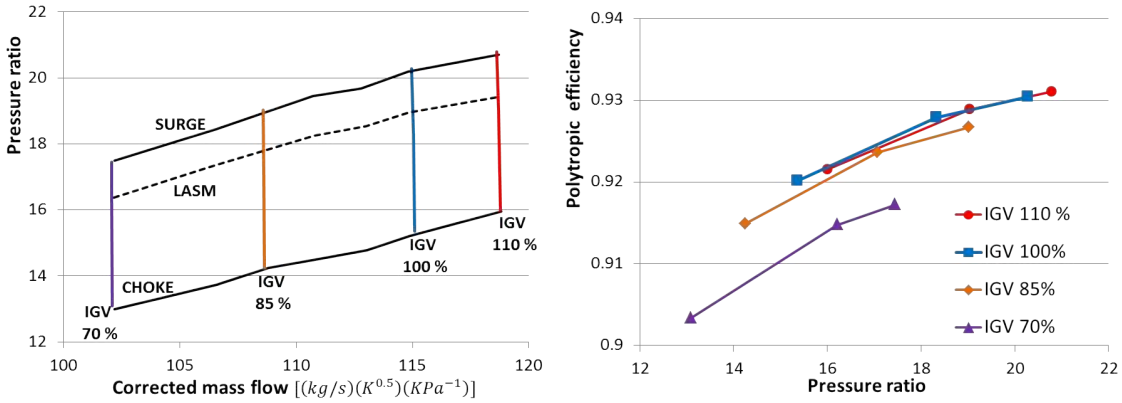

Figure 5.8: Compressor maps predicted using CFD

A nominal polytropic efficiency of 92.75% is calculated. This is in good agreement with the value of the Siemens SGT5-4000F compressor [91]. Furthermore the obtained efficiency matches the value established by the H2-IGCC project partners. Different factors should be considered to discuss the relatively high efficiency obtained without optimised flow distribution. First, in terms of overall performance, CFD prediction accuracy is generally within 2%. Moreover, in the current study, compressor flow leakages have not been taken into account. Nevertheless the overall performance of the 3D design show that a stable and efficient design has been achieved using educated modifications to the preliminary design. Details of the flow features at nominal condition are provided below.

Table 5.4 shows the values of stage pressure ratio, ψ, DF and inlet Mach number predicted by the ECPPS and CFD analysis. Furthermore, the isentropic efficiency (η_{is}) predicted using CFD is also shown. With the exception of the pressure ratio and efficiency, CFD results represent the spanwise average along the blade core (from 30% to 70% of the span) and good agreement is found with the ECPPS preliminary design values. The front and rear stages exhibits similar stage loading coefficients while, in comparison, lower values are calculated across the middle stages. In addition to the work input variation across the compressor stages, stage loading is significantly affected by the type of annulus geometry. In this case, the outer diameter slightly decreases from the front to the mid of the compressor. Towards the

Table 5.4: Stage performance predictions. Comparison between ECPPS (referred to as ES in the table) and CFD simulation results

Stage	Pressure ratio		ψ		DF_m (rotor)		DF_m (stator)		M_{in} (rotor)		M_{in} (stator)		η_{is}
-	ES	CFD	ES	CFD	ES	CFD	ES	CFD	ES	CFD	ES	CFD	CFD
1	1.395	1.394	0.31	0.325	0.398	0.391	0.417	0.406	0.876	0.854	0.704	0.686	0.934
2	1.346	1.346	0.284	0.297	0.373	0.370	0.416	0.412	0.783	0.785	0.648	0.634	0.935
3	1.305	1.306	0.260	0.280	0.365	0.363	0.427	0.419	0.753	0.758	0.618	0.608	0.932
4	1.271	1.291	0.268	0.276	0.405	0.407	0.477	0.465	0.732	0.718	0.591	0.600	0.926
5	1.22	1.261	0.258	0.264	0.415	0.406	0.445	0.449	0.692	0.683	0.552	0.569	0.913
6	1.206	1.210	0.21	0.238	0.337	0.361	0.419	0.432	0.645	0.645	0.552	0.545	0.896
7	1.201	1.202	0.226	0.247	0.379	0.379	0.378	0.362	0.633	0.636	0.514	0.525	0.908
8	1.189	1.185	0.232	0.247	0.396	0.392	0.425	0.399	0.597	0.593	0.521	0.536	0.903
9	1.167	1.164	0.226	0.250	0.387	0.384	0.398	0.401	0.573	0.560	0.501	0.534	0.907
10	1.153	1.155	0.229	0.261	0.387	0.402	0.427	0.459	0.553	0.540	0.487	0.520	0.901
11	1.153	1.154	0.250	0.281	0.411	0.417	0.429	0.419	0.538	0.540	0.475	0.482	0.912
12	1.149	1.150	0.264	0.291	0.423	0.433	0.431	0.452	0.525	0.522	0.464	0.479	0.920
13	1.142	1.144	0.273	0.311	0.420	0.433	0.382	0.413	0.513	0.513	0.458	0.467	0.922
14	1.136	1.139	0.282	0.317	0.405	0.432	0.459	0.473	0.506	0.500	0.446	0.456	0.911
15	1.132	1.134	0.299	0.339	0.429	0.452	0.568	0.591	0.483	0.478	0.426	0.434	0.908

rear stages, instead, it reduces more sharply (see Figure 5.1). Therefore, at the back of the compressor, the work input reduction with stage number is balanced by the lower mean blade velocity and in this case the stage loading is higher compared to the middle stages. Table 5.4 highlights that the flow undergoes high diffusion in the rear stages, especially across rotor blades. The increase of DF towards the back of the compressor might be explained considering the boundary layer thickening, reduction of blade length and local high stage loading. In order to improve the capability of rear stages to prevent early flow separation the aspect ratio is reduced [56]. The low diffusion and loading of the compressor middle stages may justify the use of standard NACA 4 ditigits.

Figure 5.9 shows the spanwise profiles of ψ, DF and DoR of the 2^{nd}, 6^{th} and 12^{th} stages. These are representative of the front (DCA), middle (NACA 4) and rear (NACA 65) stages respectively. Conventional stage loading coefficient ($\psi = 0.45$) are only exceeded along front stage hub regions. However, flow diffusion is well controlled due to the use of DCA profiles that are better than NACA profiles in terms of DF [59]. From the figure it can be also observed that since the flow is

subjected to a general higher diffusion in the rear stages, the DF is close to critical values at end-wall regions. As previously mentioned, subsonic rotor blades have higher capability in preventing flow separation than stators. Thus, for the selected pressure rise, the high value of DF across the rotors is required in order to avoid significant flow separation at stator hubs. Figure 5.9 suggests that for the type of machine under analysis and applied design the rear stages can be seen to be critical in terms of compressor stability.

Figure 5.10 shows stage 1 inlet Mach number radial profile and the flow field extracted at 95% span. The relative inlet flow matches the value indicated by the ECPPS at the reference section and the flow is slightly supersonic towards the tip ($M_{1,rel} = 1.08$ at 95%). Thus, in agreement with the theory, despite the sharp shape of the leading edge the shock is detached [27].

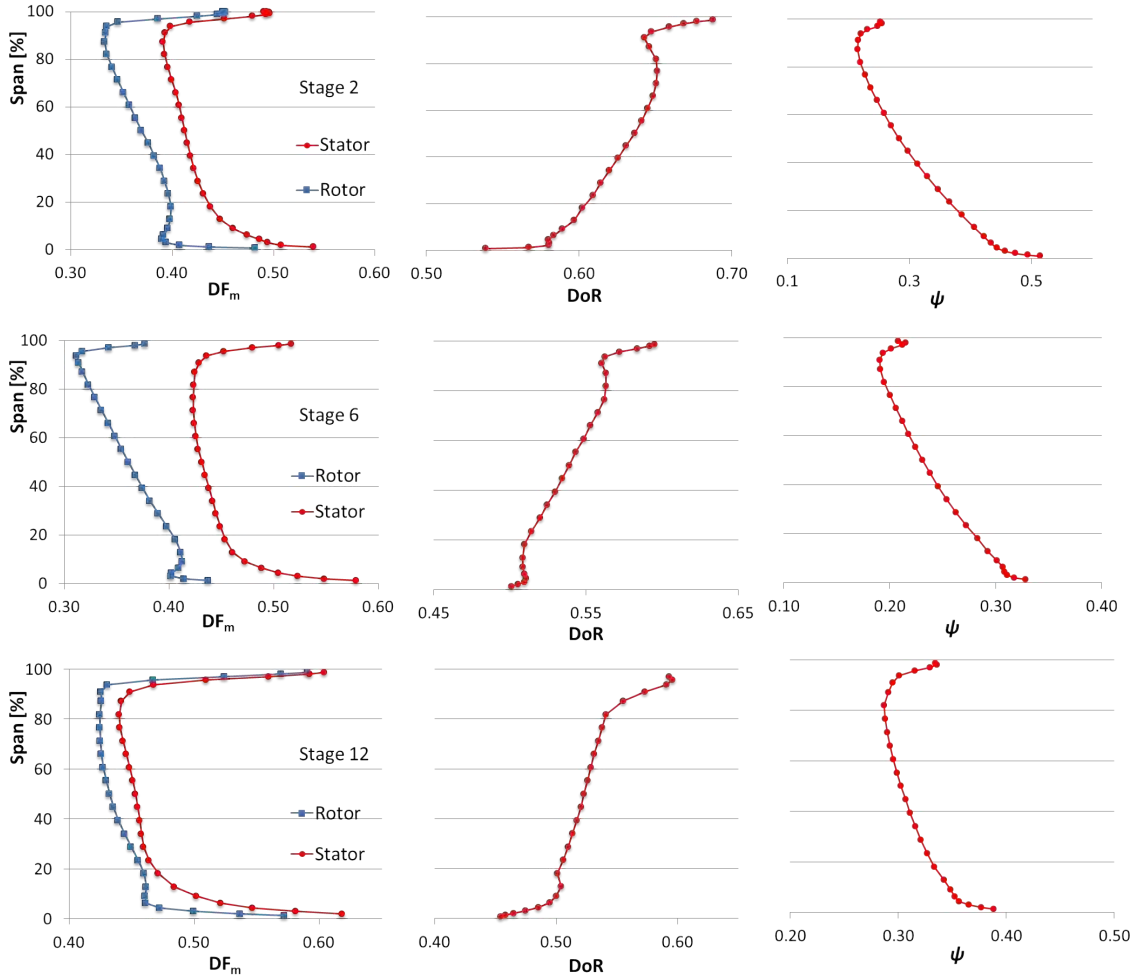

Figure 5.9: DF_m, DoR and ψ radial profiles

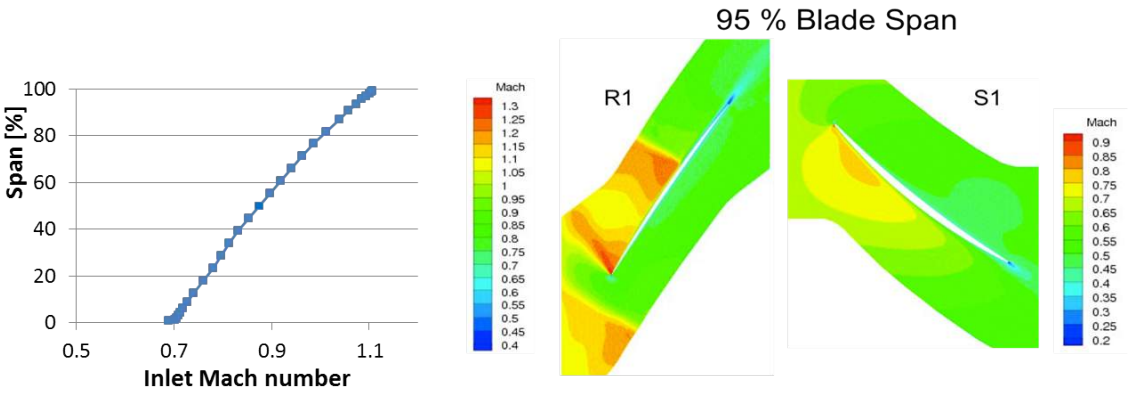

Figure 5.10: Stage 1 inlet Mach number profile and Mach contours at 95% span.

Figure 5.12 shows the near-wall Mach number contours before numerical stall occurs and both meridional views are illustrated. In the case of axial compressors with high number of stages, the literature suggests that compressor surge is caused by stalling of the rear stages, which can be explained as follows [12]. When the operating points moves from design condition towards the surge line, the flow density at exit of the compressor increases due to the increase in delivery pressure. On the other hand the mass flow rate typically slightly reduces. Both effects lead to a reduction of axial velocity and higher blade incidence towards the back of the compressor that becomes critical at the end-walls. Although in this case the pressure ratio maps are nearly vertical, similar effects occur at the downstream stages since the (choked) mass flow is controlled by the front stages. For instance, Figure 5.11 shows the inlet axial velocity variation for stage 2 and stage 12 when the operating point moves towards the surge line. The above discussion founds also agreement in Figure 5.12, where the large flow separations along the rear stages stator suction sides are further justified by the high loading predicted at design condition. Smaller boundary layer separations are observed near stator tip regions and along rotor suction sides, with the exception of stator 10 and rotor 15. Although further investigations are required, one reason of stator 10 tip flow separation might be discussed considering the relatively large amount of air flow rate extraction occurring along the casing between stages 9 and 10 and the methodology used to simulate the bleeds. Inter-stage air bleeding can be also seen as aspiration of low energy viscous flow at the annulus wall reducing the low flow blockage and leading edge loading at the downstream rotor tip. To some extent, it may be expected that when the back

pressure is increased from a working point, the air extraction slightly increases and rotor tip loading may not increase. For a required stage pressure rise, this probably causes an overloading of the downstream stator tip region at near-stall operation.

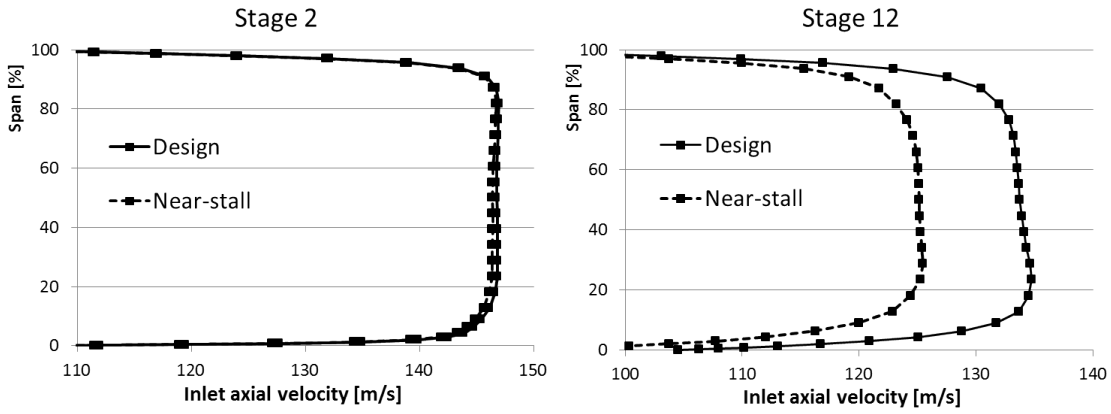

Figure 5.11: Effect of back pressure increase on stage inlet axial velocity

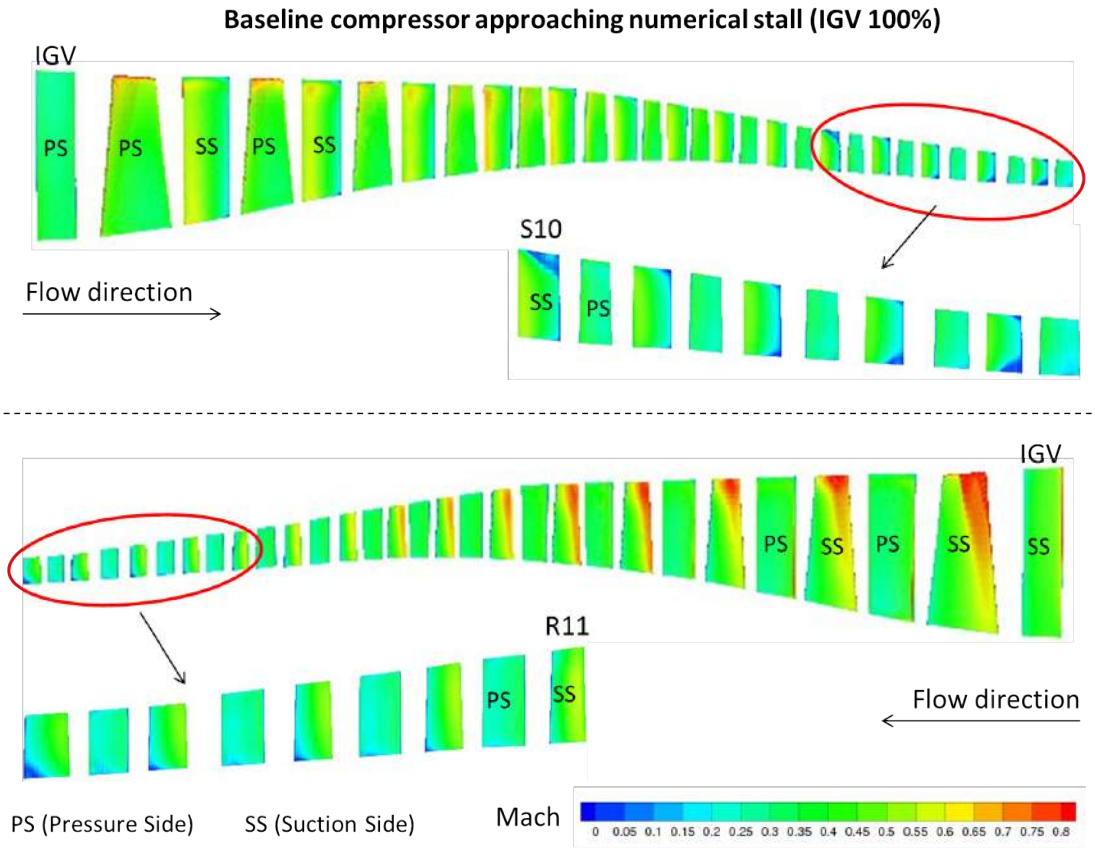

Figure 5.12: Baseline compressor meridional views. The near-wall Mach number contours refer to near-stall operation

To further discuss this, Figure 5.13 shows the DF radial profiles for stages 10 and 14 extracted at design condition. By inspection of such plots, together with Figure 5.9, it can be observed that the H2-IGCC compressor stages located downstream of air extractions (stage 6, 10, and 14) exhibit a more marked increase in DF difference between rotor and stator towards the tip. This might represent the physical effect of inter-stage casing bleeding. In other technology systems, part of the air can be bled from rotor and stator suction surfaces using suction slots distributed along the span. In addition to a more uniform air extraction, this may allow to aspirate the low energy viscous flow from diffusion-limiting locations on both blades and flow path surfaces [33]. Therefore, it may be interesting to investigate if the use of different bleeding mechanisms would improve the aerodynamic behaviour of the mentioned stages at off-design operation. Finally, as it will be illustrated in the following chapter, the large flow separation detected at rotor 15 hub region could be mainly considered a consequence of the trailing edge boundary layer detachment occurring at the upstream stator.

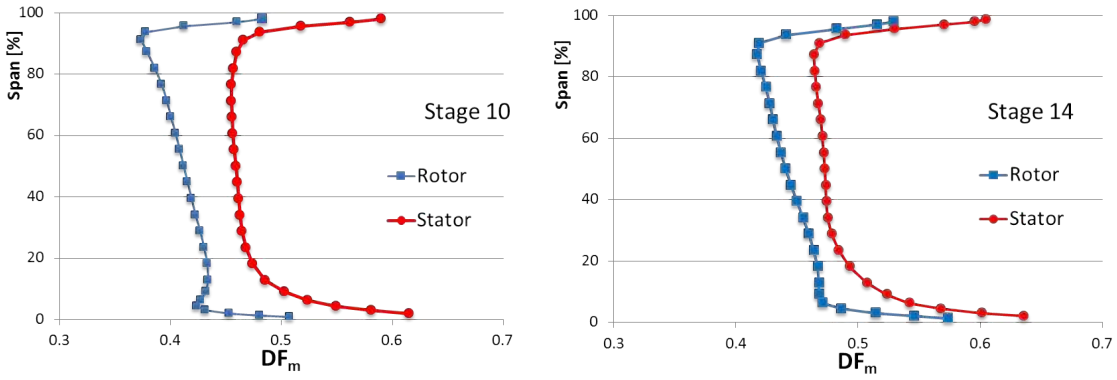

Figure 5.13: DF_m radial profiles for stages 10 and 14

5.7 Summary

The design of a conventional F class gas turbine was conducted in collaboration with other project partners by following a typical turbomachinery design. Starting from the through flow model analysis, the aim and contribution of the current work was to generate the 3D blade geometry for the 15 stage compressor that would allow the machine to achieve the required performance. This chapter described the

procedure adopted in this study in order to achieve such a goal. This involved the use of analytical tools available in the literature, known features of modern heavy-duty gas turbines and realistic assumptions based on compressor aerodynamics and design theory. The 3D blade design and stage matching was refined through steady state CFD analysis using the knowledge acquired in Chapters 3 and 4. The expected performance was obtained and stability requirements verified. Blade shape optimisation was not performed, the purpose being the generation of an efficient and stable geometry to be used as baseline. Key features of the three-dimensional flow were illustrated in order to assess the reliability of the produced design from an aerodynamic point of view. Thus, to some extent, the work discussed in this chapter contributes to the literature by presenting the methodology used, a subject that is not typically covered in this form.

Chapter 6

H2-IGCC compressor re-design for syngas operation

6.1 Introduction

In this chapter, the baseline compressor geometry presented in Chapter 5 is modified in order to accommodate specific H2-rich syngas combustion. The main purpose is to re-establish the original compressor surge margin for the new nominal mass flow rate and provide acceptable part-load operation. An additional requirement is to maintain the performance similar to those of the baseline machine. Keeping the reference TIT, the re-staggering of the front stator vanes is first considered in order to modulate the compressor air flow and maintain the original turbine inlet volumetric flow unchanged. Similarly to the generation of the baseline geometry discussed in the previous chapter, the ECPPS is first used to determine the new mean line compressor configuration that would guarantee stable and safe operation for the gas turbine when burning the new fuel. The aim of the present work is to use the stagger angle changes predicted by the ECPPS as guidance for re-designing the 3D geometry and perform CFD simulations. Inspection of the the flow features obtained from CFD allows to identify and propose additional compressor modifications in order to further improve the fuel-flexibility of the gas turbine.

6.2 Effect of H2-rich syngas combustion on the baseline gas turbine

In agreement with H2-IGCC project partners, a particular H2-rich syngas fuel has been selected. The composition of the fuel after acid gas removal and CO_2 absorption are reported in Table 6.1, resulting in a LHV of about 33.4 MJ/kg. According to the project objectives and constraints, the possibility of burning undiluted fuel is considered and zero integration between the gasifier block and power block is assumed (ID=0). As discussed in the first chapter, an undiluted H2-rich combustion, with technology still under development, might result in a relatively small compressor surge margin reduction even at low ID. This would reduce the complexity and cost of the system integration. The ECPPS has been used to investigate the fuel-flexibility behaviour of the machine when burning the selected fuel at the reference TIT [18].

Table 6.1: H2-rich syngas fuel properties

% component	molar fraction [%]
H_2	85.88
CO	1.17
H_2O	0.04
CO_2	3.95
N_2	8.95

Figure 6.1 shows that at nominal condition (TIT=1440°C and IGV 100% opening) the working point is moved towards the surge line. Thus, as expected, the large volumetric fuel flow rate required to keep the original TIT leads to an increase of the expander inlet pressure and compressor stability deterioration. The pressure ratio rises to 18.7 and the stall margin is reduced by about 20% of its original value. More importantly, while the new nominal condition may be still considered acceptable (the point is situated below the LASM line), it can be observed that adopting the constant TIT and IGV only control at part-load operation would result

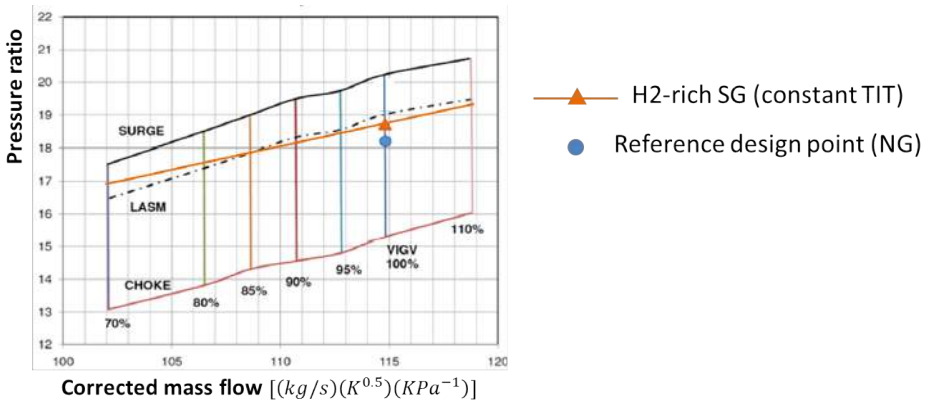

Figure 6.1: Pressure ratio maps for the baseline compressor geometry predicted by the ECPPS

in a maximum allowable air flow modulation range of about 5.5% (corresponding to the IGV 85% closing operation). This would be not tolerable considering the high importance of a relatively wide power load range. In particular, compressor flow reduction for conventional combined cycles is typically within 10-15% when the IGV is the only variable vane [22].

6.3 Re-designed compressor configuration

An adaption of the ECPPS has been developed to propose a new mean-line compressor design [88, 18]. The expander inlet volumetric flow and TIT of the original design have been fixed and a reduction of about 2.5% of the original compressor inlet mass flow has been predicted. This takes into account that, without any modifications to the cooling system technology, the compressor bleeds slightly vary due to small changes in pressure along the compressor casing. According to empirical data available from similar machines, the re-staggering of the compressor front four stator guide vanes is considered. Re-staggering the vane-rows does not include any modification of blade and vane profiles. Using the ECPPS, the stagger angle of the first four stator blade-rows have been left free to move at the new nominal compressor inlet mass flow rate, while the IGV is kept at its original position. The ECPPS optimisation includes part-load operation obtained with constant TIT and IGV only control. The process is iterative since, once the compressor is re-designed, it needs to be tested and matched using the ECPPS in order to verify the overall

machine behaviour.

Figure 6.2 shows the predicted compressor pressure ratio maps for the new geometry. Table 6.2 summarises the comparison of the main gas turbine parameter and performance between the baseline and re-staggered machines. The new nominal compressor/expander matching occurs for a pressure ratio slightly higher than the original value, and the reference surge margin is re-established. Moreover, the results indicate that the new configuration would allow for stable and safe part-load operation up to IGV 70% closing, corresponding to an airflow modulation of about 11.5%. It is important here to highlight that a fast adaption of the compressor to the two different combustion operations at full and part-load would be possible only assuming an IGV mechanical actuator independent of that of the front stators. The power required to drive the compressor (W_C) slightly reduces mainly due to the lower compressor inlet air flow rate ($\dot{m}_{a,in}$). The turbine inlet mass flow rate ($\dot{m}_{g,in}$) also reduces since the increase in fuel flow rate ($\dot{m}_f$) is lower than compressor air delivery reduction ($\dot{m}_{a,out}$). Recalling that the turbine inlet volumetric flow rate has been fixed, the reduction in $\dot{m}_{g,in}$ can be seen also as a consequence of the lower density of undiluted H2-rich syngas combustion exhaust products. However, the slight increase in pressure ratio and higher specific heat of the expander inlet gas lead to a greater turbine enthalpy drop. The result is an increase of the original turbine net power output of about 7%. Such variation can be considered relatively small, particularly if compared to those predicted by other studies when taking into account different gas turbine geometry modifications [7, 29]. As a result of the slightly higher pressure ratio, a small reduction of the TET (of about 8°C) has been calculated which, in addition to the lower turbine outlet mass flow rate ($\dot{m}_{g,out}$), suggests a slight decrease of the steam turbine power. However, these variations can be considered as well very small so that the original bottoming steam cycle performance is substantially preserved. The turbine blade metal temperature variations calculated by the simulator do not exceed 5°C in comparison with the reference design condition and therefore no important modifications of the cooling system may be required [88]. These changes in blade temperatures are mainly due to the different combustion exhaust heat transfer properties, since the turbine inlet mass flow is slightly lower and the baseline cycle pressure ratio has not changed considerably,

recalling that these parameters play a key role in determining the effectiveness of an existing cooling scheme at off-design condition.

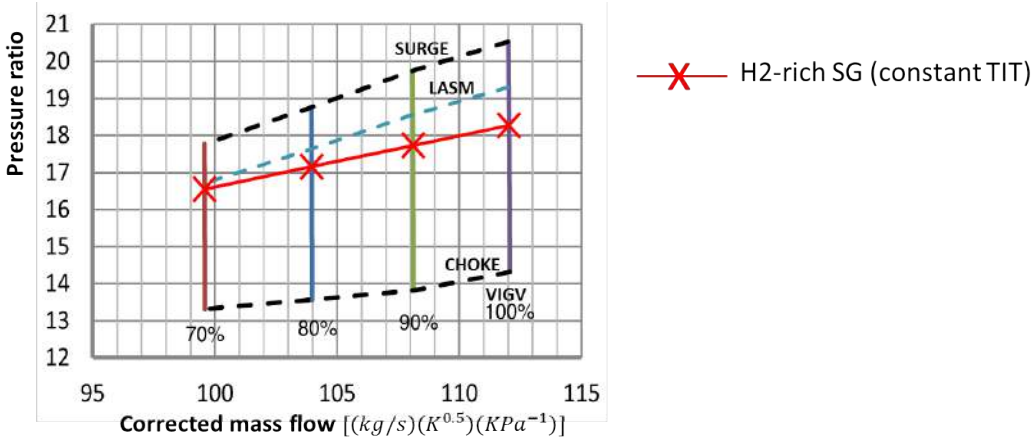

Figure 6.2: Pressure ratio maps for the re-staggered geometry predicted by the ECPPS

Table 6.2: Comparison between baseline (natural gas) and modified (H2-rich syngas) gas turbines

	Baseline	Re-staggered
$\dot{m}_{a,in}$ (kg/s)	685.4	668.8
$\dot{m}_{a,out}$ (kg/s)	508.4	496.6
W_C (MW)	262.9	256.9
Pressure ratio (-)	18.2	18.27
$\dot{m}_f$ (kg/s)	15.0	23.5
TIT (°C)	1440	1440
$\dot{m}_{g,in}$ (kg/s)	523.15	515.8
TET (°C)	578.2	570.1
W_{GT} (MW)	299.6	321.1

The task and contribution of the current work is to asses by means CFD analyses the effectiveness of the new compressor configuration proposed by the ECPPS. Furthermore, the 3D flow features analysis may suggest additional geometry modifications to be applied in order to further improve the machine off-design operation. The grid resolution and boundary conditions are the same as those described in

Table 6.3: Stagger angle variations. Comparison between ECPPS and CFD

Stator No.	$\Delta\zeta$ (ECPPS)	$\Delta\zeta$ (CFD)	$\Delta\zeta/\Delta\zeta_{stator1}$
1	1.2	3.8	1.0
2	1.1	3.48	0.917
3	1.0	3.17	0.834
4	0.5	1.58	0.416

Chapter 5. It was first observed that applying the stagger angle variations indicated by the ECPPS would not allow to shift the working line as required and larger stator blade stagger modifications were needed. As reported in Table 6.3, it was decided to keep the same stagger angle variation ratios (intended as the ratio between a given stator stagger angle variation and the first stator stagger angle variation, i.e. $\Delta\zeta/\Delta\zeta_{stator1}$) indicated by the ECPPS. The discrepancy observed between the second and third columns in Table 6.3 highlights the importance of using CFD when proposing a "new" design. However such discrepancy might be in part due to the selected 3D analytical tool used to generate the baseline compressor geometry. Figure 6.3 shows the compressor maps obtained by CFD simulations. The results match well with the ECPPS predictions illustrated in Figure 6.2, although different stagger angle modifications have been used. The efficiency calculated for the new working point of the re-staggered compressor is equal to that of the baseline geometry design point. Furthermore, comparing Figures 5.8 and 6.3 it can be observed that the efficiency variation of the re-staggered machine at part-load operation is similar to that one predicted for the baseline geometry. This is an important result, which suggests that by providing an appropriate flow matching at the front of the compressor allows keeping the original performance also at part-load.

The flow field obtained using CFD simulations has been analysed along the running and surge lines. Table 6.4 shows the stage performance variations along the working line. First of all it is interesting to observe that, similarly to the study presented in Chapter 4, when comparing Tables 6.4 and 5.4 a reduction in pressure

ratio is predicted for the stages where a variable stator is used, with the exception of the first one. The required pressure ratio is however achieved through a small overloading of the middle and rear stages compared to the baseline geometry. As expected, the drop in efficiency predicted in Figure 6.3 (and Figure 5.8) is mainly due to the large reduction in performance of the first stage. In particular, at IGV 70% closing condition a significant drop in stage 1 efficiency occurs towards the hub (see Figure 6.4). This can be attributed to a large reduction of the first rotor inflow angle along the inner part of the blade when the IGV is largely closed, in agreement with the discussion provided in Chapter 4. High friction losses are also expected across the IGV blade passage.

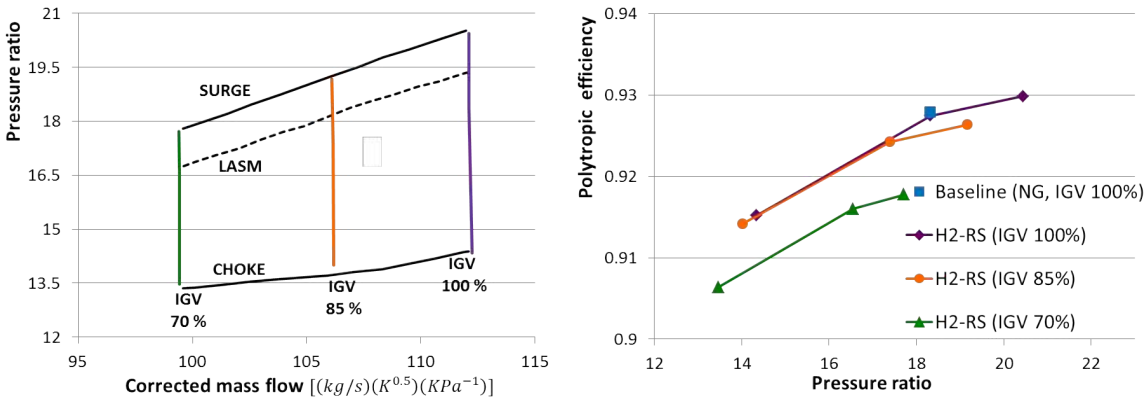

Figure 6.3: Re-staggered geometry compressor maps for H2-rich syngas combustion obtained with CFD simulations

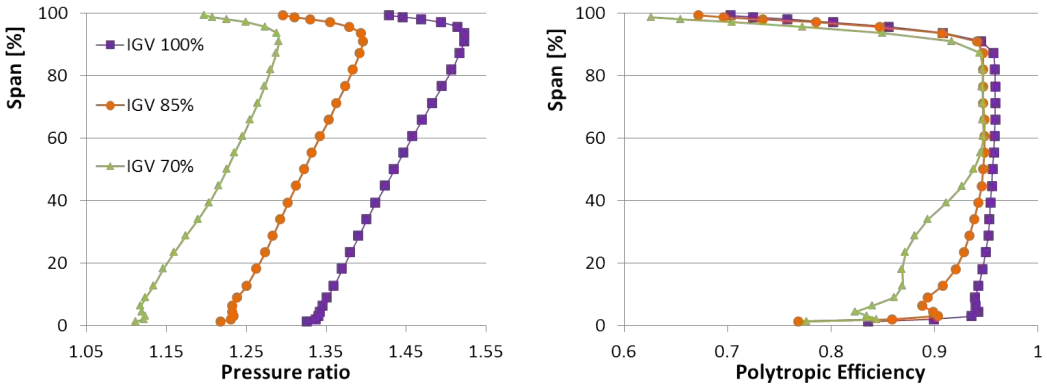

Figure 6.4: Part-load (IGV closing) stage 1 performance drop along the running line

Table 6.4: Stage performance variations at part-load operation

Stage	IGV 100%		IGV 85%		IGV 70%	
-	PR	η_{is}(%)	ΔPR(%)	$\Delta\eta_{is}$(%)	ΔPR(%)	$\Delta\eta_{is}$(%)
1	1.445	0.936	-8.06	-1.42	-16.09	-8.33
2	1.319	0.934	-0.01	-0.14	-0.19	-0.88
3	1.281	0.928	-0.05	-0.27	-0.16	-1.26
4	1.255	0.925	-0.01	-0.12	0.11	-0.83
5	1.215	0.910	0.01	-0.14	0.13	-0.74
6	1.201	0.900	-0.01	-0.31	0.08	-0.88
7	1.203	0.908	0.11	-0.28	0.30	-0.68
8	1.192	0.902	0.12	-0.25	0.32	-0.57
9	1.175	0.908	0.10	-0.35	0.30	-0.67
10	1.165	0.904	0.25	-0.22	0.64	-0.36
11	1.161	0.914	0.40	-0.10	0.94	-0.11
12	1.159	0.922	0.47	-0.05	1.10	-0.05
13	1.157	0.924	0.50	-0.03	1.11	-0.05
14	1.161	0.920	0.66	0.06	1.21	0.07
15	1.152	0.912	0.70	-0.02	1.27	-0.04

Figures 6.5 and 6.6 show the meridional views of the near-wall Mach number contours at near-stall condition for both IGV 100% and IGV 70% closing operation. The steady-state simulations suggest that, as for the reference machine, the modified compressor geometry is mainly trigged to stall by the rear stages. This seems to be true also for the lowest load condition, despite the discussed flow mismatching across the first stage consequent of the large IGV closure. In particular, towards the hub the first rotor is subjected to flow separation along the pressure side due to high negative incidence. As a consequence, bad axial matching is also found along the inner blade region of the downstream stator. The figure also shows a clear flow separation along the suction side tip region of the IGV, which can be explained as follows. At nominal condition the velocity diagram radial distribution at the inlet of rotor 1 is characterised by an increase of both relative and absolute angles due to the increase in tangential velocity from hub to tip and according to Equation 5.5.

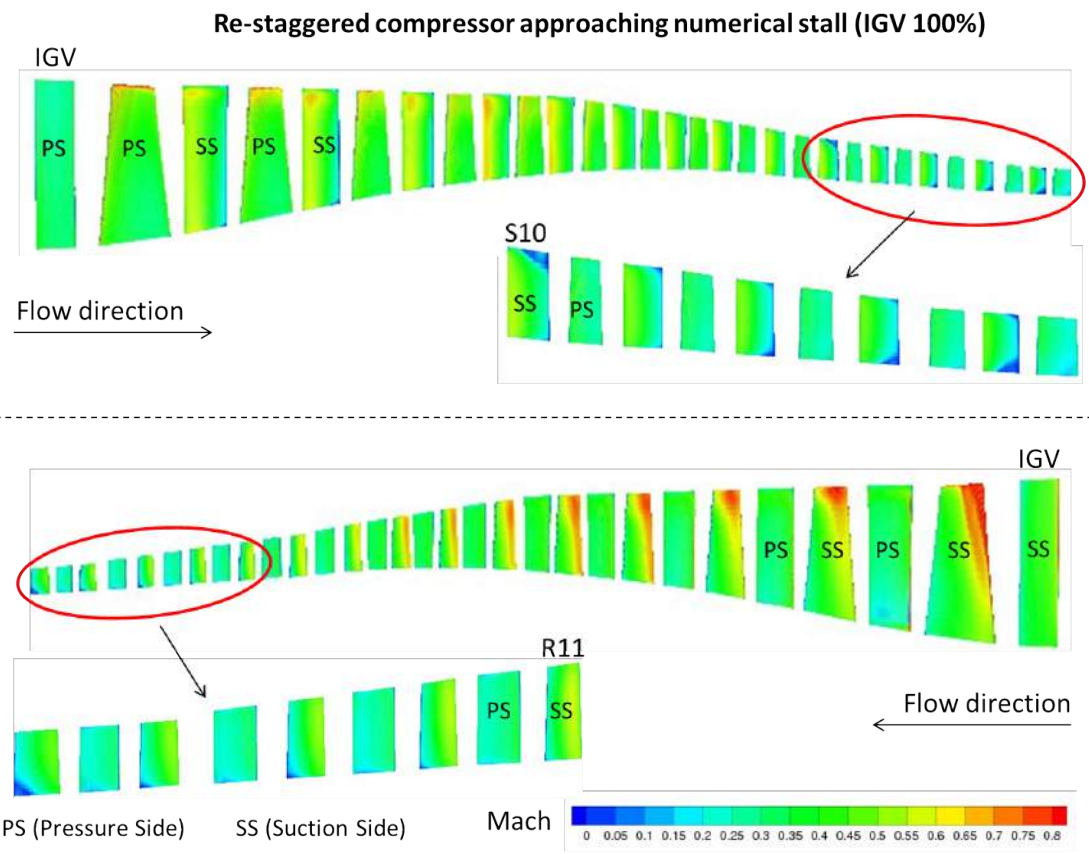

Figure 6.5: Re-staggered compressor meridional views. The near-wall Mach number contours refer to near-stall operation and IGV 100%

In order to provide the required velocity triangle along the span, the IGV stagger angle needed to be increased towards the casing considering the low hub-to-tip ratio of rotor 1. Therefore, due to the large constant IGV re-stagger modification applied at part-load operation, along the outer part of the blade the IGV inlet flow is characterised by very high incidence and separates downstream the leading edge (see Figure 6.7). Nevertheless, it is believed that in this case the severe flow separation at the back of the compressor may have major influence on compressor stall. Therefore, enhancements to the surge margin could be achieved by introducing sweep and/or dihedral angles at the rear stage stator end-walls. In particular, on the basis of the study performed in Chpater 4, blade true sweep is applied. The radial stacking line of the last 5 stators have been modified observing the related DF spanwise profiles extracted at near-stall condition. As an example, Figure 6.8 shows the applied sweep and consequent enhancement in terms of diffusion achieved for stator 10 and stator 14. The results refer to the IGV 100% opening and near-stall condition.

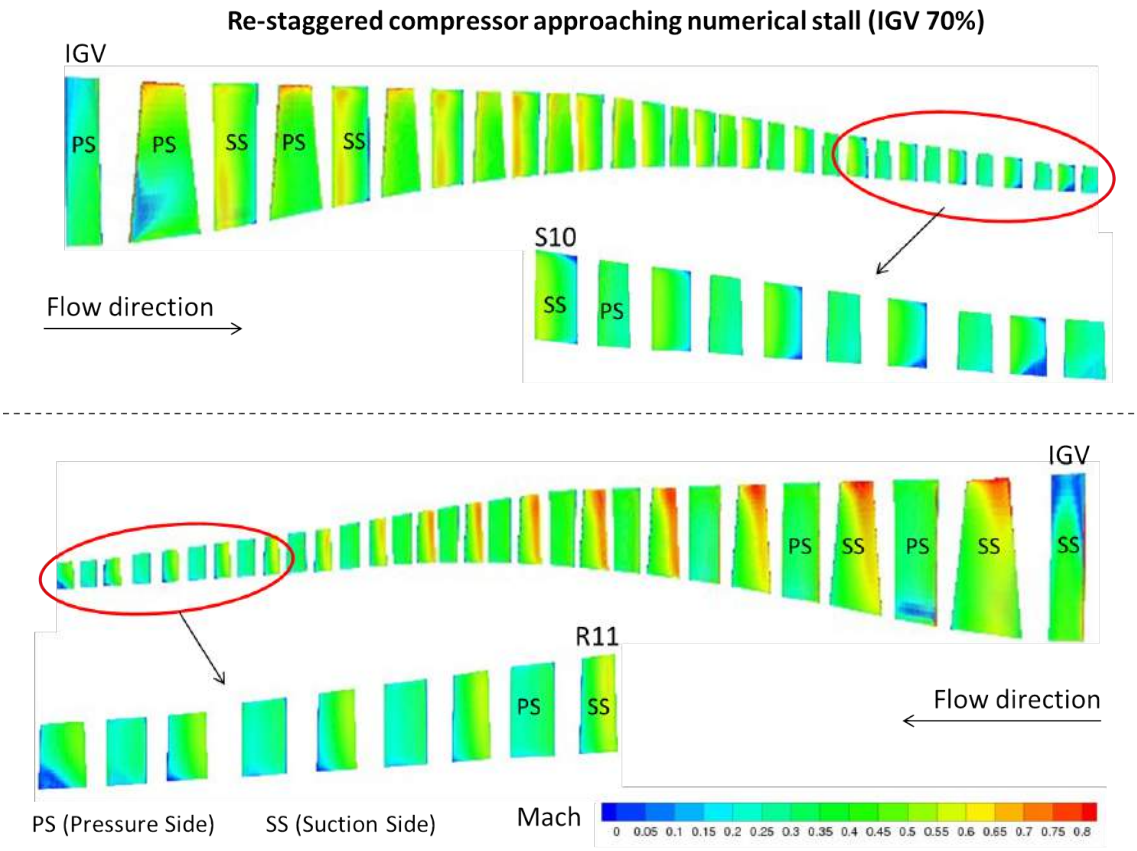

Figure 6.6: Re-staggered compressor meridional views. The near-wall Mach number contours refer to near-stall operation and IGV 70%

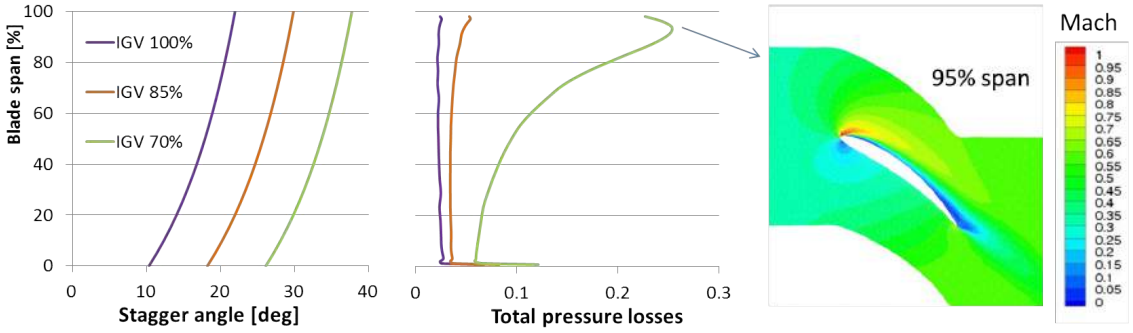

Figure 6.7: IGV profile losses during part-load operation at near-stall condition

Improvements are also obtained at part-load operation, resulting in an extended surge margin as shown in Figure 6.9. For completeness, Figure 6.10 indicates that having decreased the separated flow region along stator 14 suction side improves the inflow condition at the downstream rotor and reduces the trailing edge boundary layer separation. Overall, the consequent increase in maximum pressure during

power control may allow to extend the stable air flow modulation range. This means that a hypothetical fuel only control range, which provides lower combined cycle performance, could be reduced.

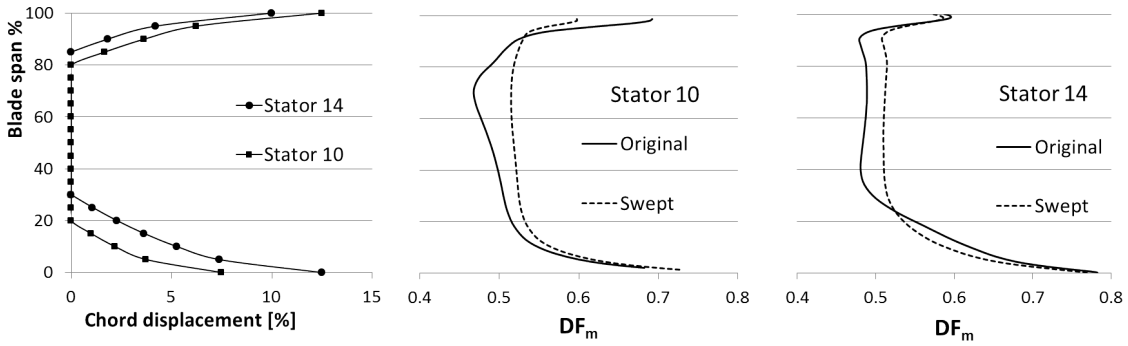

Figure 6.8: Applied sweep and related end-wall diffusion improvements for stator 10 and stator 14

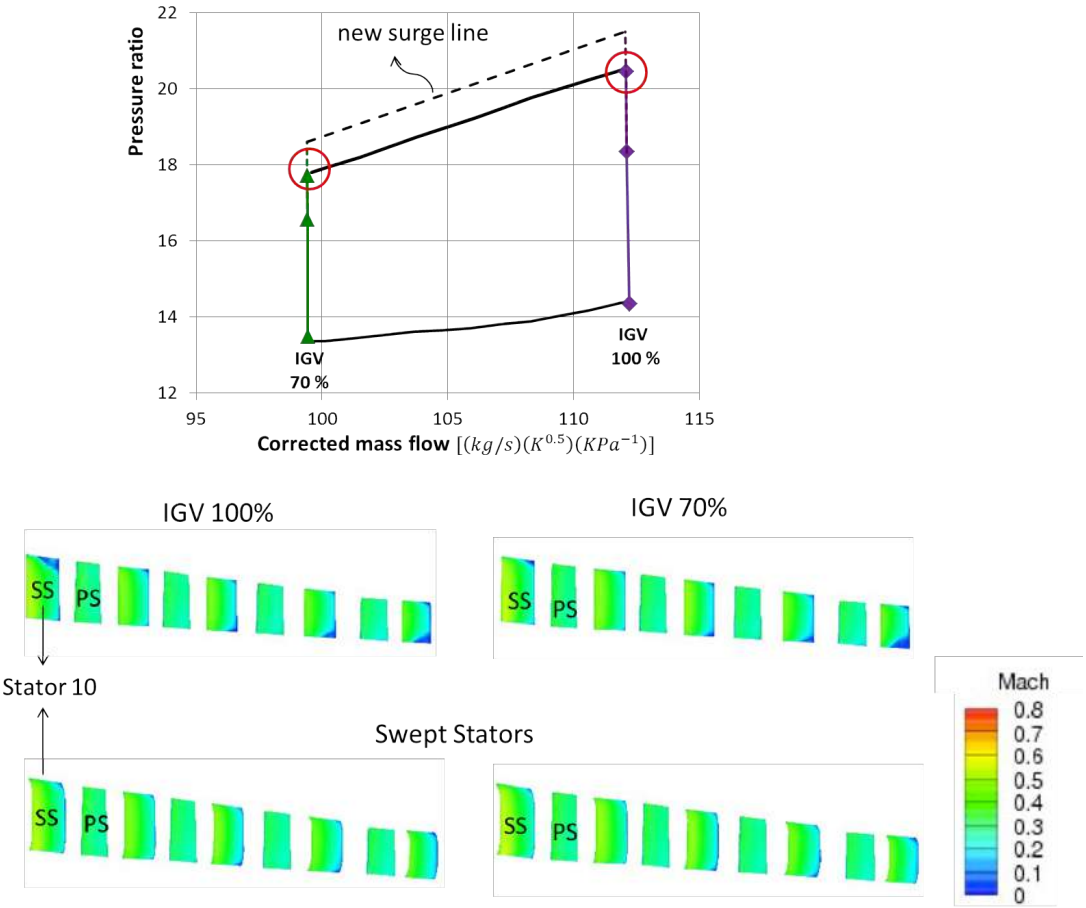

Figure 6.9: Surge margin improvement using stator blade sweep in the rear stages

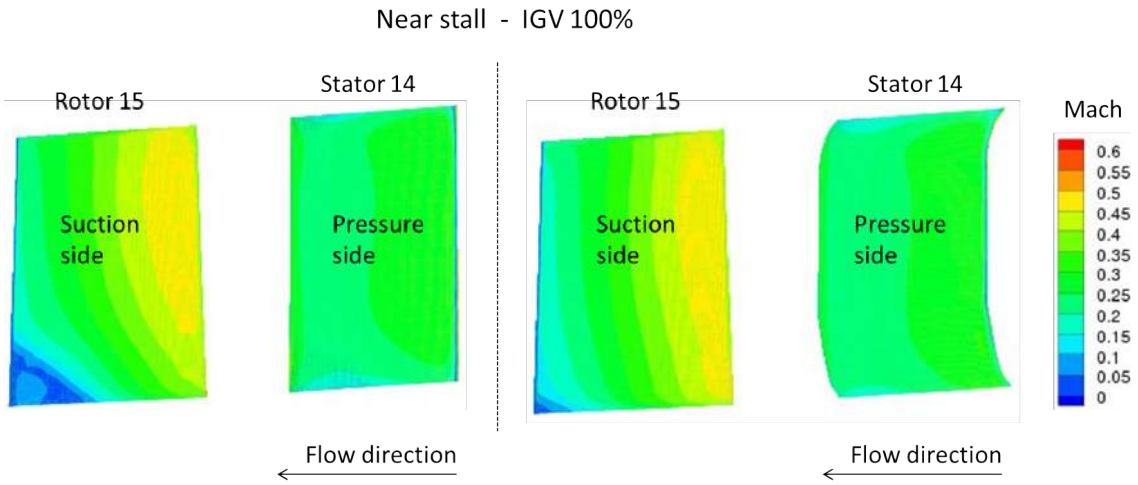

Figure 6.10: Rotor 15 boundary layer reattachment

Before concluding the chapter the following aspects should be highlighted:

- Assuming an IGV mechanical actuator independent of the one of the stator vanes, the proposed solution would allow for a fast and efficient adaptation of the compressor to the two different types of fuels. The original gas turbine cycle key parameters (pressure ratio and TIT) as well as combined cycle performance could be maintained without other major modifications.

- If the flexibility to switch back to natural gas operation is not a requirement, the re-designed compressor configuration could be improved considering rotor re-staggering and possibly introducing rotor sweep. Better flow matching would be achieved and higher local efficiency would be expected compared to the baseline geometry. However the enhancement of flow features at the front of the compressor may not result in higher overall performance, which seems to be determined by the middle and rear stages.

- Regardless of the type of combustion, the compressor part-load efficiency degradation represents a key aspect since it significantly affects the overall combined cycle performance [24]. Recalling that heavy-duty gas turbines operate at part-load for a large amount of their lifetime, compressor designers aim to produce 3D geometries that would allow for relatively high efficiency during power control at the expense of design condition performance. This may

involve a (non optimum) re-matching of the front stages at nominal condition, which are critical at off-design operation. This is further supported by the fact that the front stages of heavy-duty industrial gas turbines typically exhibit very high design efficiency, as observed in this work. This strategy however was not taken into account during the procedure illustrated in Chapter 5, which focused on flow matching at the working point.

6.4 Summary

The option of reducing the original compressor air delivery in order to cope with stability deterioration during H2-rich syngas operation has been discussed. Based on the results obtained using the through-flow model, this study addressed the 3D geometry modifications assisted by CFD. The re-staggering of the compressor front stator vanes was first applied in order to achieve the required shifting of the nominal working line towards the predicted lower mass flow range. The stability features during power control indicated by the mean-line analysis were verified. The importance of using CFD when proposing a "new" design as well as the benefits of reducing secondary losses were highlighted. In particular the use of sweep (or bowed) stators in the rear stages may be considered a very useful tool for the suggested solution. This would contribute to ensure an acceptable stable airflow modulation range for the new fuel combustion. Compared to other solutions suggested in the literature, a main motivation for the presented approach is found in the expected reduction of the modifications needed for the cooling scheme and bottoming cycle, while maintaining the machine class level. Furthermore, stator re-stagger and sweep are not believed to affect the structural integrity of the gas turbine significantly.

Chapter 7

Conclusions and recommendations

7.1 Conclusions

This section outlines the main conclusions drawn from the previous chapters. The limitations of the approach adopted for the investigations are also evaluated. For clarity, the thesis objectives listed in Section 1.2 are reported here:

1. To acquire a fundamental understanding of the impact of burning syngas on conventional industrial gas turbine operation and select appropriate compressor stability improvement techniques for the purposes of the current study.

2. To explore the selected techniques and propose suitable solutions to be applied to heavy-duty gas turbine compressors in order to cope with syngas combustion and fuel flexibility. Advantages and drawbacks of the investigated solutions compared to other possible gas turbine or cycle design modifications will be also discussed.

A fundamental understanding of the impact of syngas combustion on gas turbine operation was achieved via an extensive literature review. The participation to the H2-IGCC project allowed to gain further knowledge on the major integration factors that influence IGCC power plant performance and performance variation when considering different gas turbine modification strategies. This research however focused on the re-design of a conventional machine axial compressor. In particular, based

on the large number of available studies on compressor stability enhancement techniques, it was decided to explore the use of blade radial stacking line changes and VSVs methods within the IGCC development technology scenario. In collaboration with one project partner, a particular compressor re-design option for the H2-IGCC project was investigated and the expected main advantages compared to other modifications highlighted. The proposed solution is based on the concept of air flow modulation for conventional gas turbine part-load operation. The basic idea is to reduce the compressor air delivery in order to accommodate the higher fuel flow rate, while keeping the pressure ratio and TIT of the original thermodynamic cycle.

The following subsections elaborate further on the results obtained in this thesis.

7.1.1 Blade radial stacking line modifications

Effects of blade stagger, sweep and lean on NASA Rotor 37 performance were described in Chapter 3. The aim was to explore blade geometry modifications for the front transonic stages of heavy-duty gas turbines. Blade stagger was first analysed in order to investigate the shifting of the stage working line towards lower mass flow rates. Re-staggering from nominal condition typically involve a reduction of stage surge margin. It was found that, wherever rotor tip regions are critical, major improvements are obtained by applying forward true sweep since it significantly reduces the leading edge loading and effects of shock interaction with both tip leakage vortex and trailing edge boundary layer. In addition, a reduction of the radial flow migration and boundary layer accumulation towards the casing is possible. Although positive lean provides similar benefits, it leads to a lower radial pressure gradient on the blade suction surface enhancing the spanwise outward flow. Blade lean introduces additional radial forces so that its application in highly loaded blade may not be considered as a primary solution. As indicated in this study, however, it is expected that in industrial gas turbines the compressor front stages operate under conventional loading condition and stall mainly arises from flow separation along the end-wall regions of the rear subsonic stage stators. Therefore, in Chapter 4 blade true sweep was analysed in the last stage of the IDAC compressor. The study suggested that considerable benefits in flow stability can be obtained at hub regions, which are typically subjected to higher aerodynamic loading compared to

tip sections. Enhancements are mainly obtained by reducing the adverse pressure gradient on the suction side at the front of hub sections. For a given swept configuration, improvements are achieved at different flow coefficient operating conditions, an important feature for the current research.

7.1.2 Variable stator vanes and part-load operation

Based on the concepts of part-load VSVs methods for conventional machines, in Chapter 4 the re-staggering of the IDAC guide vanes was investigated. The aim was to produce a new geometry in order to allow the compressor to operate efficiently at a lower mass flow range estimated as a result of a hypothetical syngas combustion and fixing the reference TIT and turbine inlet mass flow rate. Closing the IGV represents the main tool to reduce the air flow rate but it may also cause significant drop in performance. In addition to the high IGV pressure losses, it was found that other major losses arise from the large reduction of the incidence angle towards the hub of the first rotor and consequent bad axial matching of the flow across the first stage. At the required lower mass flow rate, performance and surge margin improvements can be obtained by re-staggering the stator vanes and reducing the IGV closure. In particular, it was demonstrated that even applying constant stator blade re-stagger the original spanwise distribution of the first rotor inflow angle could be re-established. Although a VSVs optimisation procedure may lead to the required matching of the flow at the inlet of the rotors, it was emphasised that a reduction in compressor pressure ratio is likely to occur due to the lower pressure rise across the stators. Nevertheless, the application of blade sweep in the overloaded region of the multi-stage compressor provided a further increase of the overall maximum pressure rise and mass flow range. This allowed to re-adjust the stagger angle setting of the stators leading to a re-designed compressor with values of pressure ratio, efficiency and surge margin similar to the ones of the baseline geometry.

The positive impact of combing blade re-stagger and sweep for IGCC gas turbines was finally demonstrated in Chapter 6. Stator vanes re-staggering in the front stages and blade sweep in the rear stages were applied in order to cope with air supply control and critical flow separation regions respectively. The new compressor configuration would guarantee safe operation at nominal condition and relatively

wide stable part-load range, the latter predicted assuming the constant TIT and IGV only control. Power control strategies are discussed in the literature but detailed analysis in terms of the corresponding 3D compressor flow features are rarely included. In this study the blade regions responsible of the performance drop at part-load were highlighted but no attempt was made in order to improve the flow features.

Finally, the possibility of reducing the number of adaptations for the cooling system and bottoming cycle represents a considerable advantage when compared to other gas turbine modifications discussed in the literature. It was therefore concluded that the proposed solution can be considered a viable option to satisfy some important technical and economical constraints imposed by the integration of an existing gas turbine within an IGCC plant.

7.1.3 Axial compressor design using CFD

A necessary step for the current work was the generation of an axial compressor geometry for conventional combined cycle operating with natural gas. Although compressor 3D design does not represent a typical topic of research, the methodology described in Chapter 5 may be considered an educated procedure and useful example to cover such argument. Although further improvements can be achieved, the discussion focused on important aspects related to the generation of three-dimensional blade shapes within multi-stage axial compressor for industrial applications. The importance of using CFD when proposing a modified design as well as the benefits of reducing secondary losses during design refinement were emphasised. In addition, the FORTRAN code written in order to generate 3D geometries for different types of blade profiles (provided the required input parameters) may be a useful tool for future research in blade shape optimisation using CFD.

7.2 Recommendations and future work

The study performed in this thesis is potentially important to a gas turbine designer for IGCC plants. However the results are not exhaustive and limits of the adopted approach should be highlighted. The following subsections attempt to provide suggestions for improvements and further research.

7.2.1 Blade radial stacking line modifications

The choice of adopting blade true sweep for the H2-IGCC compressor was supported by the fact that, compared to geometric modifications in the tangential directions, it allows a re-distribution of the radial forces without adding additional load. This was however explored only in the study performed on NASA Rotor 37. Therefore it could be useful, for instance, to investigate the effect of applying blade lean in the last stator of the IDAC compressor and compare the results with those illustrated in section 4.4. This would contribute to confirm that major benefits are generally provided by true sweep. Furthermore, the reduction of the axial gap between the swept and upstream blades may represent a major drawback compared to the tangentially bended blade. It is generally acknowledged that the smaller the axial gap the higher may be the resulting unsteady forces on the downstream blade-row. Unsteady simulations should be therefore performed with the aim of investigating the aeroelasticity effects and engine order excitations in the stages of interest.

7.2.2 Variable stator vanes and part-load operation

In Chapter 6 it was stated that the proposed new gas turbine configuration would allow for an acceptable stable air flow modulation. However the part-load operation range could not be compared with the one of the baseline geometry, since the power control working line for natural gas combustion was not provided by the through-flow model. It would be important to investigate if the constant TIT and IGV only control range obtained for the re-designed machine would be considerably lower with respect to the reference case.

Since slight increases in turbine blade metal temperatures and gas turbine net power output were predicted by the mean line design analysis, the effects on the

cooling effectiveness and machine structural integrity, as well as possible solutions, should be explored. Clearly an accurate CFD modelling of the cooling system would be preferable. In addition, due to the small changes in gas turbine outlet condition, the consequent variations of the steam turbine and combined cycle performance should be quantified and compared with the baseline case.

It was discussed that an adaptation of the compressor to the two different types of combustion would be achievable by providing an IGV mechanical actuator independent of the one of the stators. If practicable, this would however increase the costs. Thus, it may be useful to repeat the investigation proposed in Chapter 6 by assuming a single mechanical actuator for the same variable guide vanes and comparing the overall performance.

Finally, regardless of the type of combustion, a challenging task for future research is represented by the need for improving part-load operation efficiency that play a key role in the combined cycle performance during power modulation.

7.2.3 Axial compressor design using CFD

The analytical tool used in Chapter 5 for the calculation of the spanwise distribution of flow and blade angles is based on the adoption of constant specific enthalpy and axial velocity along the radius. The former assumption is widely used in compressor design, while methods that satisfy the simple radial equilibrium equation, involving a spanwise variation of the axial velocity, are generally preferred. The choice of the applied method was forced by the need to provide realistic velocity diagrams at the end-wall regions of the front stages. Since high efficiency was obtained for the transonic stages the same criterion was used for the remaining stages. However, it is believed that another solution would be to use different design criteria along the compressor. For the presented case, for instance, it may be interesting to investigate if by applying another method that satisfies the simple radial equilibrium in the middle and rear stages would lead to higher compressor efficiency or reduced need of CFD refinement of the design.

Another important aspect is represented by the bleeding mechanism adopted to perform CFD simulations. Although it is believed that inter-stage air extraction is commonly used, it may be interesting to explore the possibility of modifying

the technology and obtaining an enhancement in compressor performance. For instance, the possibility of extracting part of the air along the stator suction sides (and potentially improve their diffusion-limiting features) is very attractive.

In addition to the limitations related to RANS turbulence modelling, a major issue is represented by the use of CFD steady-state simulations for multi-stage compressors. It is known that, for a given blade-row, the application of mixing planes neglects the effect of circumferential non-uniform flow field of the upstream and downstream blade-rows, thus affecting the accuracy of the predictions. Nevertheless, in spite of the ever increasing computing power, unsteady flow simulations for a compressor with a high number of stages are still not very feasible. However, once all the major aspects of compressor design are solved via steady simulations, an unsteady CFD analysis of the near-stall operating condition may improve the quality of the results and further assess the reliability of the produced design.

Bibliography

[1] Low emission gas turbine technology for hydrogen-rich syngas. Brochure, ETN, 2008.

[2] J. Wu, P. Brown, I. Diakunchak, A. Gulati, M. Lenze, and B. Koestlin. Advanced gas turbine combustion system development for high hydrogen fuels. In *ASME Turbo Expo*, number GT2007-28337, 2007.

[3] H.J. Herzog. The economics of CO_2 separation and capture. MIT Energy Laboratory, 2005.

[4] E.S. Rubin, A.B. Rao, and C. Chen. Comparative assessments of fossil fuel power plants with CO_2 capture and storage. *Proceedings of 7^{th} International Conference on Greenhouse Gas Control Technologies*, 1:285–293, 2005.

[5] C. Descamps, C. Bouallou, and M. Kanniche. Efficiency of an integrated gasification combined cycle (IGCC) power plant including CO_2 removal. *Energy*, 33:874–881, 2008.

[6] T. Lieuwen, V. McDonell, E. Petersen, and D. Santavicca. Fuel flexibility influences on premixed combustor blowout, flashback, autoignition and stability. *Journal of Engineering for Gas Turbines and Power*, 130:011506 (10 pages), 2008.

[7] P. Chiesa, G. Lozza, and L. Mazzocchi. Using hydrogen as gas turbine fuel. *Journal of Engineering for Gas Turbines and Power*, 127:73–80, 2005.

[8] R. Chacartegui, D. Sanchez, J.M. Munoz, T. Munoz, and T. Sanchez. Gas and steam combined cycles for low calorific syngas fuels utilisation. *Applied Energy*, 101:81–92, 2013.

[9] Y.S. Kim, J.J. Lee, T.S. Kim, and J.L. Sohn. Effects of syngas type on the operation and performance of a gas turbine in integrated gasification combined cycle. *Energy Conversion and Management*, 52:2262–2271, 2011.

[10] J.C. Mankins. Technology readiness levels - a white paper. Office of Space Access and Technology, 1995.

[11] D. Jones, D. Bhattacharyya, R. Turton, and S.E. Zitney. Optimal design and integration of an air separation unit (ASU) for an integrated gasification combined cycle (IGCC) power plant with CO_2 capture. *Fuel Processing Technology*, 92:1685–1695, 2011.

[12] H. Cohen, G.F.C. Rogers, and H.I.H Saravanamuttoo. *Gas Turbine Theory*. Pearson Education, 2009.

[13] J.J. Lee, Y.S. Kim, T.S. Kim, J.L. Sohn, and Y.L. Joo. Influence of system integration options on the performance of an integrated gasification combined cycle power plant. *Applied Energy*, 86:1788–1796, 2008.

[14] D. Sanchez, R. Chacartegui, J.M. Munoz, T. Munoz, and T. Sanchez. Performance analysis of a heavy duty combined cycle power plant burning various syngas fuels. *International Journal of Hydrogen Energy*, 35:337–345, 2009.

[15] F. He, Z. Li, L. Ma, and E.N. Pistikopoulos. Operation window and part-load performance study of a syngas fired gas turbine. *Applied Energy*, 89:133–141, 2012.

[16] J.F. Louis. Systematic studies of heat transfer and film cooling effectiveness. In *AGARD-Conference Proceedings-229*, number 28, 1977.

[17] Y.S. Kim, J.J. Lee, T.S. Kim, and J.L. Sohn. Performance analysis of a syngas-fed gas turbine considering the operating limitations of its components. *Applied Energy*, 87:1602–1611, 2009.

[18] G. Cerri, C. Basilicata, and A. Giovannelli. Compressor modifications for 300 MW IGCC gas turbine stable behaviour. In *ASME Turbo Expo*, number GT2013-94056, 2013.

[19] R.F. Geosits and L.A. Schmoe. IGCC: the challenges of integration. In *ASME Turbo Expo*, number GT2005-68997, 2005.

[20] A.R. Smith and K. Klosek. A review of air separation technologies and their integration with energy conversion processes. *Fuel Processing Technology*, 70:115–134, 2011.

[21] F. Hannemann, B. Koestlin, and G. Zimmermann. Pushing forward IGCC technology at Siemens. In *Gasification Technology Conference*, 2003.

[22] T.S. Kim. Comparative analysis on the part load performance of combined cycle plants considering design performance and power control strategy. *Energy*, 29:71–85, 2004.

[23] L. Gallar, M. Aria, V. Pachidis, and R. Singh. Stochastic axial compressor variable geometry schedule optimisation. *Journal of Applied Science and Technology*, 15:366–374, 2011.

[24] T.S. Kim and S.H. Hwang. Part load performance analysis of recuperated gas turbines considering engine configuration and operation strategy. *Energy*, 31:260–277, 2006.

[25] B.F. Moller, M. Genrup, and M. Assadi. On the off-design of a natural gas-fired combined cycle with CO_2 capture. *Energy*, 32:353–359, 2007.

[26] M. Jansen, T. Schulenberg, and T. Waldinger. Shop test result of the V64.3 gas turbine. *Journal of Engineering for Gas Turbines and Power*, 114:676–681, 1992.

[27] B. Lakshminarayana, M. Pougare, and R. Davino. Three-dimensional flow field in the tip region of a compressor rotor passage. *Journal of Engineering for Gas Turbines and Power*, 4:772–781, 1982.

[28] H. Jian and W. Hu. Numerical investigation of inlet distortion on an axial flow compressor rotor with circumferential groove casing treatment. *Chinese Journal of Aeronautics*, 21:496–505, 2008.

[29] J. Kim, K. Choi, and K. Kim. Aerodynamic analysis and optimisation of a transonic axial compressor with casing grooves to improve operating stability. *Aerospace Science and Technology*, 29:81–91, 2013.

[30] D.C. Rabe and C. Hah. Application of casing circumferential grooves for improved stall margin in transonic axial compressor. In *ASME Turbo Expo*, number GT2002-30641, 2002.

[31] I. Wilke and H. Kau. A numerical investigation of the flow mechanism in a high pressure compressor front stage with axial slots. *Journal of Turbomachinery*, 126:339–349, 2004.

[32] G. Lagras, I. Trebinjac, N. Gourdain, X. Ottavy, and L. Castillon. A novel approach to evaluate benefits of casing treatment in axial compressor. *International Journal of Rotating Machinery*, 2012:975407 (19 pages), 2012.

[33] R. Biollo and E. Benini. Recent advances in transonic axial compressor aerodynamics. *Progress in Aerospace Science*, 56:1–18, 2013.

[34] K.L. Suder, M.D. Hathaway, S.A. Thorp, A.J. Strazisar, and M.M. Bright. Compressor stability enhancement using discrete tip injection. *Journal of Turbomachinery*, 123:14–23, 2001.

[35] S. Hiller, R. Matzgeller, and W. Horn. Stability enhancement of a multi-stage compressor by air injection. In *ASME Turbo Expo*, number GT2009-59868, 2009.

[36] A.J. Strazisar, M.M. Bright, S. Thorp, D.E. Culley, and K.L. Suder. Compressor stall control through end wall recirculation. In *ASME Turbo Expo*, number GT2004-54295, 2004.

[37] A.I. Sayma, M. Vahdati, and M. Imregun. Multi-bladerow fan forced response predictions using an integrated three-dimensional time-domain aerolasticity model. *Journal of Mechanical Engineering Science*, 214:1467–1483, 2000.

[38] A.I. Sayma. Towards virtual testing of compression systems in gas turbine engines. *International Journal of CFD Case Studies*, 9:29–42, 2011.

[39] A.I. Sayma, M. Vahdati, L. Sbardella, and M. Imregun. Modeling of three-dimensional viscous compressible turbo machinery flows using unstructured hybrid grids. *AIAA Journal*, 38:945–954, 2000.

[40] P.R. Spalart and S.R. Allmaras. A one-equation turbulence model for aerodynamic flows. *AIAA 92-0439*, 1992.

[41] L. Reid and R.D. Moore. Design and overall performance of four highly-loaded, high speed inlet stages for an advanced, high pressure ratio core compressor. Technical Paper 1337, NASA, 1978.

[42] L. Reid and R.D. Moore. Experimental study of low aspect ratio compressor blading. *Journal of Engineering for Gas Turbines and Power*, 102:875–882, 1980.

[43] K.L. Suder and M.L. Celestina. Experimental and computational investigation of the tip clearance flow in a transonic axial compressor rotor. *Journal of Turbomachinery*, 118:218–229, 1996.

[44] T. Knopp. On grid-independence of RANS predictions for aerodynamic flows using model-consistent universal wall-functions. In *Proceedings of ECCOMAS CFD*, 2006.

[45] J. Denton. Lesson from Rotor 37. *Journal of Thermal Science*, 6:1–13, 1997.

[46] R.V. Chima. Swift code assessment for two similar transonic compressors. Technical Memorandum 215520, NASA, 2009.

[47] J. Dunham. CFD validation for propulsion system components. Advisory Report 355, AGARD, 1998.

[48] C. Hah and J Loellbach. Development of hub corner stall and its influence on the performance of axial compressor blade rows. In *ASME Turbo Expo*, number 97-GT-42, 1997.

[49] C. Hah. Large eddy simulation of transonic flow field in NASA Rotor 37. Technical Memorandum 215627, NASA, 2009.

[50] A. Shabbir, M.L. Celestina, J.J. Adamczyk, and A.J. Strazisar. The effect of hub leakage flow on two high speed axial compressor rotors. In *ASME Turbo Expo*, number 97-GT-346, 1997.

[51] K.L. Suder. Blockage development in a transonic axial compressor rotor. *Journal of Turbomachinery*, 120:465–476, 1998.

[52] N.P. Gopinathrao, D. Bagshaw, C. Mabilat, and Alizadeh S. Non-determiistic CFD simulation of a transonic compressor rotor. In *ASME Turbo Expo*, number 97-GT-346, 1997.

[53] B.H. Beheshti, J.A. Teixeira, P.C. Ivey, K. Ghorbanian, and B. Farhanieh. Parametric study of tip clearance casing treatment on performance and stability of a transonic axial compressor. *Journal of Turbomachinery*, 126:527–535, 2004.

[54] S. Lieblein, F.C. Schwenk, and R.L. Broderick. Diffusion factor for estimating losses and limiting blade loadings in axial-flow compressor blade elements. Research Memorandum E53D01, NASA, 1957.

[55] J.A. Wennerstrom. *Design of highly loaded axial-flow fans and compressors*. Concepts ETI, 2000.

[56] C.C. Koch. Stalling pressure rise capability of axial compressor stages. *Journal of Engineering for Power*, 103:645–656, 1981.

[57] V.M. Lei, Z.S. Spakovsky, and E.M. Greitzer. A criterion for axial compressor hub-corner stall. *Journal of Turbomachinery*, 130:031006 (10 pages), 2008.

[58] M.T. Schobeiri. A new shock loss model for transonic and supersonic axial compressors with curved blades. *Journal of Propulsion and Power*, 14:470–478, 1998.

[59] N.A. Cumpsty. *Compressor aerodynamics*. Krieger, 2004.

[60] P.V. Ramakrikrishna and M. Govardhan. Numerical study of stagger angle effects in forward swept axial compressor rotor passages. In *ASME Turbo Expo*, number GT2010-23160, 2010.

[61] Y.A. Yoon, S.J. Song, and H.W. Shin. Influence of flow coefficient, stagger angle, and tip clearance on tip vortex in axial compressors. *Journal of Fluids Engineering*, 128:1274–1280, 2006.

[62] C. Hah, S.L. Puterbaugh, and A.R. Wadia. Control of shock structure and secondary flow field inside transonic compressor rotors through aerodynamic sweep. In *ASME Turbo Expo*, number 98-GT-56, 1998.

[63] A.R. Wadia, P.N. Szucs, and D.W. Crall. Inner workings of aerodynamic sweep. *Journal of Turbomachinery*, 120:671–682, 1998.

[64] H. Passrucker, M. Engber, S. Kablitz, and D. K. Hennecke. The effect of forward sweep in a transonic compressor rotor. *Journal of Power and Energy*, 217:357–365, 2003.

[65] J. D. Denton and L. Xu. The effects of lean and sweep on transonic fan performance. In *ASME Turbo Expo*, number GT-2002-30327, 2002.

[66] C. Xu and R.S. Amano. Computational analysis of swept compressor rotor blades. *International Journal for Computational Methods in Engineering Science and Mechanics*, 9:374–382, 2008.

[67] M.G. Beiler and T.H. Carolus. Computation and measurement of the flow in axial flow fans with skewed blades. *Journal of Turbomachinery*, 121:59–66, 1999.

[68] S.J. Gallimore, J.J. Bolger, N.A. Cumpsty, M.J. Taylor, P.I. Wright, and J.M.M. Place. The use of sweep and dihedral in multistage axial flow compressor blading - part I: University research and methods development. *Journal of Turbomachinery*, 124:521–532, 2002.

[69] P.V. Ramakrishna and M. Govardhan. Study of sweep and induced dihedral effects in subsonic axial flow compressor passages - part I: Design considerations-changes in incidence, deflection, and streamline curvature. *International Journal of Rotating Machinery*, 2009:787145 (11 pages), 2009.

[70] L. Ji, J. Chen, and F. Lin. Review and understanding on sweep in axial compressor design. In *ASME Turbo Expo*, number GT2005-68473, 2005.

[71] J. Vad, A.R.A. Kwedikha, C. Horvath, M. Balczo, M.M. Loahsz, and T. Regert. Aerodynamic effects of forward blade skew in axial flow rotors of controlled vortex design. *Journal of Power and Energy*, 221:1011–1023, 2007.

[72] A. Corsini and F. Rispoli. Using sweep to extend the stall-free operational range in axial fan rotors. *Journal of Power and Energy*, 218:129–139, 2003.

[73] L.H. Smith and H. Yeh. Sweep and dihedral effects in axial-flow turbomachinery. *Journal of Basic Engineering*, 85:401416, 1963.

[74] T. Sasaki and F. Breugelmans. Comparison of sweep and dihedral effects on compressor cascade performance. *Journal of Turbomachinery*, 120:454–463, 1998.

[75] M. Govardham, O.G. Krishna Kumar, and N. Sitaram. Investigations on low speed axial compressor with forward and backward sweep. *Journal of Thermal Science*, 16:121–133, 2007.

[76] S.L. Dixon and A. Hall. *Fluid Mechanics and Thermodynamics of Turbomachinery*. Elsevier, 2010.

[77] K.P. Mohammad and D.P. Raj. Investigations on axial flow fan impellers with forward swept blades. *Journal of Fluids Engineering*, 99:543–547, 1977.

[78] F. Breugelmans, Y. Carels, and M. Demuth. Influence of dihedral on the secondary flow in a two-dimensional compressor cascade. *Journal of Engineering for Gas Turbines and Power*, 106:578–584, 1984.

[79] J. Bergner, D.K. Hennecke, M. Hoeger, and K. Engel. Darmstadt rotor no. 2, ii: Design of leaning rotor blades. *International Journal of Rotating Machinery*, 9:385–391, 2003.

[80] E. Benini and R. Biollo. Aerodynamics of swept and leaned transonic compressor-rotors. *Applied Energy*, 84:1012–1027, 2007.

[81] R. Niehuis, A. Bohne, and A. Hoyanacki. Experimental investigation of unsteady flow phenomena in a three-stage axial compressor. *Journal of Power and Energy*, 217:341–348, 2003.

[82] A. Bohne and R. Niehuis. Experimental off-design investigation of unsteady secondary flow phenomena in a three-stage axial compressor at 100% nominal speed. In *ASME Turbo Expo*, number GT2004-53100, 2004.

[83] L. Gallar, V. Pachidis, P. Zachos, and R. Singh. Compressor IGV off design performance and loss modelling. 1221:957–964, 2009.

[84] A. Fischer, W. Riess, and J.R. Seume. Performance of strongly bowed stators in a four-stage high-speed compressor. *Journal of Turbomachinery*, 126:333–338, 2001.

[85] T. Sasaki and F.A.E. Breugelmans. Comparison of sweep and dihedral effects on compressor cascade performance. *Journal of Turbomachinery*, 120:454–464, 1998.

[86] L. Huawei, C. Fu, W. Jilin, and W. Zhongqi. Flow field improvement by bowed stator stages in a compressor with different axial gaps under near stall condition. *Chinese Journal of Aeronautics*, 21:215–222, 2007.

[87] J. Friedrichs, S. Baumgarten, G. Kosyna, and U. Stark. Effect of stator design on stator boundary layer flow in a highly loaded single-stage axial-flow low-speed compressor. *Journal of Turbomachinery*, 123:483–489, 2001.

[88] G. Cerri and L. Chennaoui. General method for the development of gas turbine based plant simulators: an IGCC application. In *ASME Turbo Expo*, number GT2013-94040, 2013.

[89] G. Cerri. A simultaneous solution method based on a modular approach for power plant analyses and optimised designs and operations. In *ASME Turbo Expo*, number 96-GT-302, 1996.

[90] G. Cerri. Description of the models adapted or developed *ad hoc* for the IGCC & CCS plants. Technical report, Univeristy of Rome Tre, 2012.

[91] H. Ceric, J. Slad, and T. Johnke. Latest performance upgrade of the Siemens gas turbine SGT5-4000F. Brochure, Siemens, 2008.

[92] 2010 Energy Handbooks, Combined Cycle Journal, Ansaldo: a global leader in generation technology. Brochure, Ansaldo, 2009.

[93] F. Sieverding, B. Ribi, M. Casey, and M. Meyer. Design of industrial axial compressor blade sections for optimal range and performance. *Journal of Turbomachinery*, 126:323–331, 2004.

[94] Wilson D.G. and Korakianitis T. *The design of high-efficiency turbomachinery and gas turbines*. Prentice Hall, 1998.

[95] T. Dickens and I. Day. The design of highly loaded axial compressor. *Journal of Turbomachinery*, 133, 2010.

[96] J.H. Horlock and J.D. Denton. A review of some early design practice using computational fluid dynamics and a current perspective. *Journal of Turbomachinery*, 127:5–13, 2005.

[97] R.H. Aungier. *Axial Flow Compressors: A Strategy for Aerodynamic Design and Analysis*. Wiley-Blackwell, 2003.

[98] A.S. Lebedev and S.V. Kostennikov. Trends in increasing gas-turbine units efficiency. *Thermal Engineering*, 55:461–468, 2008.

[99] GT24/GT26 gas turbines. Brochure, Alstom, 2013.

[100] Siemens gas turbine SGT5-4000F advanced performance. Brochure, Siemens, 2008.

[101] E. Deuker, M.H. Koenig, M. Moeller, J. Slad, and H. Streb. SGT5-4000F gas turbine and combined cycle power plant evolution reflecting the changing market requirements.

Appendices

Appendix A

Gas turbine units of various classes

The technical level of gas turbine units is represented by three indices: the gas turbine efficiency and net power output (or capacity) and the efficiency of the combined cycle. Among several factors, these parameters are strongly dependent on the maximum achievable TIT. Figure A.1 shows the temperature trend evolution obtained by the main gas turbine manufactures. According to the level of efficiency, gas turbine plants are divided into the following four classes (see Figure A.2) [98].

E class units, developed in the middle of the 1980's, are characterised by high reliability, long operation time and relatively low maintenance cost. The TIT is about 1100 $^{\circ}C$, the cycle pressure ratio varies from 10 to 12 and the gas turbine and combined cycle efficiency ranges from 33% to 35% and from 50% to 53% respectively.

F class units, delivered to the market in the late 1990's, represent the state-of-art of power plants in operation. These are characterised by a TIT that varies from 1250 to 1350$^{\circ}C$, cycle pressure ratio of 15-17 and gas turbine and combined cycle efficiency of 35-36% and 54-55% respectively.

FA (FB) class units represent an evolutionary step in proven F series. The use of advanced material and cooling scheme systems allow for an extended lifetime and high level of efficiency that can reach 38.5% for the gas turbine and 58% for the combined cycle. In addition, enhanced combustion technologies provide a reduction in NO_x emissions and allow for fuel flexibility to handle current as well as unconventional fuels.

G and H Class units represent the most advanced prototypes of very high capacity machines. The TIT can reach 1500 $°C$, the pressure ratio is more than 20 and the gas turbine and combined cycle efficiency is of 39-40% and 58-60% respectively. Such increase in TIT and thus performance is mainly ensured by the use of special thermal barrier coating and single-crystal blades for the first expander stage that allow to increase significantly the turbine blade metal temperature. In addition, the level of efficiency of the these new models is also a result of other unit upgrading techniques and strategies that differ from manufacturer to manufacturer. A main innovation applied by General Electric, for instance, is the use of combined steam-air cooling that enhances the cooling effectiveness since the specific heat capacity of steam is higher than that of air [98]. Furthermore, the air that is not anymore bled from the compressor can be sent to the combustion chamber and through the turbine inlet section, thus increasing the gas turbine net power output. In one of the most advanced gas turbine manufactured by Alstom, a unique sequential combustion system with gas reheat during its expansion is implemented [99]. Combined with an advanced combustion technology this allows for an efficient operation flexibility, supporting a wide range of gas variations. In addition, major advantages are represented by the very high combined cycle efficiency (due to the high temperature of the gas at the exit of the low-pressure turbine) and the possibility of maintaining high efficiency also at part-load.

According to the objectives of the thesis, some features of the SGT5-4000F Siemens machine (see Fig. A.3) are finally presented [91, 100]. Besides the development conducted by other major manufactures that led to the introduction of new machines, Siemens provided a continuous improvement of the models that have been already mastered. Within the Siemens design philosophy, the limiting of changes of geometry and material specifications represents an important aspect [101]. This ensures a reduction of the risks typically involved during a "new " design process since the applied modifications are based on proven and pre-tested designs. The evolutionary design principle also allows for a fast, easy and reliable installation of the modified parts which can be directly compared with those of the previous design. The SGT5-4000F, for instance, was introduced in 1996 and constantly upgraded in order to meet the challenges of current and future market requirements.

For example, important improvements are applied to the compressor on the basis of aircraft engine technologies. The flow path is optimised with CD airfoils. The profile steepness of the hub annulus line at the front of the compressor is increased in order to optimise (minimise) the number of stages without considerably reducing the efficiency for a given pressure ratio. Furthermore, hydraulic tip gap control in order to optimise rotor clearances at different operating conditions is implemented. In addition to the techniques of single-crystal turbine blade with thermal barrier coating, further increase of the TIT is obtained by reducing the leakage air in the hot gas path and amount of cooling in areas which may be excessively cooled and via an intensive improvement of the existing air cooling technology. Finally, a further technique that is taken into account in order to cope with the fuel-flexibility requirements is represented by fuel gas preheating. This also leads to an increase in efficiency and reduction of NO_x emissions during the different load operation [101].

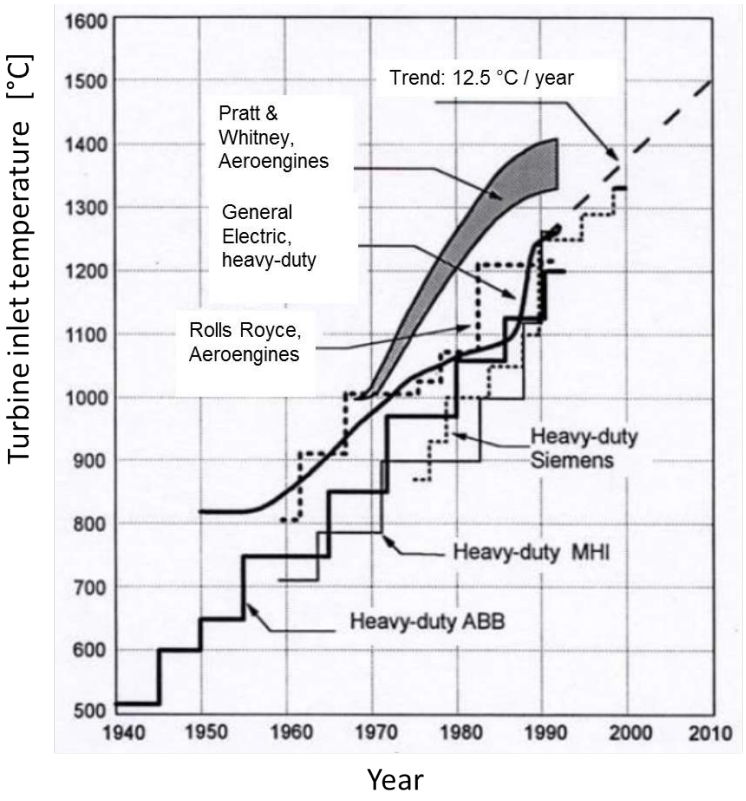

Figure A.1: Evolution of TIT of gas turbines

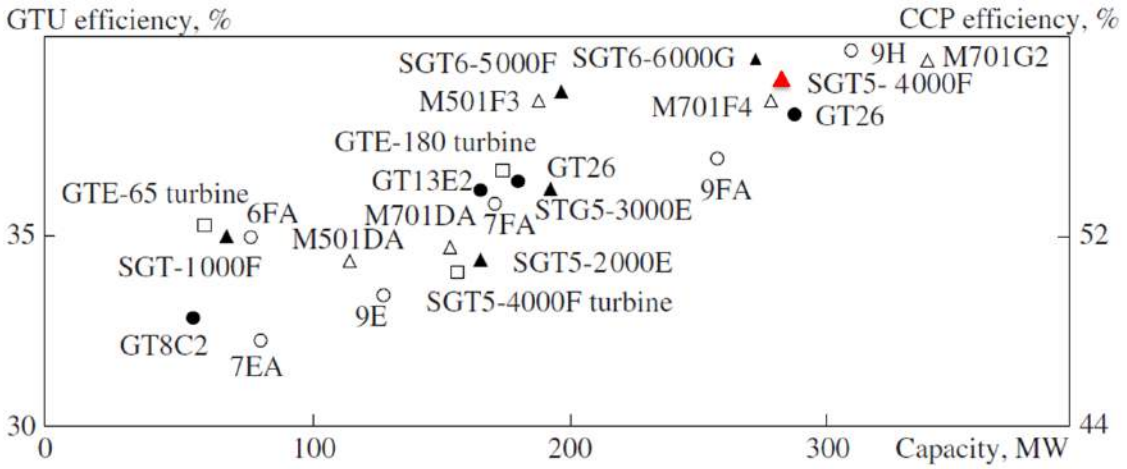

Figure A.2: Efficiency of gas turbines and combined cycles of different classes. Manufacturer: (○) General Electric, (▲) Siemens, (●) Alstom, (△) Mitsubishi, (□) Silovie Mashiny, (Lebedev et al., 2008)

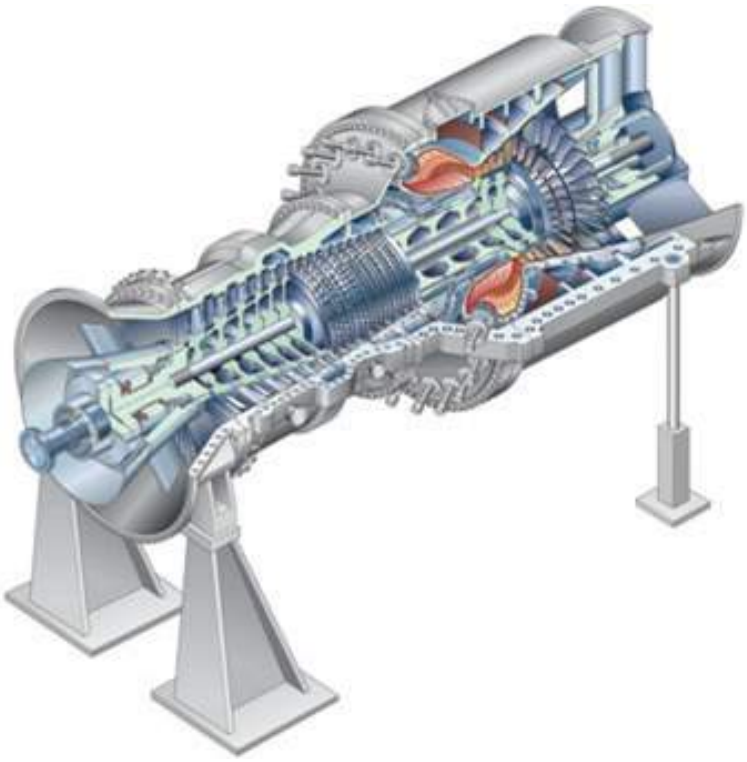

Figure A.3: SGT5-4000F turbine